

令和6年度博士論文

**One-step Gas Phase Fabrication of Semiconductor-
based Nanomaterials and Their Characteristics with
Enhanced Photocatalytic Performance**
半導体系ナノ材料のワンステップ気相作製と
増大した光触媒性能を含む特性

Supervisor: Manabu Shimada
指導教員: 島田 学 教授

Chemical Engineering Program
Division of Advanced Science and Engineering
Graduate School of Advanced Science and Engineering
Hiroshima University

広島大学
大学院先進理工系科学研究科
先進理工系科学専攻
化学工学プログラム

2024年9月

Meditha Hudandini
メディタ フダンディニ

Abstract

Semiconductor-based photocatalysts were fabricated via one-step gas-phase method, specifically utilizing plasma enhanced chemical vapor deposition and physical vapor deposition method to fabricate TiO₂, TiO₂-CuO, and TiO₂-Ag nanoparticulate thin films. In addition, spray pyrolysis method to fabricate ZnO and ZnO-Ag nanoparticles. These semiconductor-based photocatalysts characteristic and enhanced photocatalytic activity were assessed.

Chapter 1 elaborates on the detailed exploration and importance of the materials utilized and the various processes involved in nanomaterial fabrication and their applications in advanced oxidation processes (AOPs), specifically photocatalysis. This overview serves as the motivation behind the research investigation within the scope of this dissertation.

Chapter 2 explores the production of TiO₂-CuO nanoparticulate thin films via a one-step PECVD-PVD method, followed by an assessment of their photocatalytic activity under visible light, considering the anatase or rutile crystalline phases, which is altered by the increase of the post-deposition annealing temperature. Results showed, the rutile- TiO₂-CuO film exhibited superior photocatalytic activity compared to anatase- TiO₂-CuO. Further investigation focused on the characteristics of anatase TiO₂-CuO. The photocatalytic activity was explored by alterations in UV or visible light exposure, pH, and the addition of H₂O₂ to the photodegradation system. The results showed that TiO₂-CuO/H₂O₂ at pH 13 exhibited the highest photocatalytic activity.

Chapter 3 extends the investigation of TiO₂-based photocatalysts by loading noble-metal Ag nanoparticles. Utilizing the same fabrication system as in **Chapter 2**, Ag-loaded TiO₂ was fabricated. The addition of Ag extends the light absorbance of TiO₂ the

visible light wavelengths. Results demonstrated that at specific Ag contents, TiO₂-Ag exhibits superior photocatalytic activity compared to pristine TiO₂ under visible light irradiation. Additionally, this chapter delves into a comprehensive examination of how variations in the heating rate during post-deposition annealing affect the characteristics of TiO₂-Ag such as crystallinity and surface area.

Chapter 4 expands the scope of semiconductor-based photocatalysts beyond the one-step PECVD-PVD method and TiO₂-based materials. It explores alternative one-step gas-phase fabrication methods and materials by focusing on Ag-loaded ZnO using SP method, which resulted in crumpled-shaped particles. The photocatalytic activity was assessed for treating real textile wastewater, offering insights into its potential application in environmental remediation. The photocatalytic activity of ZnO-Ag was higher compared to ZnO.

Chapter 5 Summarizes the findings from all chapters and suggests future research directions.

Table of Contents

Abstract	i
Table of Contents	iii
List of Figures	v
List of Tables	ix
Chapter 1	1
Introduction	1
1.1. Advanced oxidation process by photocatalysis	1
1.2. Materials for photocatalysis	3
1.2.1. Characteristics of semiconductor-based photocatalyst	3
1.2.1.1. TiO ₂	4
1.2.1.2. ZnO	7
1.2.2. Enhancing the activity of photocatalysts	7
1.2.2.1. Semiconductor-semiconductor heterojunctions	9
1.2.2.2. Semiconductor-metal heterojunction	13
1.3. Methods of fabrication	16
1.3.1. Solid-phase method for fabricating nanomaterials	16
1.3.2. Liquid-phase method for fabricating nanomaterials	18
1.3.3. Gas-phase method for fabricating nanomaterials	20
1.3.3.1. Chemical vapor deposition (CVD)	21
1.3.3.3. Physical vapor deposition (PVD)	23
1.4. Advancement of the fabrication and application of photocatalyst	25
1.4.1. Post-deposition heat treatments	26
1.4.2. Addition of foreign materials by a one-step gas-phase method	27
1.4.3. Photocatalytic test conditions	28
1.5. Objectives and outline of dissertation	29
Chapter 2	33
Gas-phase Fabrication of TiO₂ and TiO₂-CuO: Enhancing Photocatalytic Activity	33
2.1. Introduction	34
2.2. Materials and experimental setup	35
2.3. Characterization of TiO ₂ and TiO ₂ -CuO	37
2.4. Evaluation of photocatalytic activity	37
2.5. Results and discussions	38

2.5.1.	Photocatalytic Activity of Cu _x O-loaded Anatase- or Rutile- TiO ₂	38
2.5.2.	Photocatalytic activity optimization of CuO-loaded anatase-TiO ₂ through H ₂ O ₂ addition and pH adjustments.....	46
2.6.	Conclusions.....	57
Chapter 3	59
Investigation of TiO₂ and TiO₂-Ag Photocatalyst Fabricated by the Gas-phase Method	59
3.1.	Introduction.....	60
3.2.	Materials and experimental procedures	61
3.3.	Characterization of TiO ₂ and TiO ₂ -Ag.....	62
3.4.	Results and discussions.....	63
3.4.1.	Visible-light photocatalytic activity of TiO ₂ and TiO ₂ -Ag	63
3.4.2.	The effect of heating rate on the characteristics and photocatalytic activity of TiO ₂ -Ag	69
3.5.	Conclusions.....	78
Chapter 4	79
Extending Research on Semiconductor-based Photocatalyst Fabricated by Alternative Gas-phase Method	79
4.1.	Introduction.....	80
4.2.	Materials and experimental setup	82
4.3.	Powder characterization.....	83
4.4.	Evaluation of photocatalytic activity	83
4.5.	Results and discussions.....	84
4.6.	Conclusions.....	91
Chapter 5	93
Summary	93
5.1.	Conclusions.....	93
5.2.	Suggestions for future studies	94
References	xi
List of Publications	xvii
List of Presentations	xix

List of Figures

Figure 1. Characteristics of Good Photocatalyst. Adapted from [8].	3
Figure 2. Band Gap Energy of Semiconductors. Adapted from [9].	4
Figure 3. Crystal phases of TiO ₂ : a) anatase, b) rutile, and brookite.	5
Figure 4. a) Comparison of recombination processes and b) transfer diagram of anatase and rutile. Adapted from [12].	6
Figure 5. Schematic of the charges-carrier separation in three type combination systems of semiconductor-semiconductor heterojunction. Adapted from [13,22].	10
Figure 6. Morphology of a) TiO ₂ /CuO, b) CuO-ZnO, and c) ZnO/TiO ₂ . Adapted from [26–28].	11
Figure 7. Schematic of hydroxyl radical formation by TiO ₂ -CuO/H ₂ O ₂ under UV and visible light irradiation.	13
Figure 8. Morphology of a) TiO ₂ /Ag, b) TiO ₂ -Ag NWs, and c) ZnO/Ag. Adapted from [5,16,40].	15
Figure 9. Schematic of carrier-charge separation of semiconductor and Ag under a) UV and b) visible light irradiations.	15
Figure 10. Preparation of TiO ₂ by ball-milling. Adapted from [41].	18
Figure 11. Morphology of a) TiO ₂ and b,c,d) TiO ₂ /Ag fabricated by a,b) sol-gel and c,d) hydrothermal methods. Adapted from [42,43].	19
Figure 12. a) Schematic of spray pyrolysis experimental set-up; morphology of b) Ag/ZnO and c) TiO ₂ nanoparticles fabricated by spray pyrolysis. Adapted from [37,54].	22
Figure 13. Schematic of a) simplified evaporation-condensation experimental setup and b) nanoparticles deposition process by ALD. Adapted from [57,58].	24
Figure 14. Classification of thin-film deposition methods. Adapted from [61].	26
Figure 15. Diagrammatic illustration of the objective of this dissertation.	31
Figure 16. Schematic of PECVD-PVD experimental setup.	36
Figure 17. SEM images of TiO ₂ annealed at a) 400 °C, b) 500 °C, c) 600 °C, d) 700 °C, and e) 800 °C.	39
Figure 18. a) XRD pattern, b) band gap, and c) I-V curve of TiO ₂ annealed at different temperatures.	40
Figure 19. TEM images of TiO ₂ -Cu _x O nanoparticles annealed at a) 500 °C and b) 800 °C; and c) XRD patterns of TiO ₂ and TiO ₂ -Cu _x O annealed at 500 °C and 800 °C.	42

Figure 20. XPS spectra of a,c) anatase- b,d) rutile- TiO ₂ and TiO ₂ -Cu _x O, respectively. The solid and dotted lines represent the XPS and deconvoluted spectra, respectively.....	43
Figure 21. Reaction rate constants for photocatalytic activity under visible light irradiation of anatase- or rutile- TiO ₂ as well as their TiO ₂ -Cu _x O counterparts.	44
Figure 22. Schematic of charge separation of anatase- and rutile- TiO ₂ -Cu _x O under visible light irradiation.	46
Figure 23. Morphology of nanoparticles. (a) SEM images of TiO ₂ (inset: TEM). HR-TEM of (b) TiO ₂ and (c,d) Cu _x O. Additionally, (e) TEM image and (f) EDS spectrum highlight TiO ₂ -Cu _x O.....	47
Figure 24. XRD pattern indicating crystallinity of TiO ₂ , Cu _x O, and TiO ₂ -Cu _x O nanoparticulate thin films.	49
Figure 25. Chemical state of a) TiO ₂ , (b) Cu _x O, and (c) TiO ₂ -CuO. The solid and dotted lines represent the XPS and deconvoluted spectra, respectively.....	50
Figure 26. a) Plot of $(h\nu F(R))^{1/2}$ versus $h\nu$ of nanoparticulate thin film and b) zeta potential.	52
Figure 27. Degradation of R6G by (a) photolysis, TiO ₂ , TiO ₂ -CuO, and P25 films; and (b) the corresponding samples with added H ₂ O ₂ under UV light irradiation.	53
Figure 28. Degradation of R6G by CuO and CuO/H ₂ O ₂ under dark condition. ...	54
Figure 29. Photodegradation reaction rate constant of R6G under visible light irradiation for different pH conditions; representative curves of $\ln(C_t / C_0)$ versus time for samples at pH values of (b) 3, (c) 7, and (d) 13.	56
Figure 30. SEM images of a) TiO ₂ and TiO ₂ -Ag with b) 0.56 c) 2.97 wt. % Ag content and d) P25 film. Corresponding size distributions (insets a-c).....	64
Figure 31. XRD pattern of TiO ₂ and TiO ₂ -Ag fabricated by PECVD and PVD; P25 film prepared by spin coating.	65
Figure 32. Ag 3d XPS spectra of Ag a) before and b) after annealing in N ₂ and annealed TiO ₂ -Ag c,d) after a certain period of time.	66
Figure 33. Absorbance spectra of TiO ₂ and TiO ₂ -Ag fabricated by PECVD and PVD; P25 film prepared by spin coating.....	67
Figure 34. c) Percent degradation of R6G and d) its corresponding reaction rate constants for TiO ₂ , and TiO ₂ -Ag, and P25 film.....	69
Figure 35. SEM images showing the cross-sectional view of TiO ₂ -Ag: a) the as-deposited and annealed with b) 3 °C/min, c) 5 °C/min, d) 10 °C/min, e)	

30 °C/min, and f) 60 °C/min heating rates. The inset provides a top-view perspective.....	70
Figure 36. XPS spectra of C 1s peaks of TiO ₂ annealed at heating rates of a) 60 °C/min, b) 5 °C/min, and as deposited.	72
Figure 37. a) XRD pattern of TiO ₂ -Ag nanoparticulate thin films annealed at different heating rates and b) the ratio of anatase and rutile phases.....	73
Figure 38. XRD pattern of TiO ₂ -Ag nanoparticulate thin films at heating rates of 3 and 60 °C/min (2 h holding time).....	74
Figure 39. HR-TEM images of TiO ₂ -Ag nanoparticulate thin films at heating rates of a) 5 and 60 °C/min (12 h holding time).	75
Figure 40. Surface area, total pore volume, and particle diameter of TiO ₂ -Ag nanoparticulate thin films annealed at 600 °C.....	76
Figure 41. Photocatalytic activity of TiO ₂ -Ag nanocomposite films annealed at 600 °C with a different heating rate. a) plots of $\ln C_0/C_t$ vs irradiation time and b) rate constants.	77
Figure 42. Schematic of SP experimental setup.	82
Figure 43. SEM images of a) ZnO and ZnO-Ag with Ag concentrations of b) 1 wt. %, c) 5 wt. %, and d) 10 wt. % fabricated at an O ₂ :N ₂ ratio of 0:1. ZnO-Ag with Ag content of 10 wt. % fabricated at an O ₂ :N ₂ ratio of e) 1:2, f) 1:1, g) 2:1, h) 1:0.	84
Figure 44. Cumulative size distribution ZnO and ZnO-Ag nanoparticles based on a) carrier gas ratios and b) Ag contents.	85
Figure 45. TEM images of a) ZnO and b) ZnO-Ag nanoparticles with 10 wt. % Ag content. Corresponding EDS spectra of c) ZnO and d) ZnO-Ag nanoparticles (bulk) and e) highlighted in red circle.	86
Figure 46. Crystalline phase of ZnO and ZnO-Ag fabricated at a carrier gas (O ₂ :N ₂) ratio of a) 0:1 and b) 1:0.....	87
Figure 47. The comparison of surface areas at various Ag contents and carrier gas ratios for the fabricated ZnO and ZnO-Ag nanoparticles.....	88
Figure 48. Reaction rate constant of ZnO and ZnO-Ag at different Ag contents and carrier gas ratios.....	89
Figure 49. Absorbance spectra of ZnO-Ag nanoparticles with different Ag content and O ₂ :N ₂ carrier gas ratios.	90

Blank page

List of Tables

Table 1. Modification of semiconductor-based nanomaterials	8
Table 2. Semiconductor-semiconductor based photocatalysts.....	10
Table 3. Semiconductor-metal heterojunction based photocatalyst.....	14
Table 4. Advantage and limitations of solid, liquid, and gas-phase methods	16
Table 5. XPS-analysis mass concentration of elements	51
Table 6. C 1s peak ratios of TiO ₂ annealed in air with different heating rates.....	72
Table 7. Previous studies on nanomaterials fabrication via spray pyrolysis.....	81

Blank page

Chapter 1

Introduction

1.1. Advanced oxidation process by photocatalysis

Environmental issues related to pollution have been exacerbated by human activities. Alternative solutions in wastewater treatment can be done by methods, such as advanced oxidation processes (AOPs). This method has emerged as a solution for addressing water pollution compared to traditional wastewater treatment methods such as adsorption, flocculation, and coagulation, which can be higher in operational expenses and the existence of additional streams for secondary waste. AOPs benefits includes, the accelerated degradation rate, mineralization or toxicity reduction of organic compounds, and function at room temperature and pressure [1].

AOPs involves the generation of highly oxidizing species, such as hydroxyl radicals ($\bullet\text{OH}$), which facilitate the degradation of organic compounds, possibly leading to complete mineralization. Several AOPs has been implemented in wastewater treatments, as explained by Paździor, et al. [2], such as (i) Fenton and photo-Fenton based reactions, (ii) electrochemical, (iii) photochemical, and others. Fenton-based reactions involve ferrous ions Fe^{2+} and their reaction with hydrogen peroxide (H_2O_2) in the decomposition process of organic compounds. Apart from Fenton-based reactions, electrochemical oxidation treatments have also been considered, where the degradation of organic pollutants takes place as a result of anodic activity.

Photocatalysis has attracted high attention as one of the photochemical AOPs, which involve the use of a nanomaterial semiconductor as a catalyst for the degradation of organic compounds. The process in photocatalysis follows [3]: 1) the diffusion of the

organic pollutant to the surface of the photocatalyst, 2) adsorption of the pollutants onto the surface of the photocatalyst, 3) degradation through oxidation or reduction of the adsorbed pollutant, 4) desorption of products from the surface of photocatalyst, and 5) removal of products from the interface region.

Photocatalysis involves activating a catalyst through light exposure. When the catalyst is irradiated with light, provided that the energy of the incident photons aligns with the band gap energy of the semiconductors, electrons undergo excitation from the valence band (VB) to the conduction band (CB). The electrons can instigate reduction reactions on the catalyst surface. Conversely, the resulting holes in the VB participate in oxidation reactions. The electron–hole separation and subsequent reaction can produce $\bullet\text{OH}$. These radicals can then oxidize organic compounds, potentially achieving complete mineralization. In instances where electron–hole pairs remain unused in photocatalytic reactions, they tend to recombine rapidly, releasing energy in the form of heat.

Chen et al., [4] has listed several advantages and limitation of traditional photocatalysis. They stated that photocatalysis is an environmentally friendly process, low-cost, and how easy it is to adjust catalyst loadings. However, there are still limitations of the process such as the difficulty in recovery and regeneration, effectiveness of degradation reduces because of excessive pollutants, and the potential of losses of the photocatalyst.

The effectiveness of a photocatalyst activity is influenced by its band gap energy, electronic structure, and ability to generate electron–holes [4]. The band gap energy should be tailored to extend light absorption into the visible spectrum, thereby efficiently harnessing light energy and increase the effectiveness of activity [5]. Besides the appropriate band gap energy, a photocatalyst should be selected based on its availability, surface area, cost, and physical and

chemical stability. Additionally, an ideal photocatalyst should be reliable under various reaction conditions and resistant to photocorrosion [6,7]. **Figure 1** highlights the essential characteristics of an excellent photocatalyst [8].

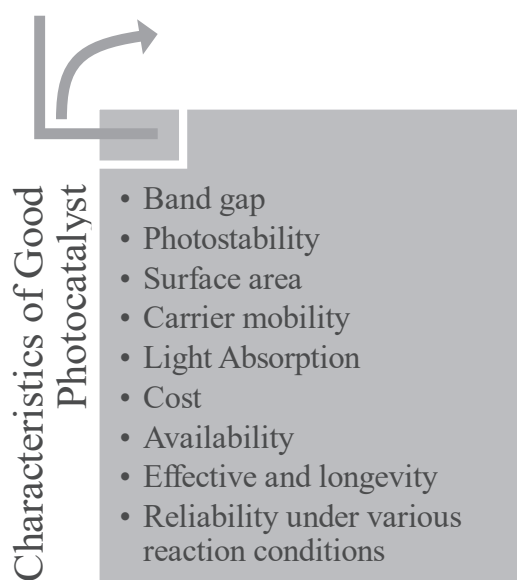


Figure 1. Characteristics of Good Photocatalyst. Adapted from [8].

1.2. Materials for photocatalysis

1.2.1. Characteristics of semiconductor-based photocatalyst

Photocatalysis involves the excitation of electrons of a photocatalyst that is irradiated with light. The light photons energy must have bigger energy compared to the band gap of the semiconductor to excite the electrons from the VB to the CB of the semiconductor. This phenomenon generates electron and hole pairs. A variety of these band gap energy can be seen in **Figure 2**, where the definition of the band gap energy is the energy gap between the filled VB to the empty conduction band of the semiconductor [9].

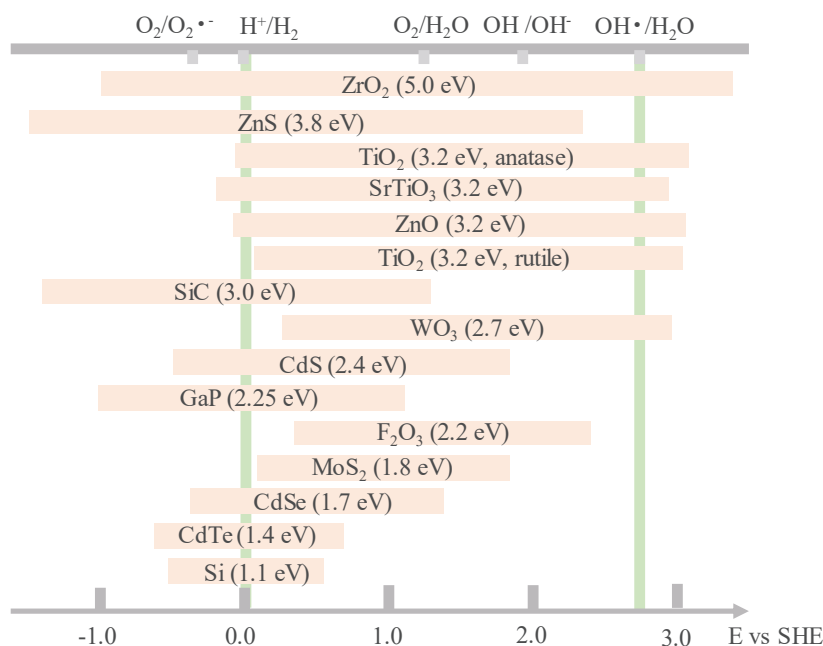


Figure 2. Band Gap Energy of Semiconductors. Adapted from [9].

Semiconductors (M_xO_y) such as TiO_2 and ZnO are eminently used as photocatalysts for the degradation of organic compounds. In photocatalysis the characteristics of the material, such as the crystallinity, morphology, and surface area, are important factors in achieving optimum applications. Additionally, to enhance the performance of M_xO_y , the introduction of either semiconductor or metal materials is utilized to tune its characteristics and improve the photocatalytic activity. The subsequent sections will introduce the materials used in this study.

1.2.1.1. TiO_2

TiO_2 , an n-type semiconductor, stands out as a pivotal material in photocatalytic applications due to its thermal and chemical stability, low toxicity, cost-effectiveness, and availability [10]. It has been studied for photocatalytic applications such as CO_2 conversion, degradation of organic pollutants, and water splitting. In nature, TiO_2 exists

in anatase, rutile, and brookite crystalline phases (**Figure 3**). The transformation from the anatase phase to the rutile phase may occur as the temperature rises [11]. Among these phases, anatase exhibits exceptional photocatalytic capabilities, particularly in generating $\bullet\text{OH}$ during photocatalysis.

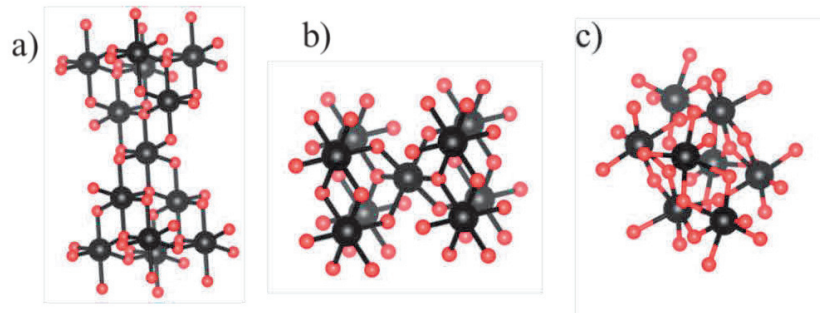


Figure 3. Crystal phases of TiO_2 : a) anatase, b) rutile, and brookite.

It was reported by Zhang et. al., [12] that anatase had the indirect band gap while rutile has direct band gaps (**Figure 4a**). Due to the indirect band gap of anatase TiO_2 it has a slower electron and hole recombination rate compared to rutile, which is the reason for the better photocatalytic performance. In addition, it was reported that because of the smaller size effective mass of anatase compared to rutile the photocatalytic activity is better (**Figure 4b**). The effective mass of electrons and holes is inversely proportional to the transfer rate of electrons and holes to migrate and transfer to the surface of the particles to participate in the photocatalytic degradation process.

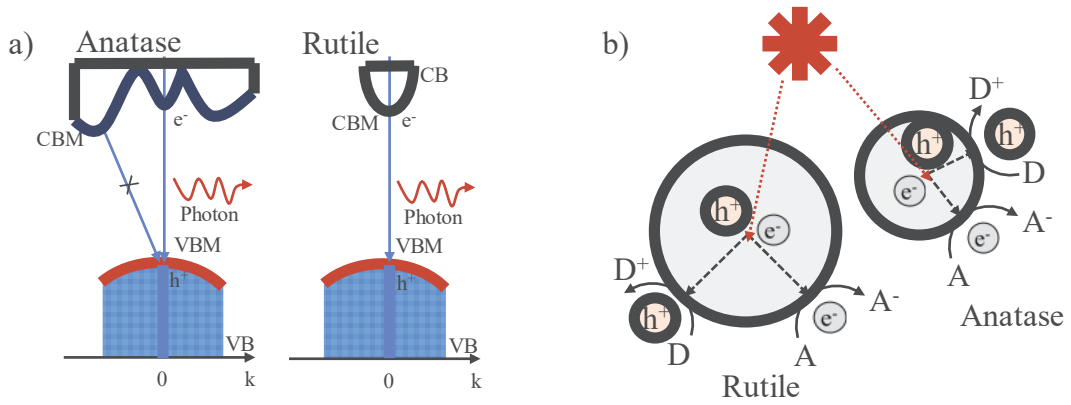
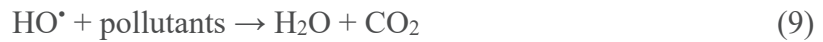
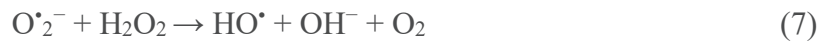
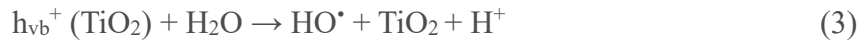


Figure 4. a) Comparison of recombination processes and b) transfer diagram of anatase and rutile. Adapted from [12].

Under UV light irradiation the photon energy from the light can excite the electrons of TiO_2 . The reaction that occurs follows eq. 1-10 [4]:



However, the UV region constitutes only a small portion ($\sim 4\%$) of the solar spectrum, restricting the practical applications of TiO_2 in daily life. This constraint arises from its wide bandgap (3.2 eV), which limits photoactivity under visible light and exacerbates rapid electron–hole recombination. Effective electron–hole recombination is needed for

the production of $\bullet\text{OH}$ that will react in degrading organic compounds.

Chen, et al, [4] stated several factors that decreases the photocatalytic efficiency of TiO_2 , such as 1) fast recombination rate of the electrons and holes, 2) poor affinity with organic pollutants, decreasing the adsorption to its surface, 3) aggregation, which can inhibit the active centers to absorb light irradiation, 4) higher scattering, 5) practicality in the recovery of the TiO_2 powder particles, which is well dispersed in the organic pollutant, 6) TiO_2 possess an initial high band energy. Potential modification strategies of TiO_2 such as doping of metal or non-metal materials, which can decrease the possible electron–hole recombination of TiO_2 [13].

1.2.1.2. ZnO

ZnO has attracted potential alternative from TiO_2 as a photocatalyst. It has a similar band gap energy (3.37 eV) with a higher absorbance in the visible light spectrum. The known crystal structure of ZnO is cubic rocksalt, cubic zinblende, and hexagonal wurtzite [1]. At ambient conditions, ZnO typically exists in the thermodynamically stable hexagonal wurtzite structure. Ong et al., [1] has explained several potential materials that can be added to ZnO which can increase the photocatalytic activity of ZnO, such as before in TiO_2 , with the addition of semiconductor (SnO_2 , Co_3O_4 , $\text{TiO}_{2x}\text{N}_y$) or even metal (Ag, Al, Mn) nanoparticles.

1.2.2. Enhancing the activity of photocatalysts

Several methods can be done to increase the photocatalytic activity of the semiconductor-based photocatalyst, which includes dye-sensitization, noble metal loading, transition metal doping, semiconductor heterojunction formation, and non-

metal doping [14]. Other researchers have done these modifications towards the semiconductor-based materials such as seen in **Table 1**. These modifications can increase the performance of the semiconductor-based materials. This study will focus on the semiconductor-semiconductor (**Section 1.2.2.1**) and semiconductor-metal heterojunctions (**Section 1.2.2.2**).

Table 1. Modification of semiconductor-based nanomaterials

Modification	Material	Application	Application Result Highlights	Ref.
Metal-doping	ZnO-Ag ZnO-Au	Photocatalysis	UV light irradiation (160 min) Methylene blue degradation ZnO = 8% ZnO-Ag (2 mol%) = 25% ZnO-Au (2 mol%) = 45%	[15]
Metal-doping	TiO ₂ -Ag	Water splitting	H ₂ production TiO ₂ = 206 mmol/g.h TiO ₂ -Ag (1.5 wt%) = 470 mmol/g.h	[16]
Non-metal doping	N-ZnO	Photocatalysis	Methylene blue degradation UV light irradiation (60 min) ZnO = 25% N-ZnO = 97% visible light irradiation (180 min) ZnO = 15% N-ZnO = 80%	[17]
Non-metal doping	N-TiO ₂	Photocatalysis	Methylene blue degradation UV light irradiation P25 = 0.032 l/min N-TiO ₂ (anatase) = 0.031 l/min N-TiO ₂ (anatase-rutile) = 0.095 l/min	[18]
Non-metal doping	TiO ₂ /rGO	Photocatalysis	UV light irradiation (240 min) Rhodamine 6G degradation TiO ₂ = 30.6% rGO = 10.9% TiO ₂ /rGO = 42.7-82.9%	[19]
Semiconductor coupling	ZnO/TiO ₂	Photocatalysis	UV light irradiation (120 min) Methylene blue degradation TiO ₂ = 84% TiO ₂ /ZnO = 92%	[20]

Semiconductor coupling	CuO-ZnO	Photocatalysis	Sun light irradiation Methylene blue degradation ZnO = 0.072 1/min CuO = 0.033 1/min CuO-ZnO= 0.022-0.099 1/min	[21]
------------------------	---------	----------------	---	------

1.2.2.1. Semiconductor-semiconductor heterojunctions

To enhance the electron separation process, it is possible to create a heterojunction, such as semiconductor-semiconductor heterojunctions, which can be categorized into three types (**Figure 5**) [13,22]. In Type I heterojunction the semiconductors should either be p- or n-type. For effective charge transfer, the CB of B should be higher, and its VB should be lower than that of A. This configuration ensures that both electrons and holes transfer to semiconductor A. In Type II, photogenerated electrons move from semiconductor B to A, while photogenerated holes move from A to B. This arrangement facilitates efficient separation of electron-hole pairs, making it highly advantageous. Type III heterojunctions are similar to Type II, except that there's a more pronounced difference in the positions of the VB and CB.

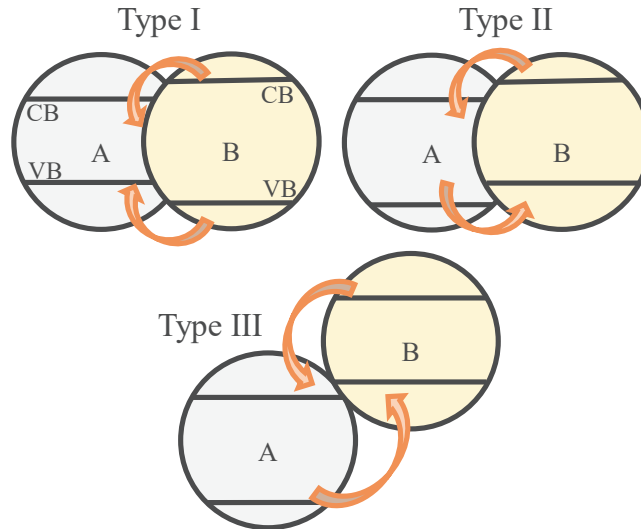


Figure 5. Schematic of the charges-carrier separation in three type combination systems of semiconductor-semiconductor heterojunction. Adapted from [13,22].

Various transition metal oxide semiconductors, including WO_3 , SiO_2 , Fe_2O_3 , and CuO , have been loaded to semiconductors, such as TiO_2 , to enhance its photocatalytic activity [23,24]. Furthermore, research has been carried out for its various applications, including hydrogen production [23], gas sensing [25], and degradation of pollutants through photocatalysis [26]. Several research of semiconductor-semiconductor heterojunction and its fabrication process and applications is summarized in **Table 2** and their respective morphologies in **Figure 6**.

Table 2. Semiconductor-semiconductor based photocatalysts

Materials	Application	Highlights	Ref.
TiO_2/CuO	Photocatalysis	Fabrication of ultrathin p-n heterojunction by thermal and ALD. Study of the photocatalytic mechanism in cationic/ionic dyes.	[26]

TiO ₂ /CuO	Gas sensing	Sensing of different gases showed the highest response to CO (50–800 ppm). Exhibits high selectivity at low temperatures (250 °C).	[25]
CuO-ZnO	Photocatalysis	Fabrication of copper doped ZnO by wet impregnation. Increase photodegradation of acid red 88 under visible light irradiation.	[27]
ZnO/TiO ₂	Photocatalysis	Fabricated by sol-gel method. Orange G was photodegraded by photocatalyst following the Network Kinetic Model.	[28]
WO ₃ /TiO ₂ /ZnO	Optoelectronic	Fabrication via RF-sputtering. Adjustability in optical and electrical characteristics based on layer composition and thickness.	[29]

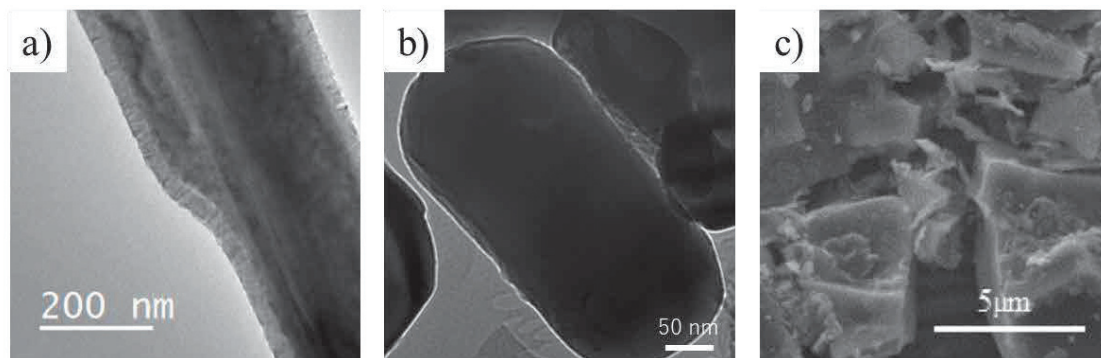


Figure 6. Morphology of a) TiO₂/CuO, b) CuO-ZnO, and c) ZnO/TiO₂. Adapted from [26–28].

Among these, copper oxides (Cu²⁺ and Cu¹⁺) is a candidate because it is economical, environmentally safe, abundance, and high activity [30–32]. When

combined with TiO₂, a well-known n-type semiconductor, CuO, which is a p-type semiconductor, forms a p–n heterojunction (Type II), leading to enhanced photocatalytic efficiency [26,33]. Several advantages stem from this heterojunction, primarily attributed to CuO:

1. Cu_xO has a bandgap energy (1.2–2.2 eV), thereby can extend light absorption to the visible spectrum [30,31]
2. By loading a lower-bandgap semiconductor like CuO, the electron–hole separation lifetime can be prolonged, lowering the electron–hole recombination [26,30]. This extended separation enables the production of •OH, which are essential for the degradation of pollutants through photocatalysis.
3. Furthermore, with the addition of H₂O₂, referred to as the Fenton process within AOPs, can enhance the generation of •OH. Cu-based materials demonstrate Fenton-like properties, enhancing their effectiveness in decomposing organic pollutants during wastewater treatment. [34].

The potential degradation mechanism can be elucidated using **Figure 7** for TiO₂-CuO/H₂O₂. As reported in a previous study [34], the introduction of CuO into TiO₂ forms a p–n heterojunction (Type II), as illustrated. Under light irradiation, electron–hole pairs are generated. Specifically, electrons excited from the VB of CuO are transferred to the CB of TiO₂. This transfer facilitates a Fenton-like reaction involving Cu²⁺ ions (depicted as green blocks) and photo-generated electrons (depicted as pink circles) with H₂O₂, effectively increasing the production of •OH, thereby enhancing the photocatalytic activity [34]. Additionally, the generated holes react with adsorbed water (H₂O) or surface hydroxyl (OH[−]) to form •OH [35,36].

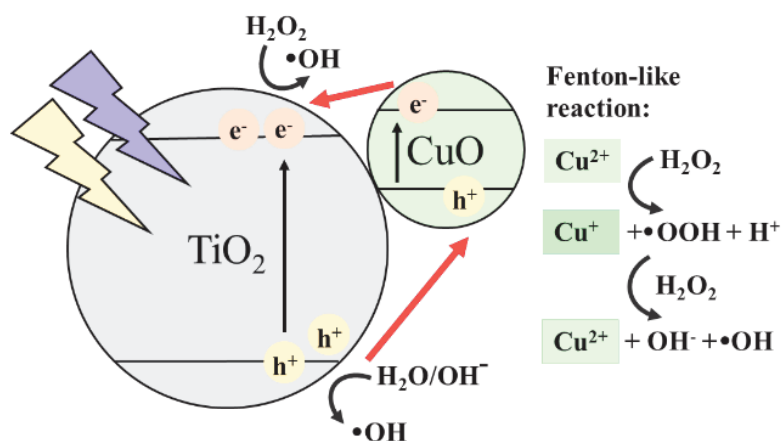


Figure 7. Schematic of hydroxyl radical formation by $\text{TiO}_2\text{-CuO}/\text{H}_2\text{O}_2$ under UV and visible light irradiation.

1.2.2.2. Semiconductor-metal heterojunction

Apart from the loading of semiconductors, the addition of metals also holds the potential to enhance the activity of semiconductor photocatalysts. Surface modification with noble metals like Ag, Cu, Pt, and Au can expand light absorption, thereby increasing photocatalytic activity in the visible light region [37,38]. **Table 3** and **Figure 8** shows several of these heterojunctions with their applications and morphologies. Under UV light irradiation, these metals can suppress the recombination of electrons–holes by being an electron sink for the excited electrons generated from the VB of the semiconductor (**Figure 9a**) [39]. Ag is regarded as a potential loading material due to its abundance and cost-effectiveness, particularly when compared to other highly stable noble metals.

Table 3. Semiconductor-metal heterojunction based photocatalyst

Materials	Application	Highlights	Ref.
TiO ₂ /Ag	Water Splitting	Fabrication by chemical reduction. Ag/TiO ₂ is more effective than TiO ₂ in water splitting. The impact of reaction time, photocatalyst loading, and the presence of sacrificial reagents (alcohols and sulfur) was analyzed.	[16]
Au-TiO ₂ , Ag-TiO ₂	DSSCs	Fabrication of novel double-layer films. The TiO ₂ -Ag NW DSSC showed higher efficiency. It is attributed to improved electron transport properties of Ag NW, strengthened light absorption, and intensified light scattering.	[40]
TiO ₂ /Ag	Photocatalysis	Fabricated by sol-gel method. Ag-doped TiO ₂ showed superior degradation of methylene blue (MB).	[10]
ZnO/Ag	Photocatalysis	Ag-modified ZnO exhibited enhanced visible light photocatalytic activity compared to ZnO, as demonstrated by the degradation of model organic dyes like MB and methyl orange.	[5]

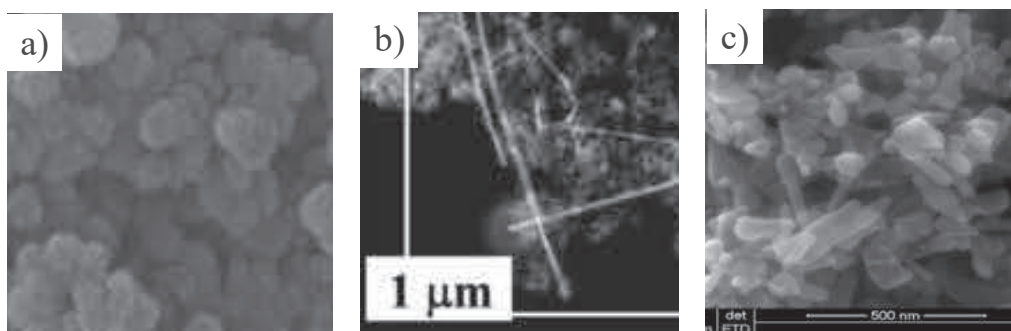


Figure 8. Morphology of a) TiO_2/Ag , b) $\text{TiO}_2\text{-Ag}$ NWs, and c) ZnO/Ag . Adapted from [5,16,40].

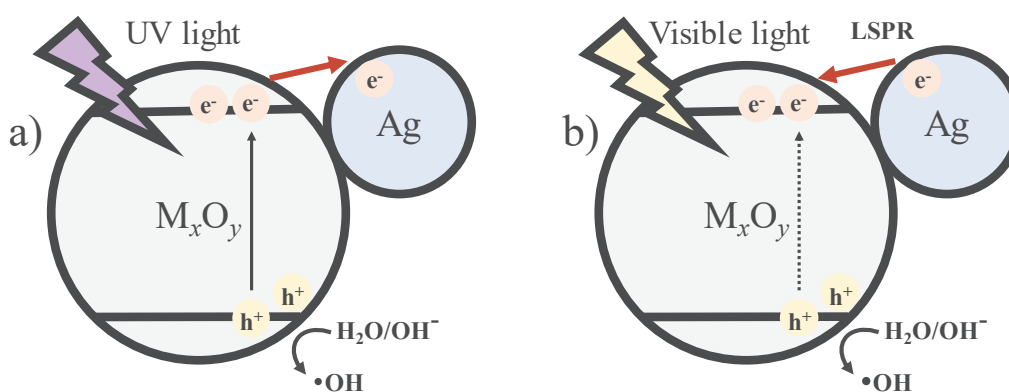


Figure 9. Schematic of carrier-charge separation of semiconductor and Ag under a) UV and b) visible light irradiations.

Loaded metals display a distinct effect due to localized surface plasmon resonance (LSPR), characterized by the oscillation of free electrons within metallic nanoparticles [16]. These energetic electrons are transferred into the CB of the semiconductor due to the presence of a Schottky barrier. The Schottky barrier between noble metals and semiconductor oxides occurs through Fermi level equilibrium, leading to the establishment of a built-in electric field at the interface [13]. This electric field facilitates the separation of photogenerated charges, such as seen in **Figure 9b**. LSPR

activation contributes to the enhancement of visible-light-driven photocatalytic activity. It facilitates the extension of the photocatalyst light-harvesting capability to longer wavelengths, enhances light scattering, and promotes direct electron transfer from the metal to the semiconductor, thereby increasing the photocatalyst activity in the visible light region.

1.3. Methods of fabrication

In this section, methods for the fabrication of photocatalysts will be introduced. It encompasses solid, liquid, and gas-phase methods in the fabrication process. A brief comparison can be seen in **Table 4**.

Table 4. Advantage and limitations of solid, liquid, and gas-phase methods

Preparation	Advantages	Limitations
Solid-phase method	Simple process, cost-effective	Time-consuming and achieving uniform particle size distribution
Liquid-phase method	Better control of the whole reaction parameters, low-cost, easily applied to any substrate.	The usage of solvents and consist of several steps in laboratory practice.
Gas-phase method	Control of nanoparticles microstructure; growth, purity, uniformity, and has good step coverage. Furthermore, it is scalable to larger process.	Control of reaction parameter and chemical compositions

1.3.1. Solid-phase method for fabricating nanomaterials

Solid-phase metho typically involves the production of materials without the

involvement of liquid or solvents. Furthermore, the precursors are solid substances that undergo physical or chemical transformation in solid state. Mechanical milling stands out as one of the straightforward and cost-effective methods, offering significant technical benefits in the fabrication of diverse nanomaterials and nanocomposites. A multitude of researchers have employed ball milling for this purpose. During milling, several phenomena may occur, including the generation of structural defects, mechanical alloying, phase transformations, and particle refinement [41].

Rinaudo, et al., [41] used titanium oxide (IV) with a purity of 99% (Biopack) as the starting material for the synthesis. High-energy ball milling was conducted using a planetary ball mill, equipped with an 80 cm³ WC vial and 15 mm WC balls. Milling was carried out under ambient air conditions. The milling process was conducted for various time periods. Such as seen in **Figure 10**, high-energy ball milling enables the preparation of titania supports with customizable phase compositions. This process generated grain boundaries and interfaces during polymorphic transformation, which has the potential to enhance the adsorption properties. Additionally, particle refinement resulted in the increase of the external surface area. In addition, prolonged milling time increases the oxygen vacancies.

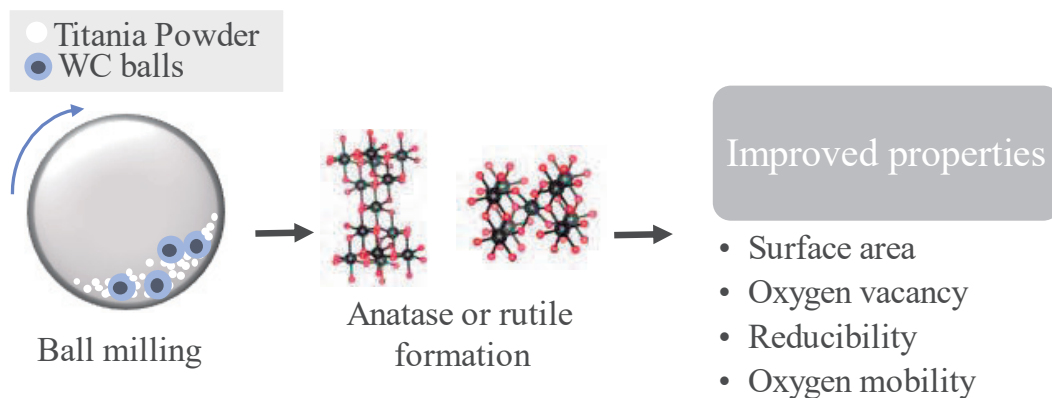


Figure 10. Preparation of TiO₂ by ball-milling. Adapted from [41].

1.3.2. Liquid-phase method for fabricating nanomaterials

Liquid-phase methods are known to be a simple approach in the fabrication of nanomaterials. The liquid-phase method involves the fabrication of materials where the precursor is prepared by dissolving, dispersing, or suspending the substance. During synthesis, chemical reaction occurs in a liquid state. Liquid-phase methods include sol-gel, hydrothermal, precipitation, solvothermal, electrochemical deposition, wet chemical, and electrospinning. This route enables easy control of the morphology of nanostructures by manipulating experimental factors such as the type of solvents, starting materials, and reaction conditions.

Figure 11 exhibits the morphology of the fabricated nanoparticles by the hydrothermal and sol-gel methods. Abbad, et al., [42] fabricated TiO₂ and Ag-doped TiO₂ nanopowder by sol-gel method. Initially, titanium tetra n-butoxide was dissolved in acetic acid, and then distilled water was added dropwise to the mixture. This gel was subsequently dried. The resulting material was ground in a mortar and annealed. For the preparation of Ag-doped TiO₂, AgNO₃ was added to water in calculated amounts to achieve different Ag contents. The morphology can be seen in **Figure 11a** and **b**, TiO₂

reveals cuboid-shaped TiO_2 particles with a size of 18 nm. In Ag-doped TiO_2 , the images show the presence of spherical Ag particles. The black spots observed can be attributed to silver metallic particles.

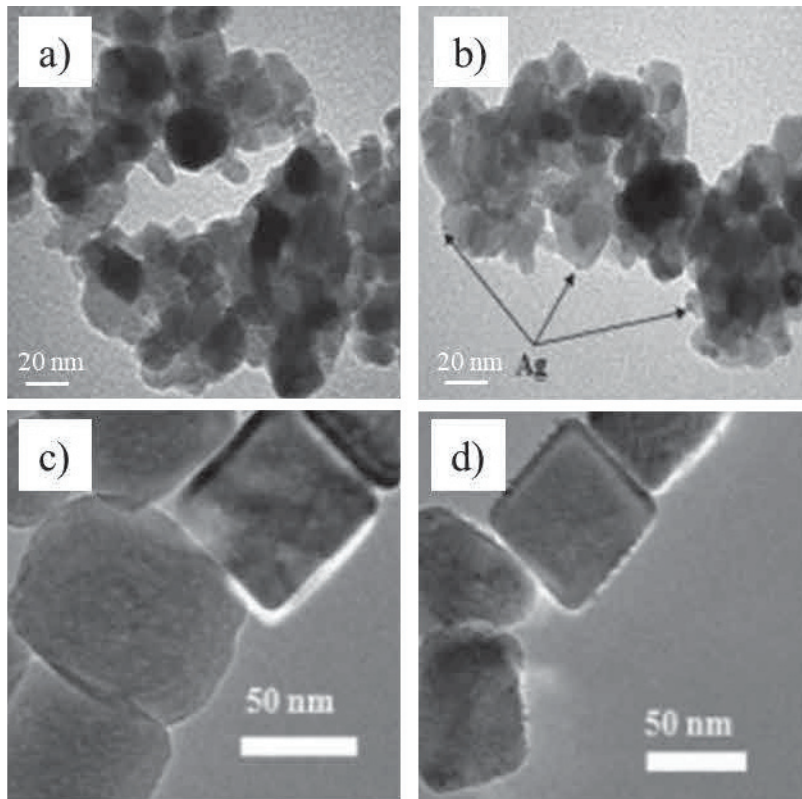


Figure 11. Morphology of a) TiO_2 and b,c,d) TiO_2/Ag fabricated by a,b) sol-gel and c,d) hydrothermal methods. Adapted from [42,43].

Zhang, et al., [43] fabricated TiO_2 nanostructures with the modification of silver nanoparticles with different contents of Ag (1–3 mol%) using a one-step hydrothermal method. In the fabrication process, TBAH ($\text{C}_{16}\text{H}_{37}\text{NO}$) and DEA ($\text{HO}(\text{CH}_2)_2\text{NH}(\text{CH}_2)_2\text{OH}$) were mixed. Subsequently, TTIP was slowly added dropwise to the solution and stirred uniformly. AgNO_3 particles were then added to the solution with varying mole ratios and stirred. The resulting solution was transferred to Teflon-lined stainless-steel autoclave and heated. The products were centrifuged with HCl,

followed by washing ethanol and distilled water. Afterward, the products were dried and then exposed to a xenon lamp to photoreduce Ag ions into metallic Ag. The morphology of the hydrothermal-synthesized TiO₂/Ag at 1 and 3 mol% Ag content can be seen in **Figure 11c** and **d**, respectively. TiO₂ nanoparticles exhibit cube-like morphology. With the increase of Ag content, small dark spots that correspond to Ag can be seen on the surface of TiO₂. In addition, the SAED patterns **Figure 11c** and **d** (inset) show the sharpness of the concentric rings increases with the higher Ag content.

1.3.3. Gas-phase method for fabricating nanomaterials

Gas-phase method involves the formation of materials in gas. The precursors are typically gas or vapor. Throughout the process, chemical and physical changes occur in the gas state. Gas-phase fabrication can happen through either a chemical or physical process, referred to as chemical vapor deposition (CVD) and physical vapor deposition (PVD), respectively.

The gas-phase method is a highly regarded route for fabricating nanoparticles. This method is considered superior to the liquid-phase method due to its simple synthesis steps, easy collection of nanoparticles, absence of liquid by-products, and production of high-purity materials [44–46]. Utilizing the gas-phase method for fabrication can simplify the production of nanoparticles, nanocomposite materials [47], and nanoalloys [48] in a one-step process. Various gas-phase methods, such as flame spray pyrolysis [44], plasma-enhanced chemical vapor deposition (PECVD) [49], spark ablation [50], and spray pyrolysis (SP) [51] have been employed to produce nanoparticles. Jamkhande et al. [52] and Kruis et al. [46] have described the advantages, disadvantages, and applications of gas-phase methods for nanoparticle preparation. The

gas-phase route has advanced to produce materials for applications such as pigments, catalysts, gas sensors, fuel cells, and more [47]. Producing nanoparticles via the gas-phase method not only simplifies the synthesis process but also enhances the characteristics of the resulting materials.

1.3.3.1. Chemical vapor deposition (CVD)

CVD method refers to the fabrication of materials in the gas form, which involves chemical reactions. Processes such as the PECVD and SP are some examples of the CVD process.

1.3.3.1.1. Spray pyrolysis (SP)

SP is a well-suited gas-phase method for producing nanoparticles and composites in a one-step method. Sriram, et al [51] have comprehensively elucidated the SP method and its prospects in metal oxide-based materials. The SP method offers the possibility to fabricate materials with diverse morphologies, further broadening their potential applications in areas such as photocatalysis, gas sensors [53], and more. The formation of nanoparticles and the resulting morphology is influenced by various parameters, including the evaporation rate of the solvent, carrier gas ratios, flow rate, and the concentration of the precursor [51].

Dermenci, et al., [54] fabricated ZnO/Ag nanocomposite particles by SP system such as seen in **Figure 12a**. The precursor solution was atomized using an ultrasonic atomizer. The aerosol stream flown into a horizontal quartz reactor that is heated by a furnace. Upon decomposition of the aerosol droplets, the resulting particles were collected in bottles connected to the outlet of the quartz reactor and stored in ethanol. The submicron-sized, spherical morphology of the particles can be confirmed through

SEM analysis, as shown in **Figure 12b**. These particles, referred to as secondary particles, are aggregates of nano-sized primary particles.

Haugen, et. al., [37] has also use SP for the fabrication of TiO₂-based materials. **Figure 12c** shows that hollow spherical nanoparticles was produced, a result of the atomization-evaporation sequence occurring during the SP process. These morphological characteristics are attributed to the compression and decomposition of the precursor in the tubular furnace [55].

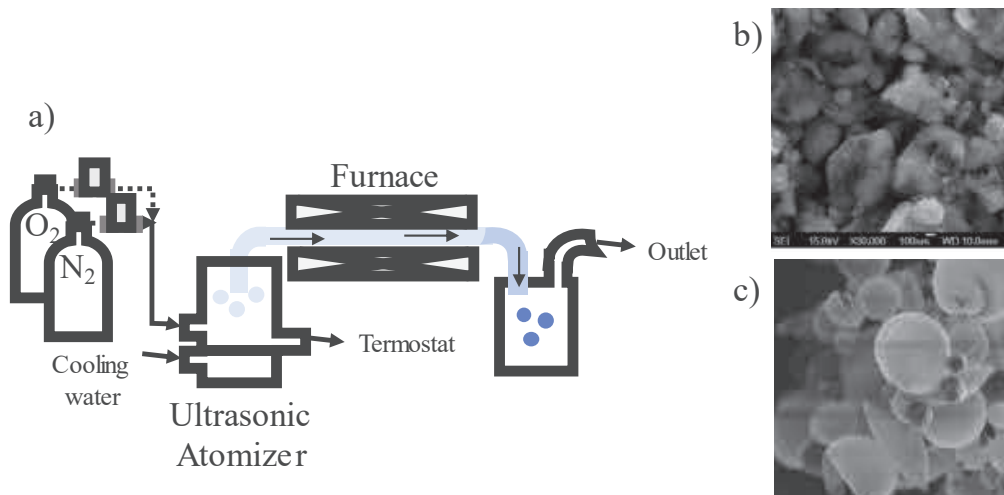


Figure 12. a) Schematic of spray pyrolysis experimental set-up; morphology of b) Ag/ZnO and c) TiO₂ nanoparticles fabricated by spray pyrolysis. Adapted from [37,54].

1.3.3.2. Plasma-enhanced chemical vapor deposition (PECVD)

PECVD method is advantageous as it requires significantly lower temperatures compared to other methods, making it feasible to deposit coatings onto temperature-sensitive substrates. PECVD is a method that employs electrical energy as an activating source to generate ionized species and radicals from gases and/or vapors, forming plasma [56].

PECVD, as a gas-phase method, facilitates the formation of nanomaterials through

the interaction of electrons generated from plasma, leading to the dissociation of precursor molecules introduced into the plasma reactor. PECVD offers several advantages such as lower deposition temperature, high material purity, and precise control over fabrication parameters. This method enables the fabrication of layered thin films through flight-coating processes [36] and nanoparticulate thin films [37], depending on the specific fabrication setup and parameters.

1.3.3.3. Physical vapor deposition (PVD)

In the PVD method, nanoparticles that are typically fabricated through evaporation-condensation, often conducted using a tube furnace under atmospheric pressure. Jung, et. al., [57] attempted the synthesis of Ag metal nanoparticles. Such seen in **Figure 13a**, the experimental setup consisted of parts to: (i) synthesize metal nanoparticles through aerosol generation, and (ii) sampling and measuring the nanoparticles. Ag nanoparticles were successfully fabricated and remained stable for extended durations. Increased surface temperatures resulted in higher values of geometric mean diameter, geometric standard deviation, and total number concentration. TEM images revealed the presence of spherical and non-agglomerated nanoparticles, even at high concentrations and elevated heater surface temperatures. Notably, the generated Ag nanoparticles were found to be pure Ag without any oxide species.

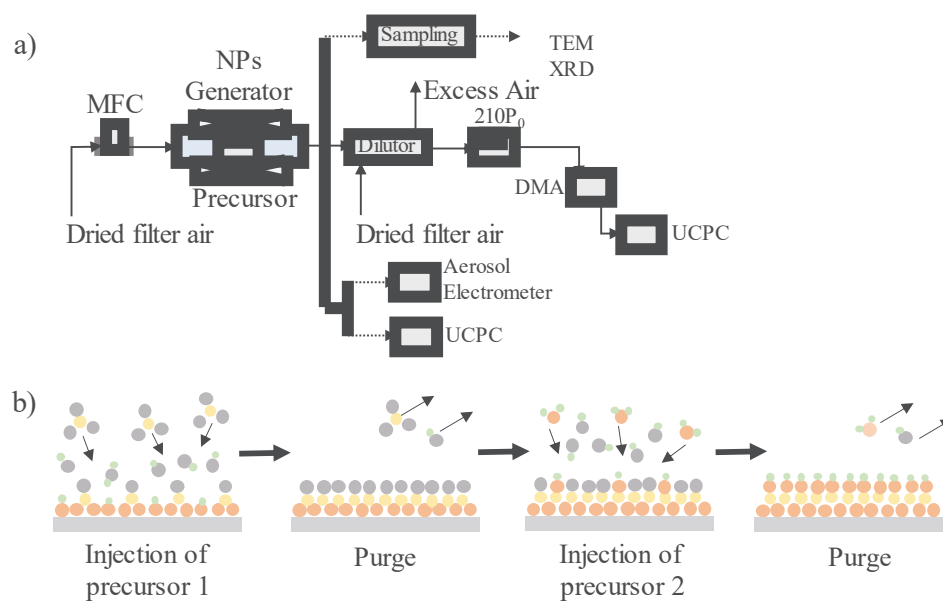


Figure 13. Schematic of a) simplified evaporation-condensation experimental setup and b) nanoparticles deposition process by ALD. Adapted from [57,58].

Another PVD method is the atomic layer deposition process. It is a deposition method used to fabricate thin film materials with exceptional conformality. It relies on self-limiting reactions between two gaseous precursors, facilitating the deposition of thin films in a layer-by-layer manner such as seen in **Figure 13b**. Initially, a precursor is introduced into the reactor chamber where it reacts with the substrate's surface groups. Next, inert gas purging or pumping removes unreacted precursors and by-products. A second precursor is then introduced to react with the adsorbed molecules. Finally, the system is purged or pumped to eliminate unreacted precursors and by-products. This cycle deposits one monolayer, and it is repeated until the desired thickness is achieved [58].

1.4. Advancement of the fabrication and application of photocatalyst

The liquid-phase preparation method offers the benefit of generating monodisperse and non-agglomerated nanoparticles. However, it has drawbacks including a complex fabrication process, generation of liquid waste, lower purity, and limited production quantity of nanomaterials. In contrast, gas-phase methods, such as SP, evaporation-condensation PVD, ALD and PECVD, offer significant advantages. These methods allow for precise control over the characteristics of the produced nanomaterials (size, crystallinity, purity, and uniformity) while minimizing environmental impact. Importantly, these processes can produce nanomaterials in a one-step manner and are suitable for large-scale production.

In our previous studies by the PECVD method [49,59,60], it allows for the production of porous nanoparticulate thin films with minimal agglomeration. Such morphology offers the advantage of increased surface area, enhancing the potential applications of the resulting nanomaterials. Thin films are particularly suitable for practical applications compared to powder materials, as they can be more conveniently reused without the need for complex recovery processes such when using powder nanoparticles.

A thin film is defined to be a layer that extends indefinitely in two dimensions but is limited to the third dimension, with thicknesses ranging from several nanometers to a few micrometers [61]. The properties of thin films are largely determined by their structure, while their mechanical and thermal properties are influenced by the reaction conditions and deposition methods. **Figure 14** provides an overview of the classification of thin film deposition methods, which are divided into physical and chemical methods. Several of these methods were explained in the previous sections.

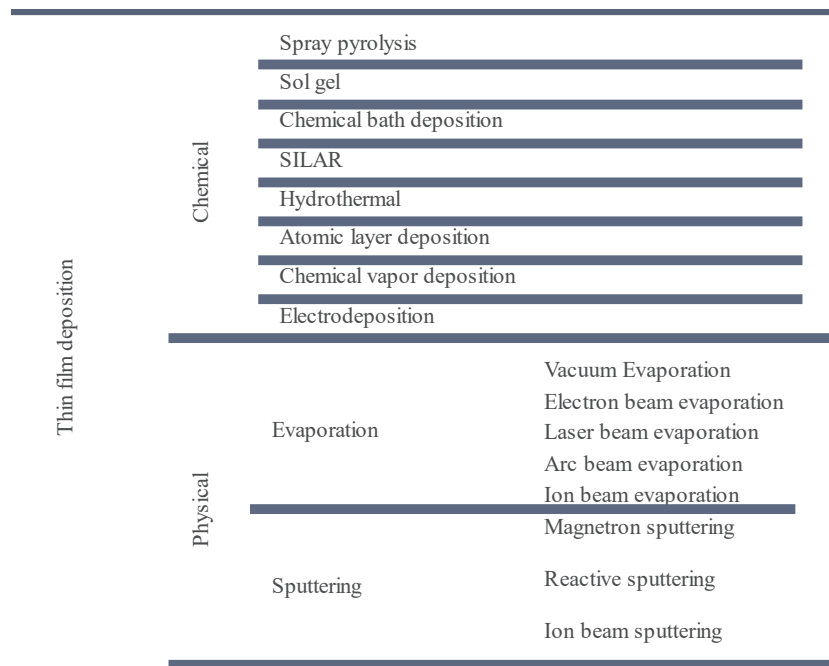


Figure 14. Classification of thin-film deposition methods. Adapted from [61].

1.4.1. Post-deposition heat treatments

In our previous studies [49,59,60] TiO₂ nanoparticulate thin films were fabricated. Given the amorphous nature of the TiO₂ nanoparticles obtained through PECVD deposition, post-deposition heat treatments were applied. The effects of post-annealing heat treatment on film characteristics and activity has already been studied [11,62]. The anatase phase shows the highest activity compared to rutile and brookite phases. For TiO₂ films, the transformation from amorphous to anatase occurred at 400 °C, followed by nanoparticle coalescence. At temperatures above 1000 °C, anatase transformed into rutile, leading to film densification and decrease thickness.

Heat treatment at a specific temperature can facilitate nanoparticle crystallization, alter film thickness, and influence film absorbance. The comparison of crystal phase changes in thin films reveals that phase transformation of TiO₂ is influenced by

deposition process variables, morphology, residues of amorphous TiO₂ nanoparticles obtained under different fabrication parameters, and plasma reactor design. Densification of thin films was confirmed in all samples subjected to heat treatment.

Other than the applied annealing temperatures, the set heating rates for annealing have also been found to affect the characteristics of the produced nanoparticles. The annealing process has been noted to have a significant impact on various characteristics of nanoparticles, including grain growth [63], crystal size [64], and crystal orientation [65]. Modifying this parameter presents an opportunity to fine-tune the activity of the nanoparticles for optimal performance.

1.4.2. Addition of foreign materials by a one-step gas-phase method

The gas-phase method versatility has led to advancements in fabricating nanocomposites with enhanced characteristics compared to pristine substances. Incorporation of foreign materials such as Ag nanoparticles via a one-step gas-phase method has been studied [62]. To simplify the fabrication process of Ag-loaded TiO₂ nanoparticulate thin film, a PECVD-PVD one-step gas-phase system was employed.

The addition of Ag to TiO₂ reduced the temperature at which the anatase-to-rutile transformation occurred, influenced by metal-induced crystallization. Additionally, higher Ag content promoted TiO₂ nanoparticle growth during annealing. When the performance was observed, optimal photocatalytic activity for MB degradation under UV irradiation was for TiO₂-Ag annealed at 700 °C, attributed to synergistic effects of anatase-rutile TiO₂ and loaded Ag metals. The coexistence of anatase and rutile TiO₂ prolonged electron-hole separation, enhancing photocatalytic activity.

Other materials such as clearly elucidated in **Section 1.2**, can be used in

photocatalysis and by the usage of a one-step gas-phase system such material can be easily produced. The resulting nanocomposites, including TiO₂-Cu_xO [66], TiO₂/Au or TiO₂/Ag [37], are anticipated to enhance the photocatalytic activity of TiO₂. Additionally, alternative materials such as WO₃ and ZnO show promise as candidates [24].

Furthermore, in the fabrication process of nanocomposites, methods stated in **Section 1.3.3** can be used to fabricate these materials. SP as a gas-phase method has the potential to fabricate composites in a simple one-step process. Materials that have been successfully fabricated by SP are ZnO/CuO, TiO₂/Ag, TiO₂/Au, and ZnO/Ag [37,54,55].

1.4.3. Photocatalytic test conditions

Under UV light irradiation, the activity of TiO₂-Ag showed an increase compared to TiO₂ nanoparticulate thin film. Additionally, the addition of Ag enhanced the activity in the visible light region (higher wavelength of light irradiation). In our previous study, the optimum content of loaded Ag was 2.2 wt. % for photocatalytic degradation under UV light irradiations [60].

In investigating the photocatalyst and its properties, other factors need to be taken into account within the photocatalytic degradation system. Such as seen in **Figure 9** the charge separation within the semiconductor-metal heterojunction undergoes changes under light irradiation. Furthermore, evaluating the performance of the photocatalyst under visible light exposure is essential to ensure its suitability for everyday applications.

Other than that, the condition in the photocatalytic system has also been viewed to

influenced and optimized the photocatalytic activity, such as the pH of the system [67]. pH significantly influences the surface charge properties of nanomaterials and the formation of $\bullet\text{OH}$, affecting photocatalytic activity. For instance, for TiO_2 nanoparticles, at neutral or high pH, $\bullet\text{OH}$ are the primary species, while at low pH, positive holes dominate oxidation reactions. TiO_2 can be protonated in acidic conditions (eq. 11) and de-protonated in alkaline conditions (eq. 12) [9].



The point of zero charge for TiO_2 ranges from 4.5 to 7. Below this value, the surface of nano TiO_2 becomes positively charged, enhancing the adsorption of negatively charged contaminants and boosting photocatalytic reactions. Conversely, above this value, the surface is negatively charged, favoring the absorption of positively charged contaminants.

Additionally, the addition of substances such as H_2O_2 can further enhance the photocatalytic activity. Acting as an electron scavenger, H_2O_2 optimizes the separation and utilization of the generated electron-hole pairs during the degradation process of organic compounds. Moreover, under UV light exposure, H_2O_2 undergoes degradation, leading to the production of additional $\bullet\text{OH}$, which are instrumental in the degradation of organic dyes [68].

1.5. Objectives and outline of dissertation

In this dissertation, semiconductor-based photocatalysts were fabricated via one-step gas-phase method, specifically utilizing a one-step PECVD-PVD and SP method. These methods were employed to fabricate photocatalyst of semiconductor-based materials such as TiO_2 and ZnO . Loaded materials, such as CuO and Ag , were

incorporated into the semiconductor-based photocatalyst structures to potentially enhance their characteristics and photocatalytic activity. This dissertation is structured into five chapters as can be seen in **Figure 15**, each delving into specific aspects of the one-step fabrication method, characterization, and applications of the photocatalytic materials.

Chapter 1 elaborates the motivations driving the progress of AOPs, exploring the materials utilized, and the diverse process employed in the fabrication of nanomaterials. This comprehensive examination shed light on the multifaceted landscape of AOPs, offering an understanding of its significance, the materials employed, and the processes available in nanomaterial fabrication.

Chapter 2 is divided into two sub-topics. Initially, TiO₂-CuO nanoparticulate thin films were produced through a single-step PECVD-PVD method, and its photocatalytic activity was assessed concerning the crystalline phase (anatase or rutile) when exposed to visible light. It was found that the photocatalytic activity of (rutile) TiO₂-CuO was higher compared to all samples. Secondly, a more detailed examination was carried out on the (anatase) TiO₂-CuO film. The test was conducted with the addition of H₂O₂ aimed at enhancing photocatalytic activity. Moreover, parameters such as variations in UV or visible light exposure and pH were investigated.

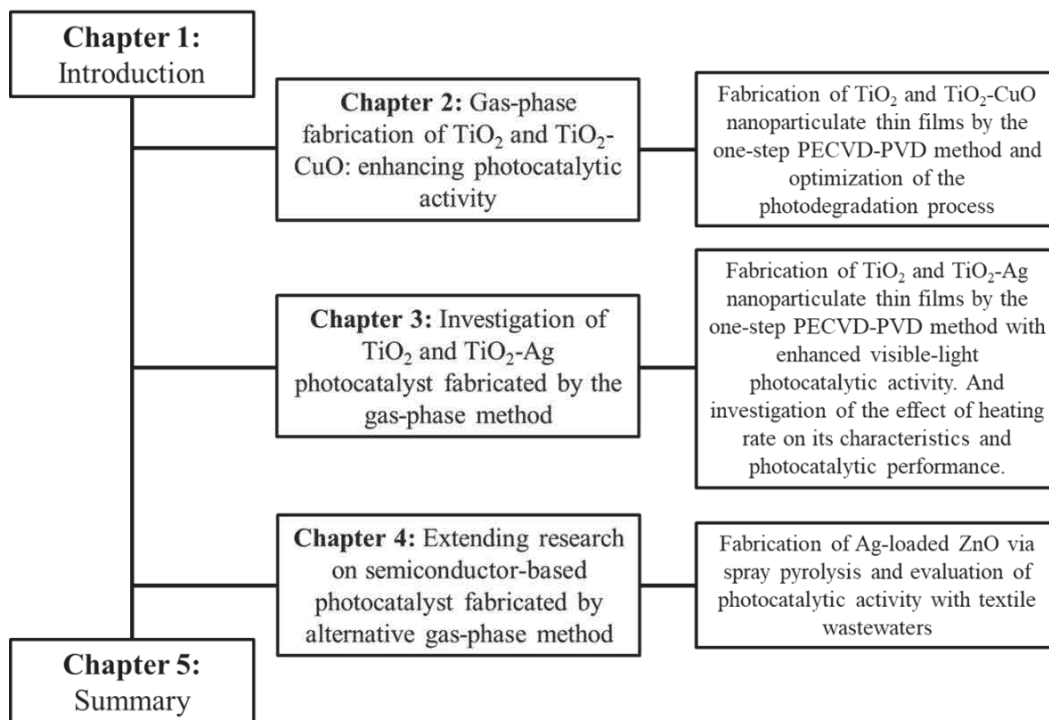


Figure 15. Diagrammatic illustration of the objective of this dissertation.

Apart from the semiconductor-semiconductor photocatalyst, the addition of noble metal has potential in increasing the photocatalytic activity. Previous studies in our laboratory have explored the fabrication and activity under UV light irradiation [60] and the effect of annealing temperatures for TiO₂-Ag nanoparticulate thin films [62]. Nevertheless, there is still room for further enhancements and investigations. In **Chapter 3** two key areas are explored. Firstly, it examines the production of Ag-loaded TiO₂ using a gas-phase system and the photocatalytic activity was evaluated under visible light irradiation. Secondly, it assesses a more detailed impact of the heating rate of annealing towards the characteristics and activity of TiO₂-Ag.

In addition to the one-step PECVD-PVD method and TiO₂-based materials discussed, there are still other fabrication methods and materials to explore, such stated

in **Chapter 1**. **Chapter 4** broadens the potential fabrication of the semiconductor-based photocatalyst through the fabrication of ZnO and ZnO-Ag nanoparticles by a one-step SP method. The photocatalytic activity was tested for direct applications in the degradation of textile wastewater under UV light irradiation.

Chapter 5 Summarizes the findings and activity from all chapters and suggests future research directions.

Chapter 2

Gas-phase Fabrication of TiO₂ and TiO₂-CuO: Enhancing Photocatalytic Activity

Abstract

This chapter discusses the fabrication of TiO₂ and TiO₂-CuO nanoparticulate thin films using a one-step gas-phase method, which utilized plasma-enhanced chemical vapor deposition and evaporation-condensation physical vapor deposition method, for TiO₂ and CuO, respectively. The produced films consisted of spherical TiO₂ nanoparticles with visible CuO on the surface of TiO₂ nanoparticles. Annealing in air resulted in the crystallization of TiO₂ and complete oxidation of CuO. Additionally, the increase of annealing temperature ranging from 400 to 800 °C transformed the crystal phase of TiO₂ from anatase to rutile and increased the size of the nanoparticles. The photocatalytic activity tests were conducted for the degradation of Rhodamine 6G. The photocatalytic activity of rutile- TiO₂/CuO exhibits better performance compared to anatase- TiO₂/CuO under visible light irradiation. Furthermore, for anatase- TiO₂ samples, H₂O₂ was added to improve the degradation process. Additionally, this study examines the impact of pH on photocatalytic activity. Anatase- TiO₂-CuO/H₂O₂ exhibited the highest photocatalytic activity at pH 13, achieving a reaction rate constant of 0.99 h⁻¹cm⁻² after 180 min of visible light irradiation. These findings have significant implications for advancing the usage of nanoparticulate thin films in wastewater treatment by enhancing pollutant degradation.

2.1. Introduction

AOPs, such as photocatalysis, is seen as a more efficient solutions compared to traditional methods in remediation due to its ability to completely degrade organic compounds in wastewaters by the generation of highly reactive $\bullet\text{OH}$ that can break down organic pollutants to the extent of complete mineralization. TiO_2 is a popular material in photocatalysis because of its stability, safety, and cost-effectiveness. However, its wide bandgap limits its activity to the UV region of the spectrum. To enhance its activity, various transition metal oxides like Cu_xO have been combined with TiO_2 to increase its activity, such explained in **Chapter 1**. Cu_xO , being economical and environmentally friendly, is a suitable candidate as a loading material to TiO_2 , by the formation of a p–n heterojunction, which in the photodegradation process can improve the charge separation.

In our previous studies on different annealing temperatures for TiO_2 and $\text{TiO}_2\text{-Ag}$ nanoparticulate thin films annealed in N_2 atmosphere [11,62], variations in the characteristics of the produced films such as the size of nanoparticles, crystal phase, and porosity; consequently, the photocatalytic activity. However, samples annealed in air and loaded with Cu_xO have not been studied.

Higher annealing temperatures, anatase shifts to rutile. While the anatase phase exhibited high activity, a study [69] suggested that Cu_xO -loaded rutile- TiO_2 displayed greater activity compared to anatase- TiO_2 , attributed to its distinct characteristics and electron–hole separation process.

Further engineering in the photocatalytic system can be explored. Several studies [68,70,71] have proposed a cost-effective method that involves enhancing the photocatalytic degradation with the aid of H_2O_2 . Additionally, in wastewater treatment

applications, the solution pH exerts significant influence on the decontamination process as it affects catalyst surfaces, organic dye properties, and reaction kinetics [71,72]. Exploring factors such as pH adjustments and the addition of H₂O₂ could offer further insights into optimizing the process.

In the fabrication process, despite its advantages, traditional fabrication methods involving liquid-phase method have limitations such as multiple steps, liquid waste generation, and small-scale production. Gas-phase preparation, like PECVD, offers a solution by enabling the creation of well-dispersed nanoparticulate thin films, which have a larger surface area and are more conducive to mass transfer. By incorporating an evaporation-condensation PVD system, Cu_xO can be loaded onto TiO₂ nanoparticles in a one-step process.

Section 2.5.1 delves into the fabrication and characterization of Cu_xO-loaded anatase- or rutile- TiO₂ by the one-step PECVD-PVD and its photocatalytic activity were evaluated under visible light irradiation. **Section 2.5.2** further studies the characteristics of anatase- TiO₂-Cu_xO and its photocatalytic activity with the addition of H₂O₂. Additionally, factors such as changes in UV or visible light exposure and pH were explored during the test.

2.2. Materials and experimental setup

The setup for producing TiO₂ and TiO₂-Cu_xO nanoparticulate thin films is illustrated in **Figure 16**. TiO₂ nanoparticles were formed by the PECVD reactor. Titanium tetraisopropoxide (TTIP; Kanto Chemical Co.), as the precursor, was fed into the plasma reactor with a radio frequency supply (AX-1000IIP; Adtec Plasma Technology Co., Ltd.) at 13.56 MHz and 100 W. Ar gas served as the carrier gas for the

system, with a bubbling flow rate of 40 sccm for TTIP, and diluter flow rates of 350 and 100 sccm were employed when the PVD system was in operational and idle, respectively. Concurrently, Cu_xO nanoparticles were generated in the PVD system through the evaporation of Cu chips (99.9% Cu, Nacalai Tesque, Inc.) at 1350 °C (Section 2.5.1) and 1400 °C (Section 2.5.2) inside a tubular furnace (FT-01VAC-1630, Full-Tech Co., Ltd.). The vapor was flown by a carrier gas and rapidly condensed to form nanoparticles inside the tubes covered by the cooling water system. For TiO_2 or Cu_xO samples, PECVD and PVD systems were operated separately. However, for TiO_2 - Cu_xO deposition, both systems were run simultaneously, depositing the nanoparticles onto a Si substrate with an applied +500 V. The pressure of the system was kept between 0.7–1.5 kPa. The films obtained were annealed in air atmosphere, with a constant heating rate of 5 °C/min, until reaching the set temperature. The temperature then held at this temperature for 3 h to oxidize Cu_xO and crystallize TiO_2 nanoparticles.

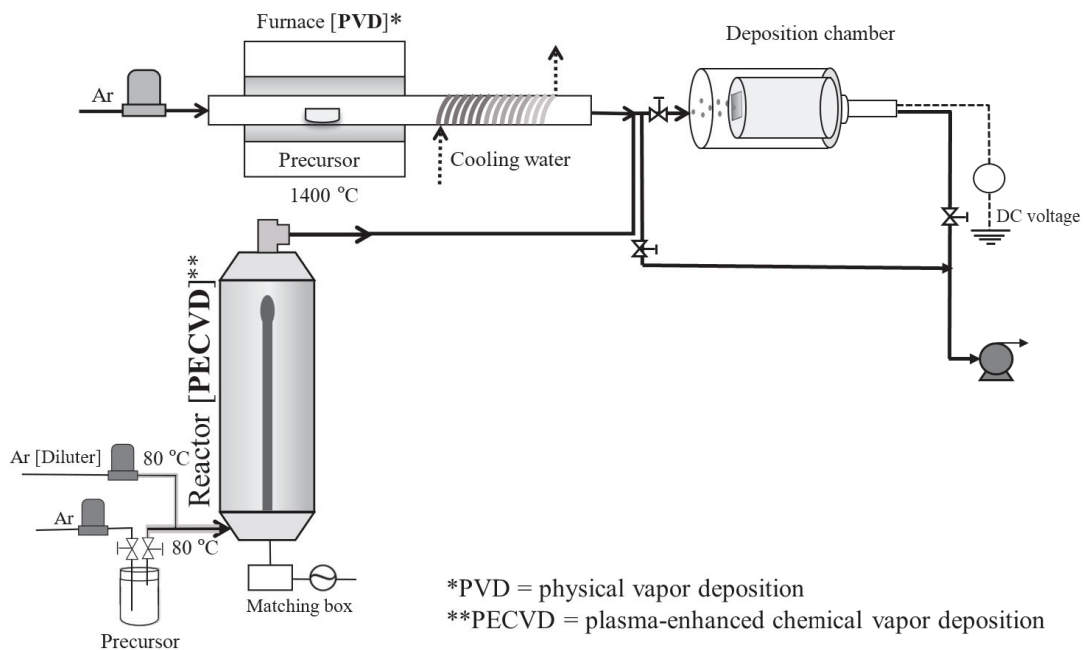


Figure 16. Schematic of PECVD-PVD experimental setup.

2.3. Characterization of TiO₂ and TiO₂-CuO

Surface morphology of the nanoparticulate thin films was inspected using scanning electron microscopy (SEM; S-5200, Hitachi High Technologies). Transmission electron microscopy with energy dispersive X-ray spectroscopy (TEM-EDS; JEM-2010, JEOL) was employed to observe nanoparticle morphology and elemental composition. X-ray diffraction (XRD; MiniFlex 600, Rigaku) determined crystallinity using Cu K α (λ = 0.154 nm) radiation, with an accelerating voltage of 40 kV and a current of 15 mA. Chemical states were analyzed via X-ray photoelectron spectroscopy (XPS; ESCA-3400, Shimadzu). UV–vis diffuse reflectance spectroscopy (UV-Vis DRS, V-650, Jasco) measured the reflectance, and zeta potential measurements were conducted using ZEN3690 (Malvern Instruments Ltd., Malvern).

2.4. Evaluation of photocatalytic activity

To evaluate the activity of both TiO₂ and TiO₂-Cu_xO nanoparticulate thin films, rhodamine 6G (R6G) was utilized as a model pollutant. The photocatalyst was immersed in a cuvette containing 3 mL of R6G aqueous solution at 5 ppm concentration. Experiments were conducted under either UV irradiation (λ = 365 nm; AS ONE) and visible light irradiation (100 mW cm⁻², λ > 385 nm; HAL-C100, Asahi Spectra). Samples were subjected to dark conditions for 30 min at 25 °C before monitoring dye photodegradation at 30 min intervals over 3 h. Changes in absorbance of R6G at 530 nm were measured using a UV–vis spectrophotometer. Additionally, diluted H₂O₂ (Kanto Chemical Co., Inc.) was added to some samples, resulting in a final concentration of 22.3 mM. Photocatalytic activity was tested under acidic (pH 3) and basic (pH 13) conditions with the addition of HNO₃ (Nacalai Tesque, Inc.) and NaOH

(Fujifilm Wako Pure Chemical Corporation), respectively.

Additionally, in **Section 2.5.2** the photocatalytic activity of the fabricated film under UV irradiation was compared with that of commercially available TiO₂ nanoparticles (P25, Sigma–Aldrich, Burlington, MA, USA) immobilized through the doctor-blade method. Both the fabricated film and immobilized P25 weighed 0.08 mg ($\pm 5\%$) each, covering an area of $1 \times 1 \text{ cm}^2$, corresponding to the size of the Si substrate.

2.5. Results and discussions

2.5.1. Photocatalytic Activity of Cu_xO-loaded Anatase- or Rutile- TiO₂

In this section the Cu_xO was formed in the PVD system by heating the Cu metal at 1350 °C and a carrier gas of 700 sccm. **Figure 17** displays SEM images depicting the top views of TiO₂ films annealed at different temperatures under air atmosphere, maintaining a constant heating rate of 5 °C/min until reaching the set temperature. The annealing process was sustained at the specified temperatures for a duration of 3 h. Examination of these SEM images indicates the formation of a highly porous film with minimal agglomeration. This porous and low-agglomeration film holds significance for photocatalytic uses due to its heightened surface-to-volume ratio. This feature enhances photodegradation efficacy by providing a larger active surface area for dye adsorption on the nanoparticle surface.

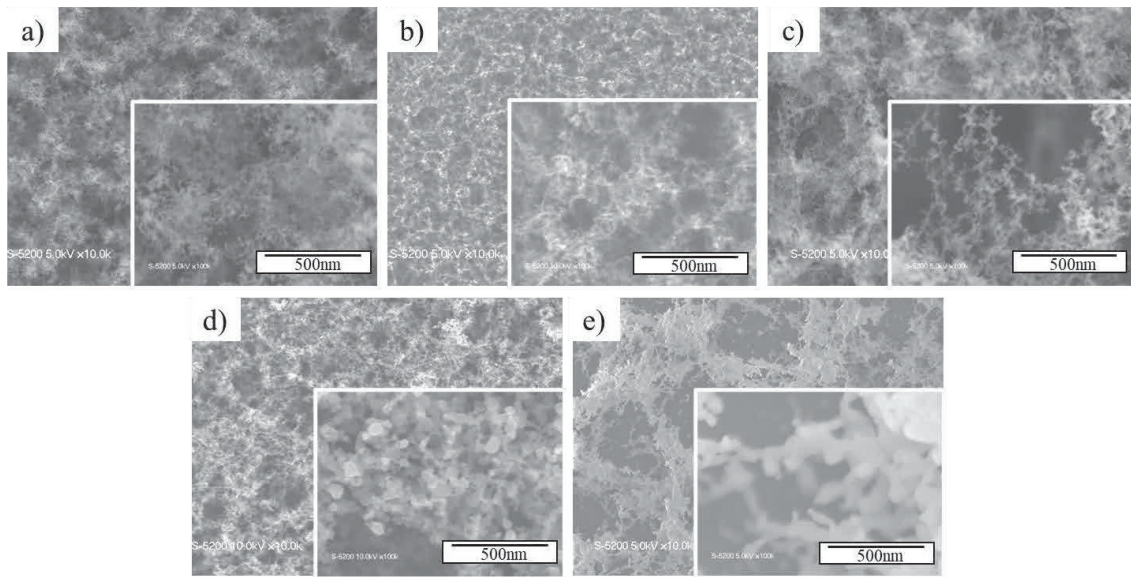


Figure 17. SEM images of TiO₂ annealed at a) 400 °C, b) 500 °C, c) 600 °C, d) 700 °C, and e) 800 °C.

Additionally, from the SEM images an increase in particle size with rising annealing temperature can be viewed, such as observed in our previous studies [11,62]. This growth in particle size after annealing is likely due to increased particle mobility, driven by the coalescence of particles induced by thermal treatment. As temperatures rise, the kinetic energy and diffusion rate of particles increase, facilitating the merging of smaller particles into larger ones.

Figure 18a displays a sequence of XRD patterns for the fabricated nanocomposite films obtained at various annealing temperatures ranging from 400 to 800 °C, with a heating rate of 5 °C/min, including the as-deposited nanocomposite film. Initially, no diffraction peaks are observed in the XRD pattern of the as-deposited film, indicating its amorphous nature. Upon annealing at 400 °C, the film peak corresponding to the anatase phase of TiO₂ emerges, signaling the initiation of the phase transformation from

amorphous to anatase. Subsequently, at 600 °C, a mixture of anatase and rutile phases is observed, with the rutile phase becoming predominant at higher temperatures. Finally, at temperatures of 800 °C, the anatase phase completely transforms into rutile.

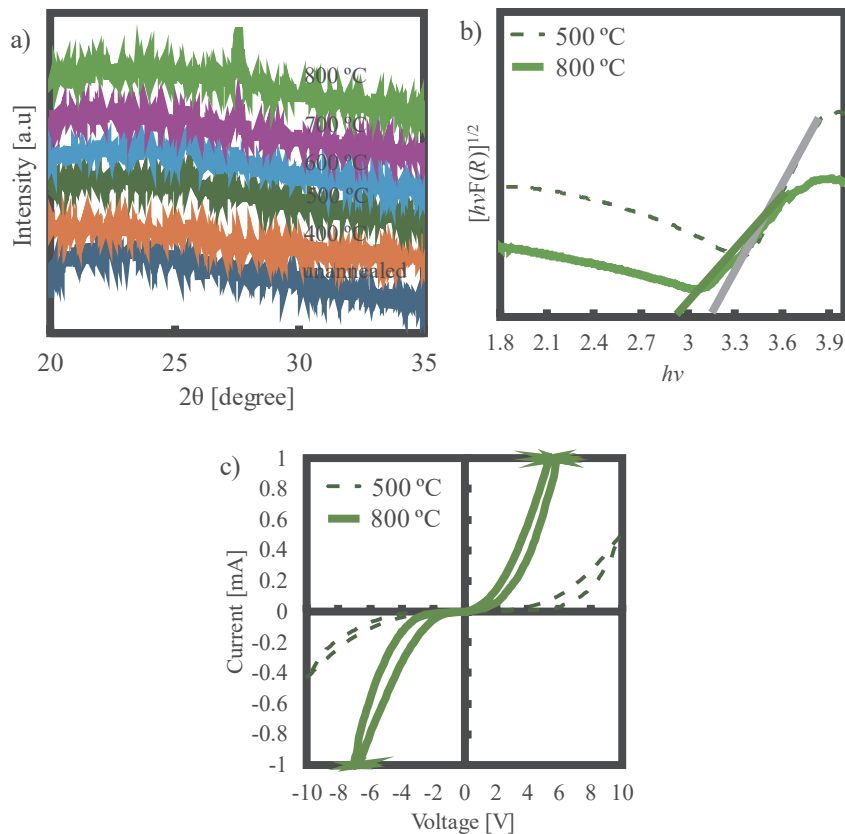


Figure 18. a) XRD pattern, b) band gap, and c) I-V curve of TiO₂ annealed at different temperatures.

Figure 18b and **c** depict the Tauc plot and dark I-V curve of anatase- or rutile-TiO₂, respectively. Tauc plot can determine the band gap energy via the Kubelka–Munk equation, expressed as $F(R) = (1 - R)^2/2R$, where R represents reflectance [19]. The bandgap energy was determined from the intercept of the $(\hbar\nu F(R))^{1/2}$ versus $\hbar\nu$ plot, where h denotes Planck's constant (1240 eV) and ν denotes frequency (eV). It's noteworthy that the bandgap energy of TiO₂ 800 °C (rutile) is lower than that of 500 °C

(anatase). The Tauc plot for TiO₂ annealed at 500 °C and 800 °C revealed a band-gap value of 3.2 and 2.9 eV, comparable to the band gaps of TiO₂ in both its anatase (3.2 eV) and rutile (3.0 eV) forms [73].

The I-V curve indicates the electrical behavior under dark conditions. This curve provides insights into its current output changes in response to varying applied voltages. The results showed that rutile has higher electrical conductivity and charge carrier mobility compared to anatase, leading to higher current values in the I-V curve. This difference in electrical properties can influence the photocatalytic activity and overall behavior of the material in various applications.

The morphology and crystallinity of TiO₂-Cu_xO nanoparticulate thin film of either anatase- and rutile- TiO₂ are shown in **Figure 19**. There were no significant changes in the morphology and crystallinity of TiO₂ (**Figure 17**) and TiO₂-Cu_xO. Such as for samples of pristine TiO₂ nanoparticles with the increase of annealing temperature the size of the nanoparticles increases. In addition, from the TEM images it can be clearly observed that the morphology of the nanoparticles are round-shaped interlinking with one another.

XRD patterns were obtained in the 2θ range of 20–60° for both TiO₂ and TiO₂-Cu_xO nanoparticulate films. After annealing at the set temperatures, the TiO₂ can be observed to crystallize. Upon annealing at 500 °C, the XRD pattern showed peaks at 25.4°, 38.3°, and 48.5°, corresponding to the (101), (004), and (200) planes of the anatase phase of TiO₂, respectively (JCPDS no. 21-1272). Furthermore, as the annealing temperature is increased to 800 °C, peaks at 27.5°, 36.1°, 41.7°, 54.3° and 57.1°, corresponding to the (110), (101), (111), (211), and (220) planes of the rutile phase of TiO₂ can be seen (JCPDS no. 21-1276). However, for both the XRD pattern of the two

annealing temperatures no peaks from Cu_xO can be seen, which can be attributed to the small size and low amount of Cu_xO nanoparticles in the $\text{TiO}_2\text{-Cu}_x\text{O}$.

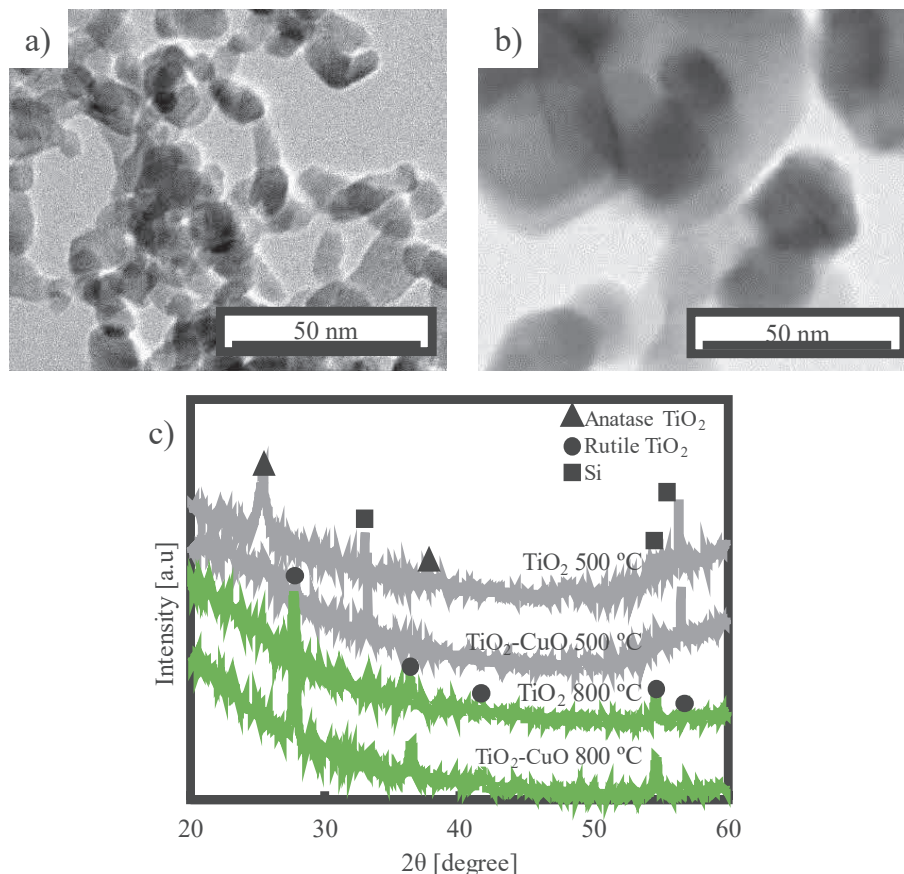


Figure 19. TEM images of $\text{TiO}_2\text{-Cu}_x\text{O}$ nanoparticles annealed at a) 500 °C and b) 800 °C; and c) XRD patterns of TiO_2 and $\text{TiO}_2\text{-Cu}_x\text{O}$ annealed at 500 °C and 800 °C.

XPS analysis was conducted to determine the composition and chemical states of the anatase- or rutile- TiO_2 and $\text{TiO}_2\text{-Cu}_x\text{O}$ nanoparticulate thin films. XPS spectra in **Figure 20** confirmed the presence of Ti and O atom. In these spectra, the prominent peaks observed around 458 eV and 464 eV for both anatase- and rutile- TiO_2 correspond to the $\text{Ti } 2p_{3/2}$ and $\text{Ti } 2p_{1/2}$ states, respectively, and binding energy (BE) separation of 6 eV is typical for TiO_2 [74]. The O 1s XPS spectra reveal peaks at approximately 530 eV, consistent with the lattice oxygen BE of TiO_2 . Additionally, an extra peak observed at a

BE of 532 eV in both samples is attributed to H₂O absorbed on the surface [74]. The difference between the anatase- or rutile- samples can be seen from the O 1s peaks. The rutile- samples had a greater amount of H₂O absorbed on the surface of the nanoparticles, evidenced by the higher peak observed at 532 eV compared to 530 eV. To confirm the existence of Cu_xO, the Cu 2p was measured for the rutile- TiO₂-Cu_xO nanoparticulate thin film. It revealed the presence of Cu_xO, albeit with a weak peak due to the low amount. To enhance detection, an increase in the concentration during deposition is necessary.

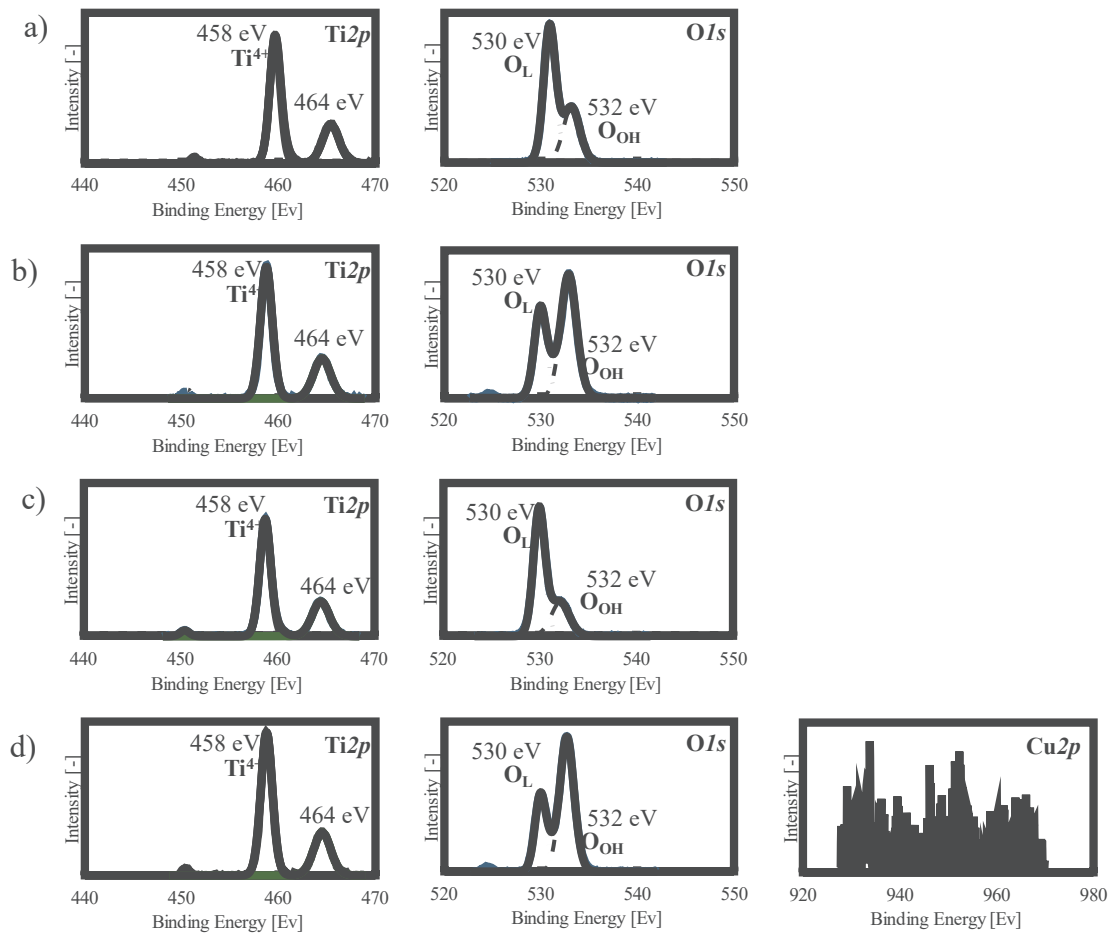


Figure 20. XPS spectra of a,c) anatase- b,d) rutile- TiO₂ and TiO₂-Cu_xO, respectively.

The solid and dotted lines represent the XPS and deconvoluted spectra, respectively.

The photocatalytic activity (**Figure 21**) of both TiO₂ and TiO₂-Cu_xO films were assessed by monitoring the degradation of R6G solution under visible light irradiation. It was determined by deriving the k from the slope of the logarithmic plot of C_t/C_0 against t . Where C_0 , C_t , t , and k represent the initial concentration, concentration at a given time, time (h), and the reaction rate constant, respectively.

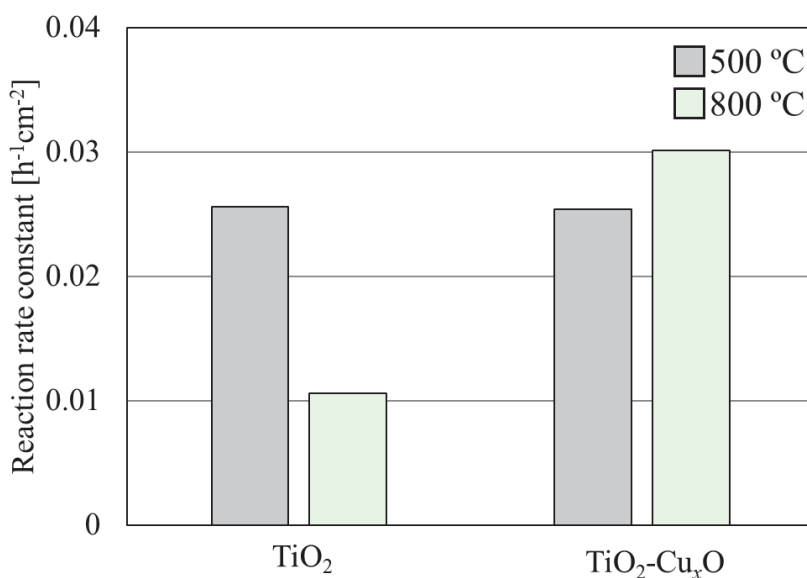


Figure 21. Reaction rate constants for photocatalytic activity under visible light irradiation of anatase- or rutile- TiO₂ as well as their TiO₂-Cu_xO counterparts.

The photocatalytic activity of anatase- TiO₂ was found to be higher compared to that of rutile- TiO₂. In this study, despite its lower band gap and higher conductivity results, rutile exhibited lower activity compared to anatase- TiO₂ for the degradation of R6G under visible light. This difference can be attributed to the inherent characteristics of rutile, characterized by a more compact crystal structure compared to anatase, resulting in a higher density of defects and surface states. These defects provide additional pathways for charge carriers to recombine. Moreover, anatase typically

possesses a higher surface area with more active sites for photocatalytic reactions. In contrast, rutile possesses a lower surface area, as observed in the SEM results, resulting in fewer available sites for charge separation and, consequently, higher chances of recombination.

For $\text{TiO}_2\text{-Cu}_x\text{O}$ showed a different result in the performance where the photocatalytic activity of Cu_xO -loaded rutile- TiO_2 is higher compared to that of anatase- TiO_2 . Chen et. al., [69] has reported the possible charge separation mechanism for the oxidation process of NH_3 under visible light irradiation. On the interface of Cu_xO and anatase- TiO_2 , visible light can only induce excitation within Cu_xO and not anatase- TiO_2 . The resulting holes in Cu_xO have low oxidation potential and thus cannot oxidize NH_3 due to the high VB position of Cu_xO . Conversely, on the interface between Cu_xO and rutile- TiO_2 , electrons from rutile TiO_2 are directly transferred from the VB to the Cu_xO under visible light irradiation. Because of the low VB position of TiO_2 , the resulting holes possess high oxidation potential, enabling efficient oxidation of NH_3 . The proposed mechanism can also justify the increase photocatalytic activity of the rutile- compared to anatase- $\text{TiO}_2\text{-Cu}_x\text{O}$ in this study and as illustrated in **Figure 22**. Owing to the low band gap energy of rutile- TiO_2 it is possible for the electrons to be excited under visible light irradiation and be transferred to Cu_xO . Compared to anatase- TiO_2 with the band gap energy of 3.2 eV, which is more active in the UV light irradiation. The higher number of holes formed in rutile- TiO_2 compared to anatase- TiO_2 can increase the formation of $\bullet\text{OH}$ that can degrade the R6G for the rutile- $\text{TiO}_2/\text{Cu}_x\text{O}$ sample under visible light irradiation.

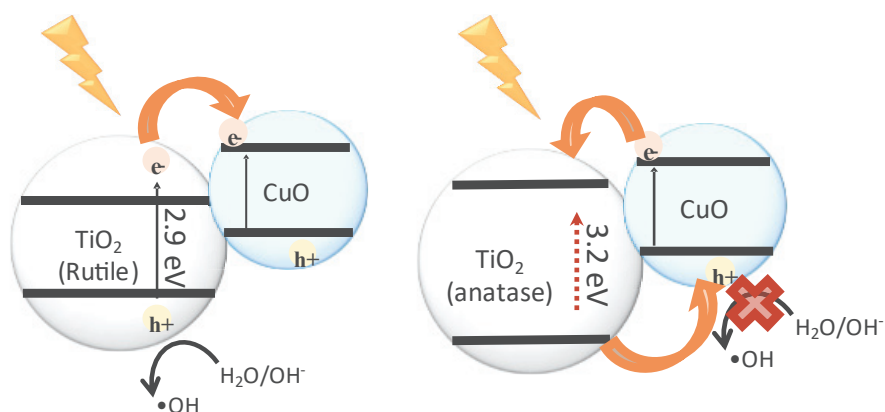


Figure 22. Schematic of charge separation of anatase- and rutile- $\text{TiO}_2\text{-Cu}_x\text{O}$ under visible light irradiation.

2.5.2. Photocatalytic activity optimization of CuO -loaded anatase- TiO_2 through H_2O_2 addition and pH adjustments

In this section, further investigations into the properties of anatase- TiO_2 and $\text{TiO}_2\text{-Cu}_x\text{O}$ and its photocatalytic activity will be explained. To enhance the quantity of Cu_xO , the Cu_xO nanoparticles were generated through heating of Cu metal at $1400\text{ }^\circ\text{C}$ with a carrier gas flow of 900 sccm. Notably, the Cu_xO sample in this section were measured as deposited (not annealed). Additionally, to optimize the photocatalytic activity, H_2O_2 was added into the system for the R6G photodegradation. Furthermore, various parameters such as alterations in UV or visible light exposure and pH levels were examined during the testing process.

Similar to **Section 2.5.1**, the SEM image of TiO_2 in **Figure 23a** the surface morphology of the annealed thin film, comprising of nanoparticles. TEM analysis provided further insight into the morphology (**Figure 23a–e**). The TiO_2 and Cu_xO nanoparticles appeared spherical, with sizes ranging from 7 to 15 nm and 8 to 14 nm, respectively. The introduction of Cu_xO did not alter the morphology of the TiO_2

nanoparticles, as observed and compared in both the TiO_2 and $\text{TiO}_2\text{-Cu}_x\text{O}$ in **Figure 23a**, **b**, and **e**. Closer examination of the $\text{TiO}_2\text{-Cu}_x\text{O}$ samples revealed the deposition of Cu_xO nanoparticles on the TiO_2 nanoparticle surface, confirming the presence of Cu_xO in the film. EDS analysis (**Figure 23f**) further supported this finding, showing peaks corresponding to Cu $L\alpha$, Cu $K\alpha$, Cu $K\beta$, Ti $K\alpha$, Ti $K\beta$, and O $K\alpha$, confirming the presence of Cu_xO and TiO_2 .

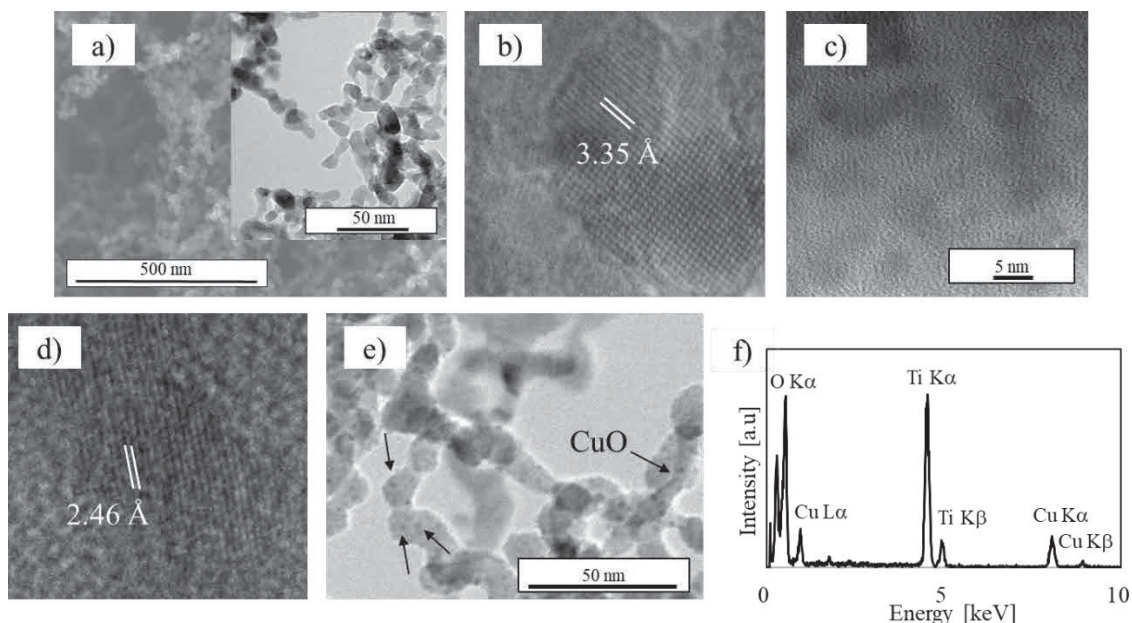


Figure 23. Morphology of nanoparticles. (a) SEM images of TiO_2 (inset: TEM). HR-TEM of (b) TiO_2 and (c,d) Cu_xO . Additionally, (e) TEM image and (f) EDS spectrum highlight $\text{TiO}_2\text{-Cu}_x\text{O}$.

The high-resolution TEM analysis in **Figure 23b** and **d** confirm the crystallization of TiO_2 post-annealing and as-deposited Cu_xO , with measured interplanar spacings of 3.35 Å and 2.46 Å, respectively. This crystallization is further supported by XRD analysis (**Figure 24**). For TiO_2 , the anatase crystalline phase exhibited notably higher photocatalytic activity compared to the rutile phase. The XRD pattern confirmed the

crystalline nature of TiO₂ nanoparticles post-annealing, with a peak corresponding to anatase TiO₂ observed at approximately $2\theta = 25^\circ$ (JCPDS no. 21-1272). Regarding Cu_xO nanoparticles, the visible peak corresponded to Cu₂O at $2\theta = 37.16^\circ$ (JCPDS no. 5-0667), indicating their crystalline state upon deposition onto the substrate, even before annealing. However, in the TiO₂-Cu_xO nanocomposite sample, only anatase TiO₂ peaks were observed, with no visible peaks corresponding to Cu₂O or CuO. Additionally, there was no shift in the peaks with the addition of Cu_xO to TiO₂. The absence of Cu_xO peaks could be due to the relatively low concentration and dispersion of Cu_xO loaded. In addition, the crystallite size of the nanoparticles could be estimated from Scherrer's equation $D = k\lambda/(B\cos\theta)$, where k , λ , B , and θ denote the constant value ($k = 0.9$), wavelength of the X-ray source ($\lambda = 0.154$ nm), full-width at half-maximum of the XRD peak, and peak angle, respectively [75]. Crystallite sizes of 13.0 nm for TiO₂ and 14.9 nm for TiO₂-Cu_xO were estimated using this equation, which align reasonably well with sizes obtained directly from TEM images.

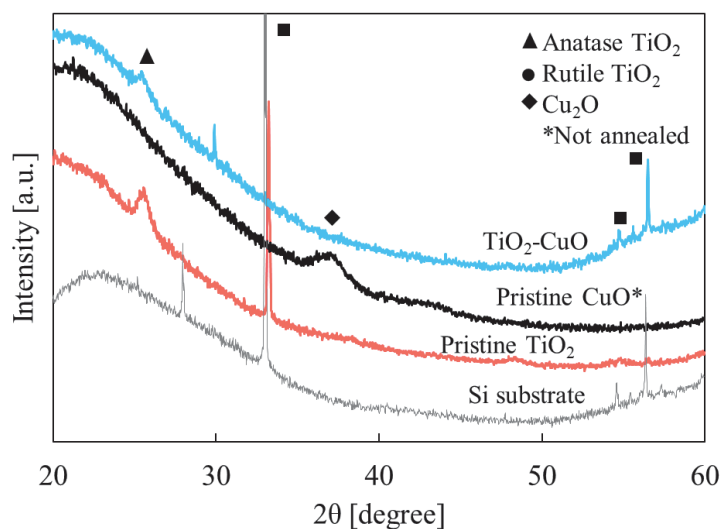


Figure 24. XRD pattern indicating crystallinity of TiO₂, Cu_xO, and TiO₂-Cu_xO nanoparticulate thin films.

XPS analysis was employed to confirm the chemical composition of the nanoparticulate thin film, particularly to confirm the presence of Cu_xO and its impact on the chemical state of TiO₂ nanoparticles. The Ti 2p, O 1s, and Cu 2p core level spectra were examined to determine the chemical composition and valence state on the film's surface (**Figure 25a–c**). In the Ti 2p profile for TiO₂, the BE for the Ti 2p^{3/2} and Ti 2p^{1/2} peaks were measured at 458.65 eV and 464.65 eV, respectively, corresponding to Ti⁴⁺ of TiO₂ [74]. Similarly, in the Ti 2p profile for TiO₂-Cu_xO, BEs of 458.33 eV and 464.33 eV were observed for Ti 2p^{3/2} and Ti 2p^{1/2}, respectively.

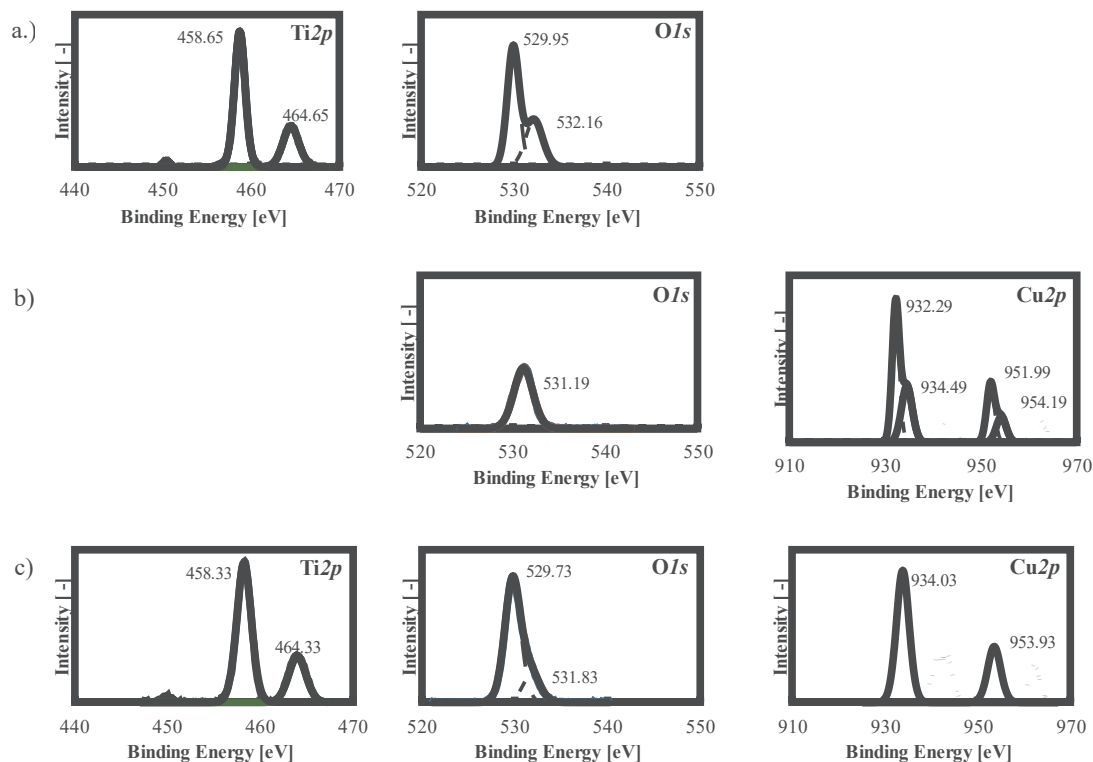


Figure 25. Chemical state of a) TiO_2 , b) Cu_xO , and c) $\text{TiO}_2\text{-CuO}$. The solid and dotted lines represent the XPS and deconvoluted spectra, respectively.

The O 1s XPS spectra reveal peaks at 529.96 eV and 532.16 eV for the electron BE of O 1s in TiO_2 (O_L) and H_2O absorbed on the surface (O_{OH}), respectively. Cu_xO exhibited a higher BE (531.19 eV) for O_L in the O 1s spectrum, attributed to the variation in Cu- or Ti- bonding to -O. In $\text{TiO}_2\text{-Cu}_x\text{O}$, the BEs for O 1s were 529.73 eV and 531.83 eV, indicating a slight shift compared with that observed for TiO_2 , attributed to the interaction between Cu ions and TiO_2 [76].

For the as-deposited Cu_xO , Cu $2p_{3/2}$ and Cu $2p_{1/2}$ peaks were detected at 932.29 eV and 951.99 eV, respectively, corresponding to Cu^+ and Cu^{2+} , respectively. However, for the annealed $\text{TiO}_2\text{-Cu}_x\text{O}$ film, the presented peaks were solely ascribed to Cu^{2+} at Cu $2p_{3/2}$ and Cu $2p_{1/2}$, with BEs of 934.03 eV and 953.93 eV, respectively. The satellite

peaks at approximately 940 eV and 960 eV in both Cu 2p results corresponded to the existence of Cu²⁺. These results indicate complete oxidation of Cu after annealing in air, hence the term "TiO₂-CuO" is used to refer to this nanocomposite. **Table 5** shows the concentration of the elements extracted from the XPS peaks in **Figure 25**. The mass concentration of Cu is 5.54 %.

Table 5. XPS-analysis mass concentration of elements

Peak	Mass Conc.
C 1s	12.23 %
Ti 2p	35.91 %
O 1s	46.33 %
Cu 2p	5.54 %

Figure 26a shows the Tauc Plot of the film derived from UV-vis diffuse reflectance spectroscopy measurements using the Kubelka-Munk function. The bandgap energies of the pristine Cu_xO, pristine TiO₂, and TiO₂-CuO nanoparticulate thin films were found to be 1.6, 3.26, and 3.25 eV, respectively. Notably, the bandgap energy of TiO₂-CuO was slightly lower than that of pristine TiO₂, despite the small amount of CuO added to the film. Udayabhanu, et al., [23] has reported the decrease of the band gap energy with the increase concentration of CuO loaded TiO₂, with concentrations of 1–4 mol % with the resulting band gap energy of 3.05–2.73 eV. This decrease in bandgap energy is attributed to the charge transfer of the p–n heterojunction between TiO₂ and CuO, consistent with previous reports [77]. This finding aligns with the XPS results, where the reduction in the BE with the addition of CuO to TiO₂ indicates a decrease in the bandgap energy.

Figure 26b illustrates the zeta potentials of the samples. It indicates that both the TiO₂ and TiO₂-CuO samples exhibited positively charged surfaces under acidic conditions and negatively charged surfaces under basic conditions. Zero zeta potential was observed at pH ~6.5 for pristine TiO₂ and TiO₂-CuO, suggesting that the surface charge remained relatively unchanged after CuO addition to TiO₂. A negatively charged surface is advantageous for interactions with cationic dyes such as R6G, enhancing the affinity of the nanoparticle surface of the film to the dye and thereby increasing photocatalytic degradation, as reported previously [67,78].

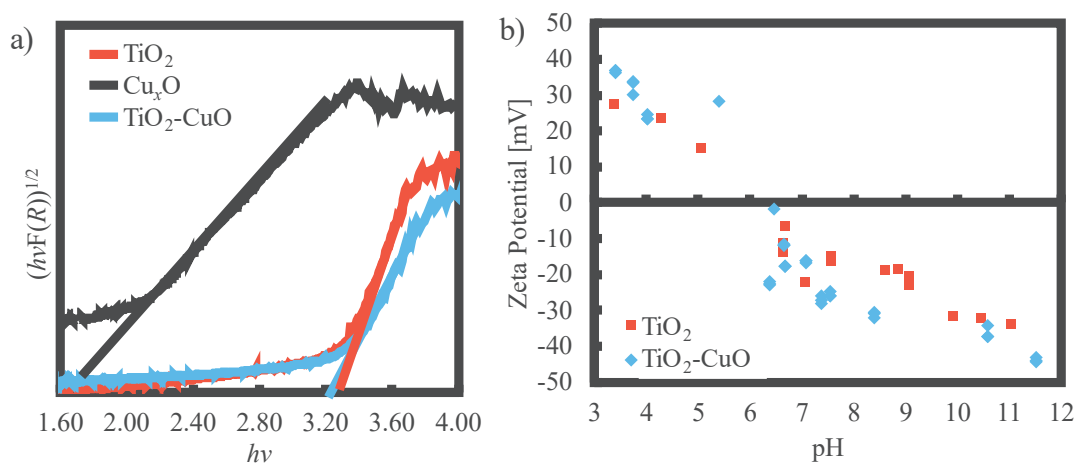


Figure 26. a) Plot of $(hvF(R))^{1/2}$ versus $h\nu$ of nanoparticulate thin film and b) zeta potential.

The degradation process of R6G was first assessed under UV irradiation. It was evaluated by monitoring the change of the absorbance peak of the dye using a UV-vis spectrophotometer. The normalized dye concentration was plotted over time (**Figure 27**). Direct photolysis (depicted as Blank) or dye degradation without a catalyst exhibited limited photodegradation of R6G, with C_t/C_0 being less than 0.99 within 180 min of irradiation. Addition a TiO₂ nanoparticulate film into the photodegradation system

enhanced the dye photodegradation rather than photolysis, resulting in $C_t/C_0 = 0.73$ after 180 min of irradiation. However, the photocatalytic activity decreased when employing the $\text{TiO}_2\text{-CuO}$ nanoparticulate thin film ($C_t/C_0 = 0.96$). CuO was introduced into the system as an electron acceptor to mitigate electron–hole recombination in TiO_2 ; however, the results suggest that CuO presence potentially amplified charge recombination, effectively serving as a center for electron–hole recombination.

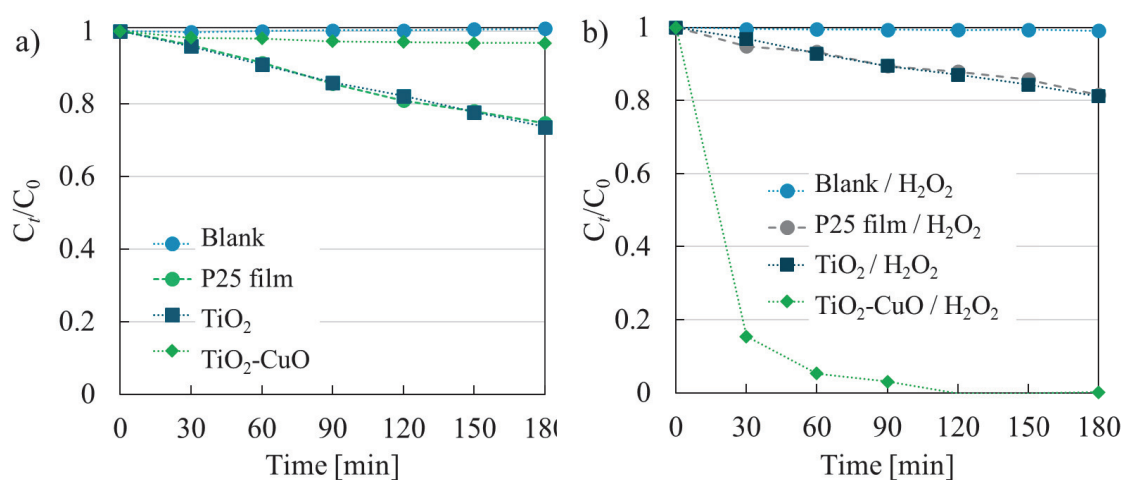


Figure 27. Degradation of R6G by (a) photolysis, TiO_2 , $\text{TiO}_2\text{-CuO}$, and P25 films; and (b) the corresponding samples with added H_2O_2 under UV light irradiation.

To further enhance the dye photodegradation, H_2O_2 (~ 0.05 mL; 22.3 mM) was introduced into the photodegradation system as an electron acceptor. The addition of H_2O_2 did not significantly increase either the photolysis (Blank/ H_2O_2) or photocatalytic ($\text{TiO}_2/\text{H}_2\text{O}_2$) degradation of R6G, with C_t/C_0 values of 0.99 and 0.81, respectively (**Figure 27b**).

Compared to the other films, the photocatalytic degradation by the $\text{TiO}_2\text{-CuO}$ nanoparticulate thin film was significantly enhanced with the addition of H_2O_2 , resulting in complete degradation of R6G at 180 min. The possible degradation

mechanism is illustrated in **Figure 7** for TiO₂-CuO/H₂O₂. Briefly, by the formation of the Type II p-n heterojunction by introducing CuO into TiO₂. The electrons generated by light irradiation was excited from the VB of CuO to CB of TiO₂. In addition, a Fenton-like reaction of Cu²⁺ and photo-generated electrons with H₂O₂ effectively increased the production of •OH, thereby enhancing the photocatalytic activity. A comparison of the results in **Figure 27a and b** indicate a substantial improvement in the photocatalytic activity with the addition of H₂O₂ and CuO.

To confirm the Fenton-like reaction of CuO and H₂O₂, degradation of R6G (5 ppm, 39.4 mL) was done under dark condition with commercially available powder CuO nanoparticles (5 mg) with and without the addition of H₂O₂. Such seen in **Figure 28** the degradation of R6G with the addition of H₂O₂ is faster compared to samples of CuO only, which proves the occurrence of the Fenton-like reaction of CuO/H₂O₂.

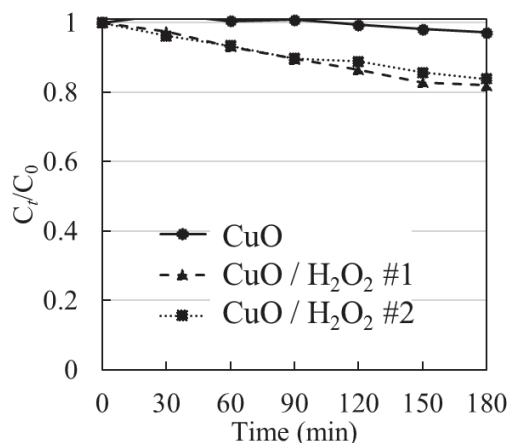


Figure 28. Degradation of R6G by CuO and CuO/H₂O₂ under dark condition.

In addition, to evaluate the effectiveness of the produced TiO₂ nanoparticulate thin film performance, its photocatalytic activity was compared with that of the P25 film. The rates of R6G photodegradation for both the fabricated TiO₂ nanoparticulate thin

film and the P25 film were found to be similar, irrespective of the presence of H₂O₂. This consistency underscores the effectiveness of the photocatalytic activity of the film developed in this study.

In photocatalytic applications, TiO₂ typically exhibits limited activity for applications under UV irradiation. Therefore, photocatalytic activity test was also conducted in the visible light region to evaluate the produced film. Additionally, considering the varying pH levels of wastewater effluents, the pH of the photodegradation system was adjusted to lower or higher values of 3 or 13, respectively. The R6G dye typically has a pH of 7. However, to explore the effects of varying pH conditions, acidic conditions (pH 3) and basic conditions (pH 13) were achieved by adding HNO₃ and NaOH, respectively, to the R6G solution. This adjustment allowed for an examination of how different pH levels influence the photocatalytic degradation process.

The calculated reaction rate constant results are shown in **Figure 29a**. Additionally, **Figure 29b–d** depict the relationship between $\ln(C_t/C_0)$ and t for the calculation of k , demonstrating the photocatalytic activity within 180 min (3 h) of light irradiation. These findings highlight the significant enhancement in R6G degradation achieved through the utilization of the photocatalyst and the addition of H₂O₂. TiO₂-CuO/H₂O₂ exhibited the most substantial degradation of R6G under visible light irradiation across various pH levels, with the highest efficacy observed at pH 13 and a reaction rate constant of 0.99 h⁻¹cm⁻². Comparatively, the photodegradation of R6G by pristine TiO₂/H₂O₂ and TiO₂-CuO/H₂O₂ films outperformed the photolysis of R6G by H₂O₂ alone (Blank/H₂O₂) under visible light irradiation.

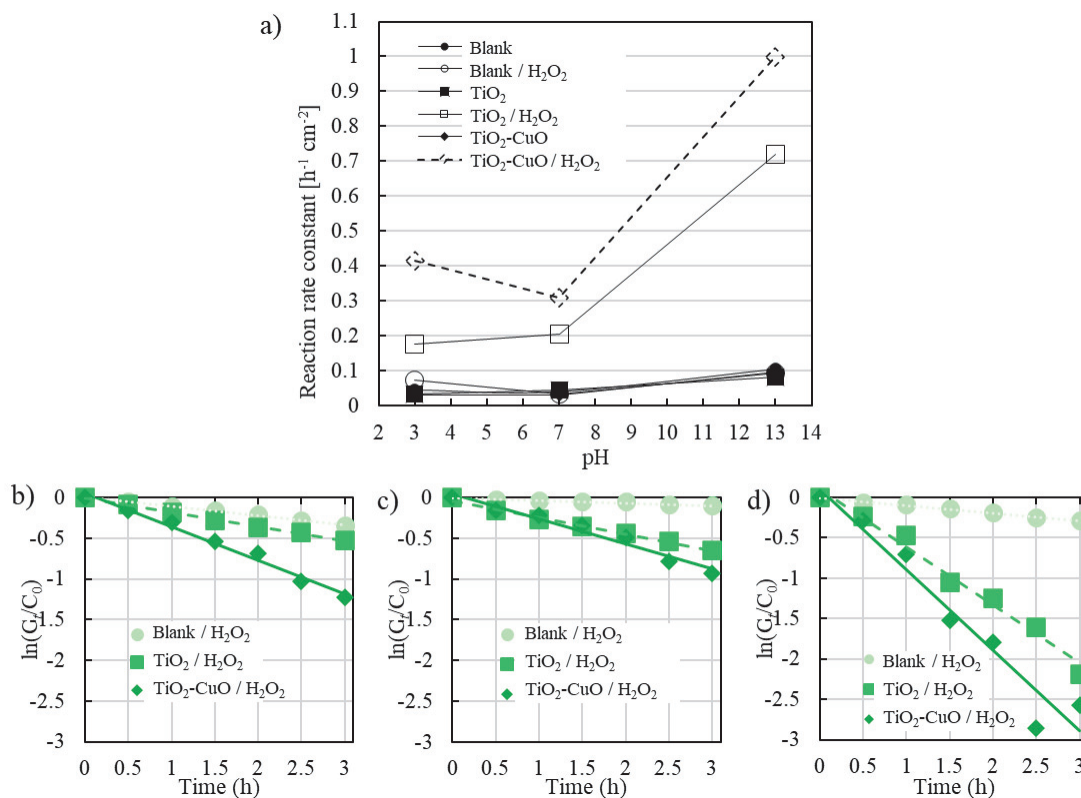


Figure 29. Photodegradation reaction rate constant of R6G under visible light irradiation for different pH conditions; representative curves of $\ln(C_t/C_0)$ versus time for samples at pH values of (b) 3, (c) 7, and (d) 13.

Comparing the photolysis results (Blank/H₂O₂), it becomes evident that the activity increased in the order of pH 3 > 13 > 7. At lower pH levels, where HNO₃ was introduced into the photodegradation system, the photolysis of R6G intensified. According to a previous study [79], the heightened activity under either acidic or basic conditions is governed by distinct mechanisms, leading to enhanced degradation under both conditions. However, in the absence of the photocatalyst, photodegradation by H₂O₂ under various pH conditions remained relatively insignificant, contrasting with the notable degradation observed upon the addition of the photocatalyst. This underscores the importance of dye degradation through the photocatalytic mechanism.

The photocatalytic activity of $\text{TiO}_2/\text{H}_2\text{O}_2$ followed the order of $\text{pH } 13 > 7 > 3$, consistent with the zeta potential results. Under basic conditions, the fabricated film exhibited a negatively charged surface, enhancing its potential for R6G adsorption compared to acidic conditions, where the surface carried a positive charge. This observation shows the influence of surface conditions on the photodegradation of R6G, indicating a strong dependence on the surface properties of the photocatalyst.

$\text{TiO}_2\text{-CuO}/\text{H}_2\text{O}_2$ demonstrated superior photocatalytic activity across all pH values compared to both photolysis with the addition of H_2O_2 and the photocatalytic activity of $\text{TiO}_2/\text{H}_2\text{O}_2$. This enhancement can be attributed to the Fenton-like reaction facilitated by the presence of CuO. Upon closer examination, it was observed that the photocatalytic activity followed the order of $\text{pH } 13 > 3 > 7$. Particularly noteworthy was the substantial improvement in photodegradation at pH 13 when $\text{TiO}_2\text{-CuO}$ was employed instead of pristine TiO_2 . The heightened activity of $\text{TiO}_2\text{-CuO}$ at pH 13 compared to other pH values may be attributed to the enhanced adsorption of R6G on TiO_2 . Additionally, the increased activity at pH 3 can be attributed to the synergistic effects of $\text{TiO}_2\text{-CuO}$ interaction and the Fenton-like reaction between CuO and H_2O_2 . Furthermore, the presence of H^+ ions at pH 3 contributes to an increased production of $\bullet\text{OH}$, which further aid in the degradation of R6G.

2.6. Conclusions

TiO_2 and TiO_2 nanoparticulate thin films were fabricated via a one-step PECVD-PVD method. The size of TiO_2 nanoparticles increased with higher annealing temperatures. XRD analysis indicated the transformation of TiO_2 from anatase to rutile phase through the increase annealing temperature. Complete oxidation of CuO occurred

after annealing. The band gap energy and zeta potential of TiO₂-CuO showed only slight changes compared to pristine TiO₂. Rutile TiO₂ loaded with CuO exhibited superior photocatalytic activity under visible light irradiation compared to anatase TiO₂ loaded with CuO. Further investigation for the photocatalytic activity by the change of pH and addition of H₂O₂, the highest photocatalytic activity was achieved for TiO₂-CuO/H₂O₂ at pH 13 with a reaction rate constant of 0.99 h⁻¹cm⁻², followed by the photodegradation of R6G by TiO₂/H₂O₂ at pH 13.

Chapter 3

Investigation of TiO₂ and TiO₂-Ag Photocatalyst Fabricated by the Gas-phase Method

Abstract

In this chapter, Ag was introduced into TiO₂ nanoparticulate thin films via a one-step plasma-enhanced chemical vapor deposition and physical vapor deposition method. Owing to the localized surface plasmon resonance (LSPR) of Ag the light absorbance can be widened to the visible light region. LSPR absorbance peaks confirmed the presence of Ag nanoparticles. The photocatalytic activity was done for rhodamine 6G degradation under visible light irradiation, with an optimal Ag content of 0.24 wt. % exhibiting superior activity compared to TiO₂ nanoparticulate thin film and commercially available TiO₂ nanoparticles immobilized on Si substrates.

Additionally, the effect of heating rates for the annealing process was studied. TiO₂-Ag were subjected to varying heating rates (3 to 60 °C/min). The fabricated films exhibited changes in characteristics such as nanoparticle size, crystalline size, crystallite phase, and surface area. Photocatalytic activity evaluation by methylene blue degradation under UV light irradiation revealed a gradual enhancement with increasing heating rates, attributed to the increase surface area and total pore volume.

3.1. Introduction

Apart from the fabrication of semiconductor-loaded TiO₂ by the addition of CuO explored in **Chapter 2**, metal-loaded TiO₂ has also attracted attention. In our previous study [60] a one-step gas-phase method combining PECVD-PVD was utilized to fabricate metal-loaded TiO₂ by the addition Ag nanoparticulate thin films. This approach produced pure Ag nanoparticles with a size of less than 10 nm, embedded within the porous structure of the accumulated TiO₂ nanoparticles forming film. Ag nanoparticles were observed on the surface of TiO₂ nanoparticles. These films exhibited excellent photocatalytic activity under UV light irradiation. There remain further exploration opportunities, which will be delved into in **Chapter 3**. Additionally, this investigation will extend the potential of TiO₂ as a semiconductor- based photocatalyst.

Increasing the light-absorption capacity of TiO₂ nanoparticles is pivotal for enhancing their photocatalytic activity in everyday applications, owing to the LSPR of Ag metal nanoparticles. LSPR activation enhances the visible-light-driven photocatalytic activity by broadening light absorption to longer wavelengths, increasing light scattering, and promoting electron transfer from the metal to the semiconductor [14]. Previous studies [43,80] have demonstrated that Ag nanoparticles, when added to TiO₂, significantly enhance visible light absorption and improve photodegradation capabilities for organic pollutants both under UV or visible light irradiation.

Previously the effect of annealing temperature on the characteristics and photocatalytic activity under UV light irradiation of TiO₂-Ag nanoparticulate thin film has been studied in our laboratory [62]. A further careful examination of post-deposition parameters, such as the heating rate, presents an intriguing opportunity to further modify the characteristics of the material. The heating rate during annealing has been

identified as one of the critical parameters influencing grain growth, crystal size, and orientation, with the potential to optimize the application of the material. Research by Dikici et. al., [81] on TiO₂ powders demonstrated that increasing the heating rate led to a higher degree of anatase phase shift due to lattice strain, without altering morphology or size distribution. Interestingly, the highest photocatalytic activity was observed for a specific heating rate that gave high crystallinity. Limited attention has been given to the influence of different heating rates in the annealing process for TiO₂-Ag nanocomposites, presenting an interesting area for further exploration.

In this chapter **Section 3.4.1** explores the characteristics and visible-light-driven photocatalysis of Ag-loaded TiO₂ nanoparticulate thin film with different Ag contents. Furthermore, the photocatalytic activity was compared with immobilized commercially available TiO₂ nanoparticles, known as P25. Whereas **Section 3.4.2** delves deeper on the to the effect of heating rate on the characteristics of TiO₂-Ag nanoparticulate thin film and its photocatalytic activity.

3.2. Materials and experimental procedures

The precursors employed in the fabrication of TiO₂-Ag nanocomposites were TTIP and Ag granules (> 99% purity, Nilaco Corp.). The fabrication of TiO₂-Ag nanocomposite thin films was achieved via a one-step method involving PECVD-PVD system such as in **Figure 16**. The TiO₂ nanoparticles are generated as in **Section 2.2**. To fabricate TiO₂-Ag nanoparticulate thin films, Ag nanoparticles were generated by evaporating Ag granules in a tubular furnace (TMF-300N, AS ONE) at temperatures ranging from 1020–1220 °C to regulate the Ag contents. The resulting Ag vapor swiftly condensed via a cooling water system, forming Ag nanoparticles. Subsequently, Ag and

TiO₂ nanoparticles from the PVD and PECVD systems were simultaneously deposited onto a Si substrate with a +500 V applied. The pressure of the system was maintained at 1.2 kPa. The nanoparticulate thin films produced underwent annealing at 500 °C for 3 h in N₂ atmosphere to ensure the crystallization of TiO₂ and to ensure that Ag metal was not oxidized. Furthermore, commercially available TiO₂ nanoparticles (P25) were immobilized via a doctor blade method to form a film. The weight of the films was set to 0.06 mg (\pm 5%). These samples were subjected to photocatalytic activity test for 5 ppm of R6G under visible light irradiation.

As a continuation from the previous study [62] of the effect of annealing temperature, the fabrication process follows the same parameters. The TiO₂ and Ag nanoparticles were continuously deposited onto a Si substrate under an applied voltage of +300 V to form a film. To achieve a target weight of 0.35 mg (\pm 5%). The total pressure of the system was maintained between 2–4 kPa using a vacuum pump. Following fabrication, the resulting film underwent annealing under air atmosphere for 12 h. The effect of heating rate was investigated by varying it from 3–60 °C/min, while the annealing temperature was held constant at 600 °C. The photocatalytic activity test was conducted for the degradation of 2 ppm MB under UV light irradiation.

3.3. Characterization of TiO₂ and TiO₂-Ag

The morphologies, sizes, and crystalline phases of the films were analyzed using various methods in the following sections. SEM (S-5200, Hitachi High Technologies) was utilized to observe the surface morphologies and film thicknesses. XRD (MiniFlex 600, Rigaku) was employed to observe the crystallinity and phases of the nanoparticulate thin films. Detailed morphology and crystallinity were examined by

TEM and HR-TEM (JEM-2010, JEOL). Additionally, XPS (ESCA-3400, Shimadzu) was performed to understand the chemical state of Ag nanoparticles. The light absorbance of the films was evaluated by measuring their light-absorption capability using a UV–Vis spectrophotometer (V-650, Jasco) equipped with an integrated sphere. Elemental analysis to confirm and quantify the Ag content in the TiO₂-Ag nanoparticulate thin films was conducted using ICP-OES (SPS 3000; Hitachi High Technologies). Additionally, nitrogen adsorption–desorption experiments were performed to analyze the surface area and pore volume using Autosorb-1 (Quantachrome Instruments).

3.4. Results and discussions

3.4.1. Visible-light photocatalytic activity of TiO₂ and TiO₂-Ag

SEM images depicted in **Figure 30** showcase the morphology of TiO₂ and TiO₂-Ag nanoparticulate thin films, as well as P25 film. Although SEM analysis did not directly reveal the presence of Ag nanoparticles, a subtle increase in nanoparticle size was observed upon Ag addition to TiO₂ nanoparticles. Specifically, the TiO₂ nanoparticulate thin film exhibited an average size of 40.97 nm for TiO₂ nanoparticles, while the TiO₂-Ag nanocomposite films with 0.56 wt. % and 2.97 wt. % Ag contents displayed sizes of 43.65 nm and 53.81 nm, respectively, for TiO₂ nanoparticles. Post-annealing SEM images suggested that the inclusion of Ag promoted the coalescence of TiO₂ nanoparticles, leading to larger particle sizes in TiO₂-Ag samples compared to pristine TiO₂ nanoparticles [60]. Overall, annealing played a role in influencing the morphology of the film, where factors like annealing temperature, duration, and the presence of foreign materials could impact nanoparticle size. In this investigation, the addition of

Ag was found to increase the size of TiO₂ nanoparticles. The P25 film was observed to be denser compared to the fabricated TiO₂ and TiO₂-Ag nanoparticulate thin film.

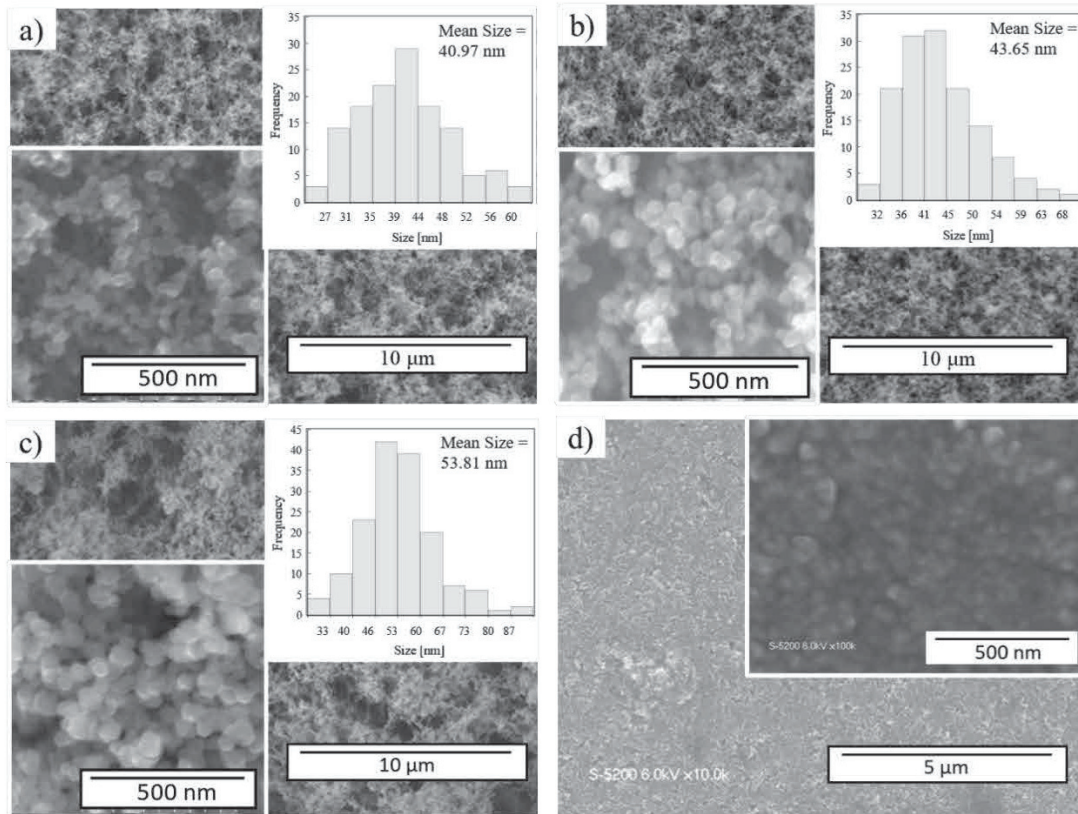


Figure 30. SEM images of a) TiO₂ and TiO₂-Ag with b) 0.56 c) 2.97 wt. % Ag content and d) P25 film. Corresponding size distributions (insets a-c).

The XRD patterns presented in **Figure 31** provide insights into the crystallinity and phase composition of the nanoparticulate thin films. Annealing plays a critical role in achieving well-crystallized TiO₂ nanoparticles. The observed peaks at $2\theta = 25.5^\circ$, 38.3° , and 48.5° correspond to the (101), (004), and (200) planes of crystallized TiO₂ in the anatase phase, respectively. Anatase TiO₂ phase was consistently observed across all samples. Additionally, broad peaks in the XRD patterns were noted due to the small size and quantity of nanoparticles within the films. Notably, a minor diffraction peak at $2\theta =$

44.5°, corresponding to rutile TiO₂, was detected with the addition of Ag (0.24 wt. %). This finding aligns with previous research [49] indicating a phase transition from anatase to rutile TiO₂ occurring at lower annealing temperatures with Ag addition. The anatase-to-rutile phase transformation typically ranges from 400 °C to 1200 °C which depends on the fabrication method used [82]. Our study observed this transition at 500 °C with the one-step PECVD-PVD fabrication method and loading of Ag metal nanoparticles. The presence of both anatase and rutile phases in TiO₂ is beneficial for enhancing photocatalytic activity due to their synergistic effects on electron-hole separation. However, the existence of Ag metal nanoparticles was not evident from the XRD peaks, possibly due to their low quantity and dispersion within the nanoparticulate films [16]. Additionally, the appearance of the Si peak at 33° was attributed to the Si substrate.

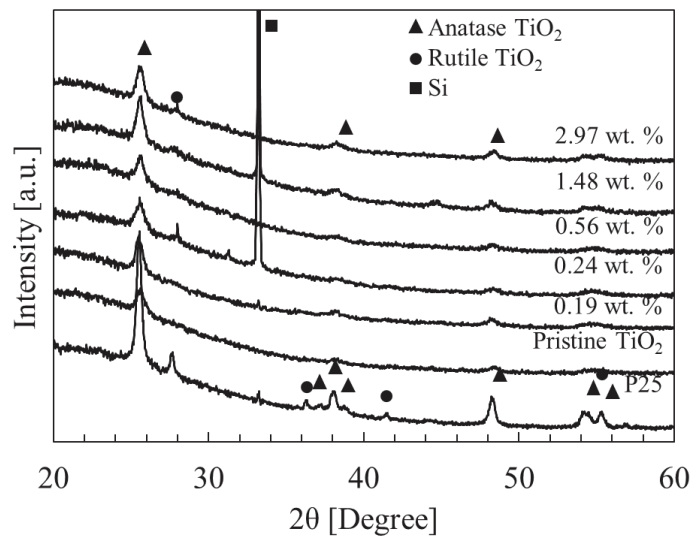


Figure 31. XRD pattern of TiO₂ and TiO₂-Ag fabricated by PECVD and PVD; P25 film prepared by spin coating.

XPS analysis was employed to verify the oxidation state of the pristine Ag

nanoparticles both before and after annealing under N₂ atmosphere at 500 °C for 3 h. The results depicted in **Figure 32a and b** revealed peaks at 367.2 eV and 374.2 eV with a spin energy separation of 6.0 eV, indicating the presence of zero-valent or metallic Ag (Ag⁰) [43]. Remarkably, no shift in the XPS peaks was observed post-annealing, affirming the ability of Ag to withstand oxidation processes and maintain its metallic state during annealing under N₂ atmosphere. Furthermore, the stability of Ag metal was evaluated over an extended period, as shown in **Figure 32c and d**. The peak of Ag remained unchanged, confirming its long-term stability. The stability of the metallic form of Ag is important, as the LSPR effect of the metal Ag can enhance the photocatalytic activity of TiO₂ under visible light irradiation.

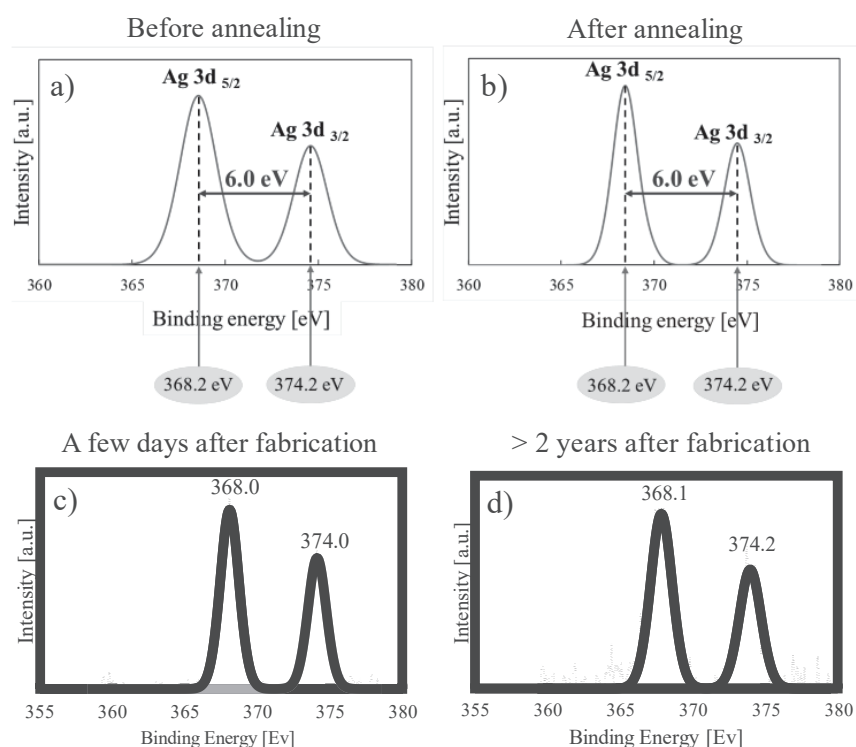


Figure 32. Ag 3d XPS spectra of Ag a) before and b) after annealing in N₂ and annealed TiO₂-Ag c,d) after a certain period of time.

The impact of varying Ag contents on TiO₂ and its comparison with TiO₂ nanoparticulate thin film and the P25 film were assessed based on their absorbance (Figure 33). TiO₂ nanoparticles exhibited notable light absorption within the wavelength range of 300–400 nm across all samples. However, their absorbance at longer wavelengths, corresponding to visible light, was relatively low, indicating limited photoactivity in this region. Incorporating Ag metal nanoparticles led to increased light absorption at longer wavelengths ($\lambda > 500$ nm), enhancing the light-harvesting capacity. This observation aligns with findings by Fei, et. al., [83], demonstrating that the addition of Ag enhances visible light absorption in TiO₂. The presence of Ag metal and its LSPR progressively enhanced visible light absorption with increasing Ag content, as evident in our results. The LSPR peak of 450 nm for Ag metal can be seen to become more prominent at higher Ag content of such 3.02 wt. %.

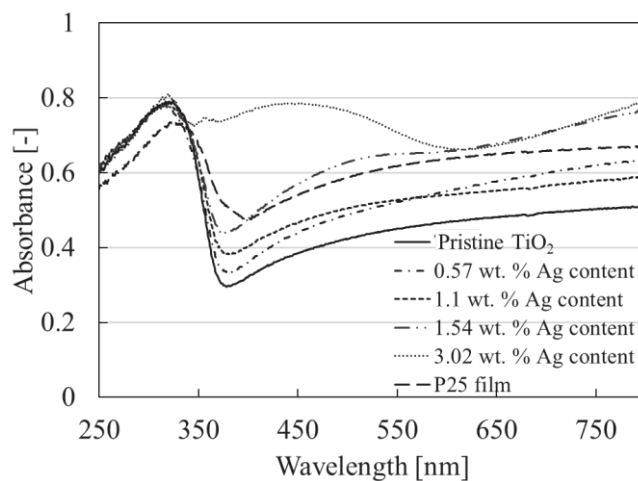


Figure 33. Absorbance spectra of TiO₂ and TiO₂-Ag fabricated by PECVD and PVD; P25 film prepared by spin coating.

The photocatalytic degradation of R6G under visible light irradiation was investigated using fabricated films weighing at 0.06 mg and a substrate size of 1×1 cm².

The experiment comprised photolysis of R6G, photocatalytic activity with TiO₂ and TiO₂-Ag films with varying Ag contents, and P25 film. Additionally, an adsorption test of the dye and film in the dark was conducted. The activity was assessed by monitoring changes in R6G color and its absorbance peaks. The percent degradation was calculated from the change of peak absorbance of R6G throughout the photocatalytic activity test by $(A_0 - A_t)/A_0 \times 100\%$. Where A_0 corresponds to the initial absorbance, while A_t is the absorbance after a certain interval (t), respectively. Furthermore, the reaction rate constant was determined by deriving the k from the slope of the logarithmic plot of C_t/C_0 against t . Where C_0 , C_t , t , and k represent the initial concentration, concentration at a given time, time (h), and the reaction rate constant, respectively.

Figure 34 reveals that the presence of a photocatalyst significantly increased the percent degradation and reaction rate constant of R6G degradation compared to photolysis and adsorption tests. The P25 film exhibited higher photocatalytic activity than the TiO₂ nanoparticulate thin film due to its phase mixture of anatase and rutile, which enhances electron-hole separation. The addition of Ag to TiO₂ increased its photocatalytic activity under visible light, with the optimum Ag content observed at 0.24 wt. %. From the observed characteristics, the increase photocatalytic activity other than solely because of the addition of Ag, was due to the formation anatase and rutile phases and the increase of light absorption capabilities. The lower activity of P25 compared to TiO₂-Ag can be attributed to several inherent characteristics of P25. These include its low surface area, nonporous nature, and limited activity in the visible light region [84].

An increase in Ag content beyond this optimum concentration resulted in decreased photocatalytic activity. The decrease in activity could be attributed to factors such as the

increasing size of TiO₂ nanoparticles such as seen in SEM. Additionally, several studies [85,86] have elucidated the enhanced electron-hole recombination in Ag when excessive amount is added. The experimental results of this study contribute to understanding the increased activity of TiO₂ by the addition of Ag, which demonstrated a twofold increase compared to TiO₂.

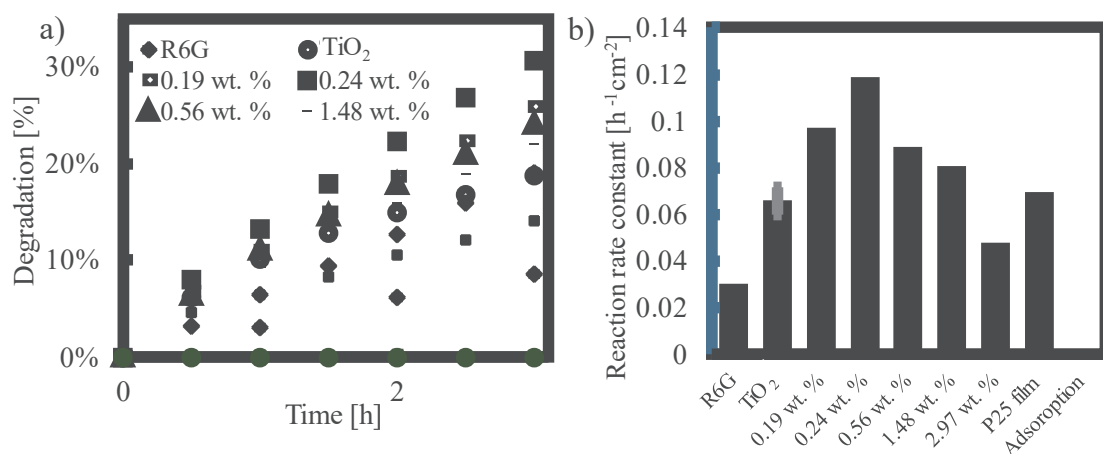


Figure 34. c) Percent degradation of R6G and d) its corresponding reaction rate constants for TiO₂, and TiO₂-Ag, and P25 film.

3.4.2. The effect of heating rate on the characteristics and photocatalytic activity of TiO₂-Ag

In our previous study [62], we examined the impact of annealing temperature on the morphology of TiO₂-Ag, revealing larger and thinner nanoparticles with increasing annealing temperatures. In addition, such seen in the results of **Figure 17** and **Figure 18** and our other previous study [11] for TiO₂ nanoparticles. Variations in annealing temperature also yielded notable differences in crystallite size, phase content, and other characteristics stated. Consequently, the change in the photocatalytic efficiency of the nanocomposite films. In this section we further investigate the post-deposition

annealing parameters, such as the annealing heating rates and its effects towards TiO₂-Ag characteristics such as the morphology, thickness, crystallinity, and surface area. The subsequent findings in this section can increase the understanding of the annealing parameters which can be applied to other materials such as TiO₂-Cu_xO in **Chapter 2**.

SEM images in **Figure 35** still showed the porous non-agglomerated film consisted of nanoparticles such as in previous sections. From measurement of the nanoparticles size, negligible differences were noted in the mean diameter values of nanoparticles after annealing at different rates. The mean diameter was measured to be 22, 25, 24, 20, and 22 nm for heating rates of 3, 5, 10, 30, and 60 °C/min, respectively. This suggests that the heating rate change from 3–60 °C/min insignificantly affects the particle size of nanocomposite films.

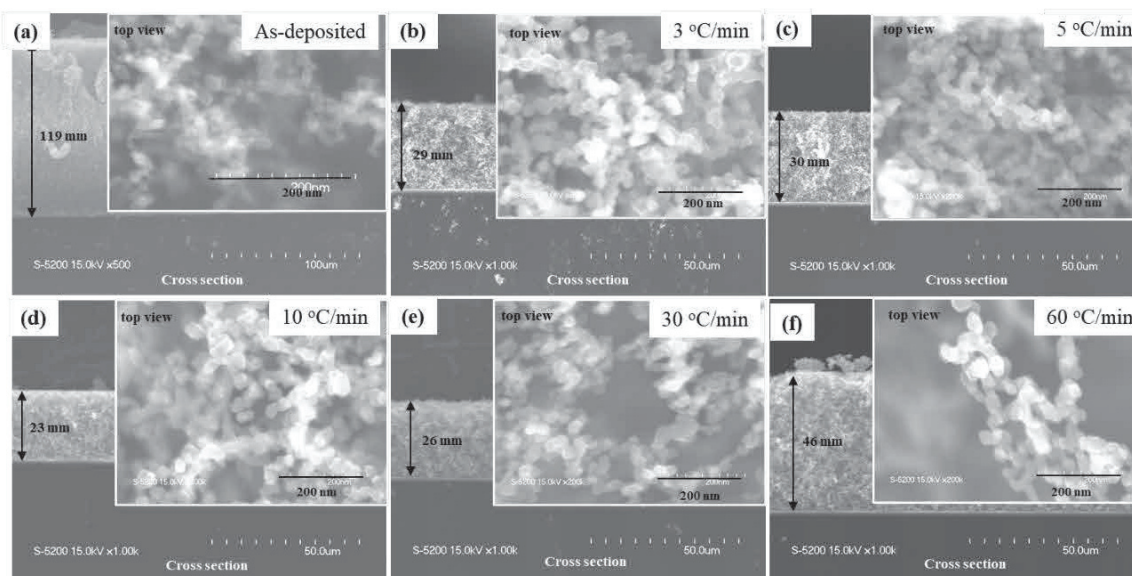


Figure 35. SEM images showing the cross-sectional view of TiO₂-Ag: a) the as-deposited and annealed with b) 3 °C/min, c) 5 °C/min, d) 10 °C/min, e) 30 °C/min, and f) 60 °C/min heating rates. The inset provides a top-view perspective.

Furthermore, the relative thickness showed no significant difference observed for

heating rates of 3–30 °C/min. The relative thickness gradually rose at a heating rate of 60 °C/min, despite insignificant changes in the size of nanoparticles. A high heating rate might result in a brief calcination process, leaving insufficient time for all nanoparticles within the primary framework to coalesce, thereby yielding a thicker film structure compared to lower heating rates.

Annealing does not only improve crystallinity and densifies the film, but carbon contaminants are also removed. Higher heating rates (60 °C/min) result in greater thickness compared to lower rates, possibly due to the reduced time required for coalescence. To further assess the effects of annealing heating rates on carbon contaminants, XPS measurements on pristine TiO₂ samples was done (**Figure 36**). The results showed that a higher heating rate leads to nearly the same amount of secondary carbon peaks as the as-deposited sample (**Table 6**). Conversely, a lower heating rate of 5 °C/min, which involves a longer duration (120 min compared to 10 min at 60 °C/min), results in a lower ratio of secondary peaks due to higher carbon residue. This can also explain the higher thickness observed at higher heating rates, as the remnant carbons contribute. The thickness for these pristine TiO₂ samples were also confirmed and it was found that the samples annealed at a heating rate of 60 °C/min was thicker than the 5 °C/min. Further studies on the annealing time and atmosphere (nitrogen or air) are necessary to understand their impact on the characteristics of TiO₂ and TiO₂-Ag.

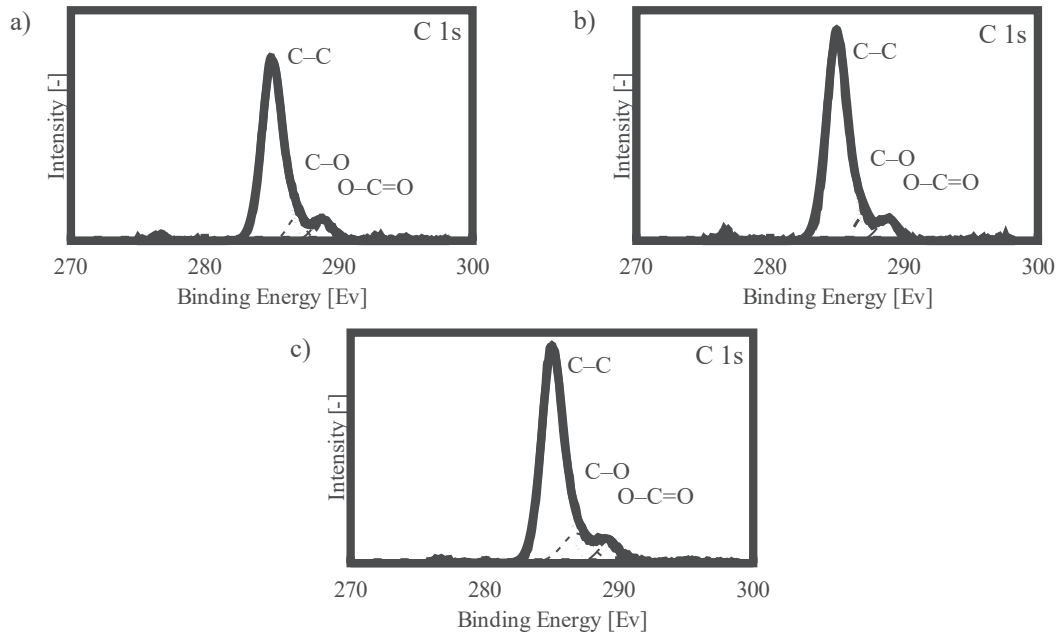


Figure 36. XPS spectra of C 1s peaks of TiO₂ annealed at heating rates of a) 60 °C/min, b) 5 °C/min, and as deposited.

Table 6. C 1s peak ratios of TiO₂ annealed in air with different heating rates

Element	Heating rate	Primary Peak Ratio	Secondary Peak Ratio
		$\frac{I_{C-C}}{I_{C-C} + I_{C-O} + I_{O-C=O}}$	$\frac{I_{C-O} + I_{O-C=O}}{I_{C-C} + I_{C-O} + I_{O-C=O}}$
C 1s	60 °C/min	0.800785	0.199215
	5 °C/min	0.817761	0.182239
	As deposited	0.806708	0.193292

The average crystallite size estimated using the lattice planes from **Figure 37a** and the Scherrer's equation, $D = k\lambda/(B\cos\theta)$, where k , λ , B , and θ denote the constant value, wavelength of the X-ray source, full-width at half-maximum of the XRD peak, and peak angle, respectively. The calculation revealed no significant difference of the crystallite size of anatase (range from 26 to 29 nm) across all heating rates. Conversely, the crystallite size of rutile (31–45 nm) was consistently greater than that of anatase.

Furthermore, the crystallite size of rutile decreased from 41 nm at 3 °C/min to 32 nm at 60 °C/min, except at 5 °C/min. Furthermore, the ratio of anatase to rutile from the peaks were also calculated (**Figure 37b**). It reveals that the film is dominated by the anatase phase (~84%) and rutile phase (~16%).

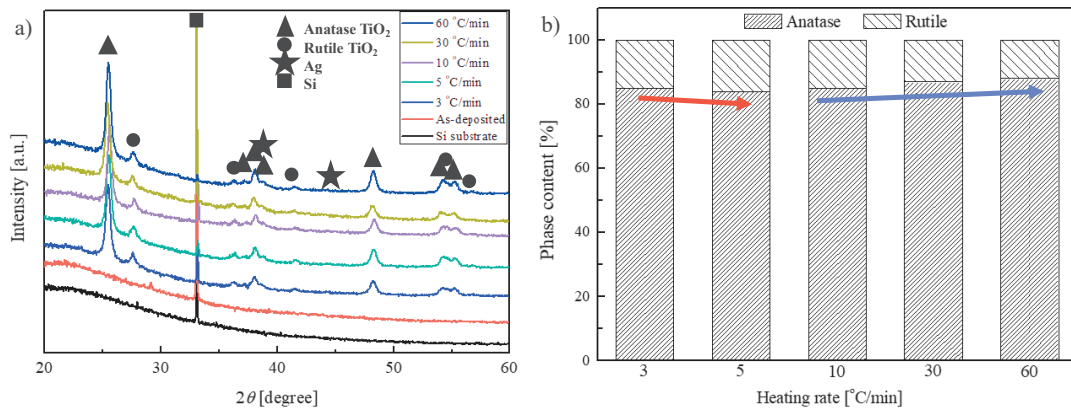


Figure 37. a) XRD pattern of TiO₂-Ag nanoparticulate thin films annealed at different heating rates and b) the ratio of anatase and rutile phases.

Further experiments conducted at two heating rates (3 and 60 °C/min) with a shorter holding time (2 h), which revealed only slight differences in XRD patterns such seen in **Figure 38**. Despite a slightly higher intensity at the higher heating rate, both spectra displayed a small rutile peak, indicating its presence in the nanocomposite after short-term annealing. However, the intensity of these peaks was lower than those observed with longer holding times, suggesting that holding time predominantly influences the crystal phase of the nanocomposite compared to the heating rate.

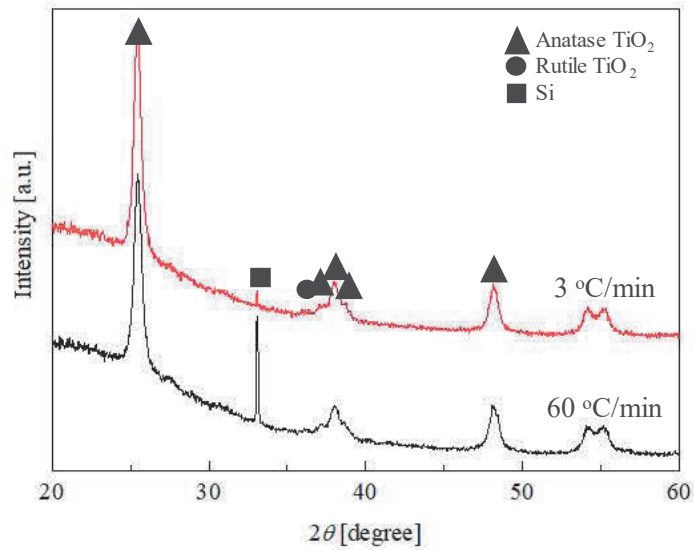


Figure 38. XRD pattern of TiO₂-Ag nanoparticulate thin films at heating rates of 3 and 60 °C/min (2 h holding time).

Further examination of the samples was done by HR-TEM such as seen in **Figure 39**. It reveals that a higher heating rate (60 °C/min) leads to greater crystallinity compared to a lower heating rate (5 °C/min), as indicated by the lattice spacing of the anatase or rutile phase. HR-TEM observation highlighted that at high heating rates, the entire area of the nanocomposite particles is mostly occupied by the crystalline phase structure, with only a small portion exhibiting imperfect crystallization. Conversely, at low heating rates, a significant portion of the phase structure appears imperfectly crystallized. This imperfection is likely due to the lower crystallinity of the anatase phase, making the lattice spacing less clearly observable.

TEM images further revealed that the nanocomposite was primarily determined by the diffraction peak of anatase (101), with a lattice spacing of 0.35 nm (JCPDS no. 21-1272), consistent with results from XRD. Additionally, a lattice spacing of 0.24 nm

corresponds to the Ag (110) phase, indicating the presence of Ag nanoparticles in the nanocomposite structure.

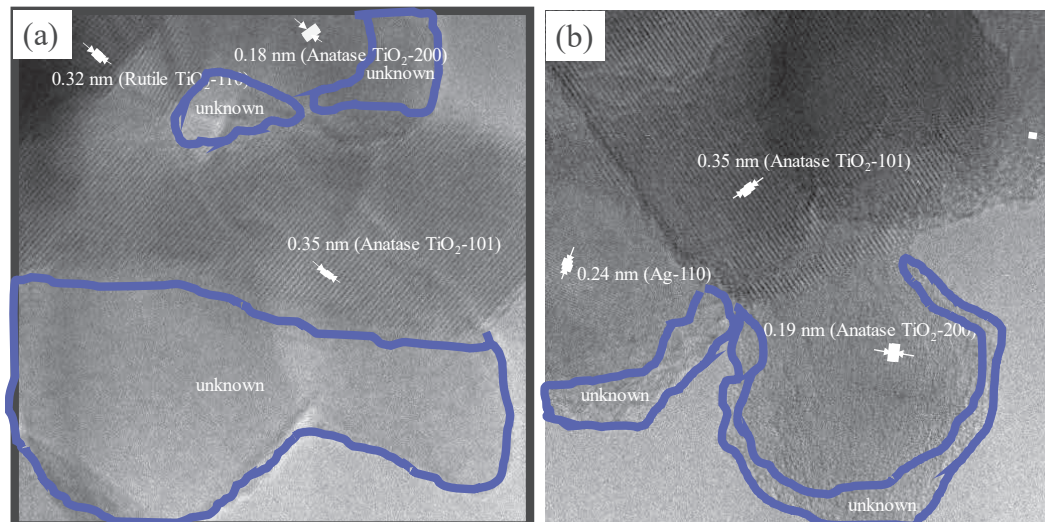


Figure 39. HR-TEM images of TiO₂-Ag nanoparticulate thin films at heating rates of a) 5 and 60 °C/min (12 h holding time).

The surface area and pore volume values obtained from nitrogen adsorption-desorption isotherm analysis presented in **Figure 40** exhibits a clear increase with the rise in the heating rate except for 5 °C/min. A larger pore volume facilitates the penetration of dye molecules into the deeper regions of catalyst particles, creating more reaction sites. This phenomenon ultimately contributes to a higher photocatalytic activity, enabling the degradation of numerous organic compounds.

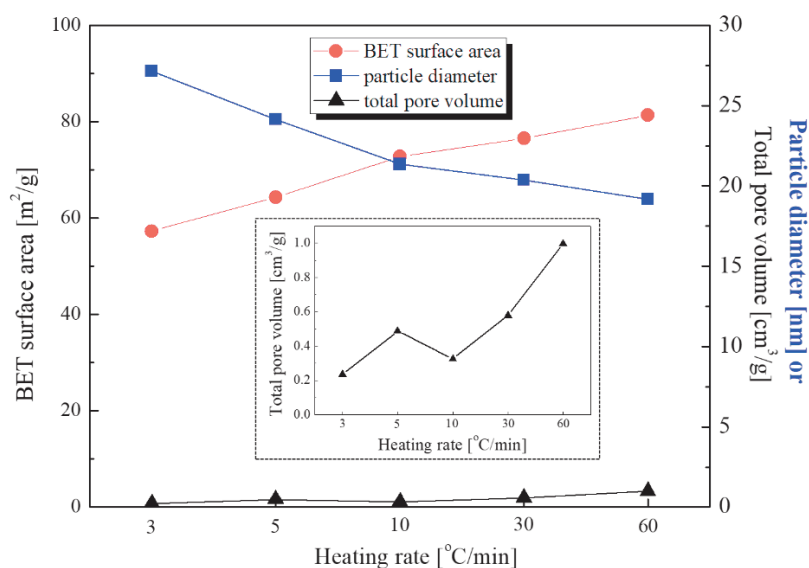


Figure 40. Surface area, total pore volume, and particle diameter of TiO₂-Ag nanoparticulate thin films annealed at 600 °C.

The photocatalytic activity was evaluated through the degradation of MB aqueous solution under UV light irradiation. The absorbance data at 664 nm were converted into concentrations to calculate the MB degradation efficiency. Photocatalytic activity was assessed by determining the rate constant (k) using the equation $\ln(C_0/C_t) = kt$. **Figure 41** depicts $\ln(C_0/C_t)$ plotted against irradiation time at various heating rates. The rate constants were obtained from the slope of the fitted linear curves in $\ln(C_0/C_t)$ versus irradiation time (t), showing a gradual increase with heating rates. The highest rate constant at 60 °C/min indicates rapid MB degradation and excellent photocatalytic activity.

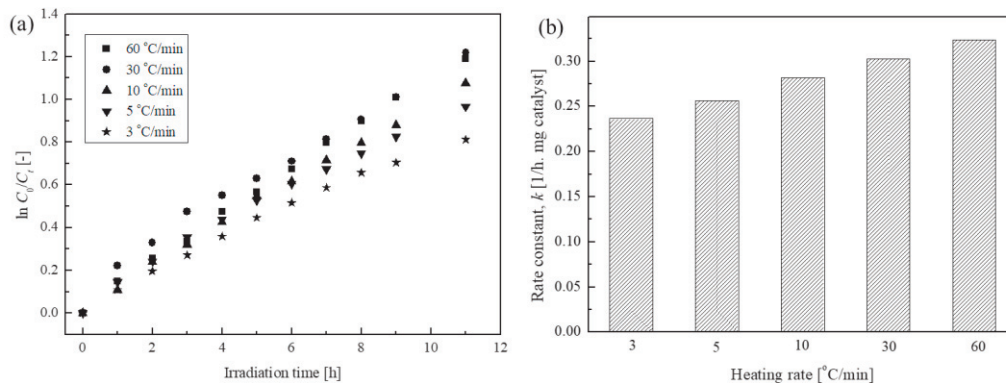


Figure 41. Photocatalytic activity of TiO_2 -Ag nanocomposite films annealed at 600 °C with a different heating rate. a) plots of $\ln C_0/C_t$ vs irradiation time and b) rate constants.

Typically, photocatalytic activity is influenced by several parameters, such as particle size, crystallite size, and phase content. The possibility for enhanced photocatalytic activity at 60 °C/min is the differing thicknesses among the films (**Figure 35**). Allowing for increased contact between catalyst particles and the dye, resulting in the degradation of more organic compounds. The enhanced photocatalytic activity at higher heating rates may also be attributed to the higher crystallinity, as observed through HR-TEM analysis. HR-TEM images (**Figure 39**) at several nanometers revealed that a heating rate of 60 °C/min led to higher crystallinity compared to lower heating rates. In addition, with the slightly higher ratio of anatase to rutile phase in the film at 60 °C/min (**Figure 37b**), which is a much more active crystal structure of TiO_2 .

Dikici, et al., [81] compared the photocatalytic activity of TiO_2 nanoparticles and revealed that the degradation process is optimum at heating rates of 1 °C/min, which is due to the high crystallinity of the anatase phase. However, for them the photocatalytic activity decreases with increase heating rates because of the lower crystallinity with

increase heating rates, in addition to the increase of the residual carbon left. This shows the characteristic of TiO₂ is influenced by the heating rates and therefore effects the effectiveness in photodegradation of organic pollutants under UV light irradiation.

3.5. Conclusions

TiO₂ and TiO₂-Ag nanoparticulate thin films were successfully produced using a one-step PECVD-PVD method. The addition of Ag did not alter the spherical structure of TiO₂; however, it led to an increase in nanoparticle size after annealing. Ag nanoparticles remained stable even after annealing under an N₂ atmosphere. Moreover, the addition and increase in Ag content widened the light absorption capacity of TiO₂ into the visible light spectrum, thereby broadening its potential applications beyond UV light irradiation. Photocatalytic testing with R6G under visible light irradiation revealed an optimal degradation rate of 0.1191 h⁻¹cm⁻² at 0.24 wt. % Ag content.

Furthermore, when the film is annealed at 600 °C with different heating rates (5–60 °C/min), no significant differences in morphology, phase composition, and crystallite size were observed from the SEM and XRD analyses. After annealing, the films exhibited a mixture of anatase-rutile phase, with predominantly anatase phase. TEM analysis showed that higher heating rates led to higher crystallinity. Additionally, the surface area and total pore volume increased with the heating rate. Photocatalytic activity tests for MB degradation under UV light revealed enhancement with increasing heating rate.

Chapter 4

Extending Research on Semiconductor-based Photocatalyst Fabricated by Alternative Gas-phase Method

Abstract

ZnO and ZnO-Ag nanoparticles were fabricated using a one-step spray pyrolysis method. The addition of Ag was done with varying contents of 1, 5, and 10 wt. %. Additionally, alterations in the carrier gas ratio ($O_2:N_2$) of 1:0, 1:2, 1:1, 2:1, and 0:1 were also investigated to assess their impact on nanoparticle characteristics such as crystallinity, morphology, and surface areas. These characteristics were correlated with the photodegradation under UV light irradiation results. The spray pyrolysis method can produce crystallized crumpled-shaped ZnO and ZnO-Ag nanoparticles. The highest surface area was found at Ag content of 10 wt. % with 0:1 carrier gas ratio. Furthermore, ZnO-Ag nanoparticles exhibit better activity compared to ZnO specifically at a carrier gas ratio of 0:1, with reaction rate constants of 0.0059 and 0.0025 min^{-1} for ZnO-Ag and ZnO, respectively.

4.1. Introduction

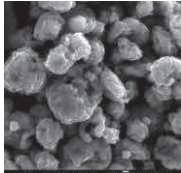
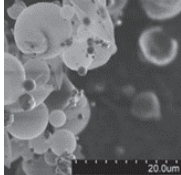
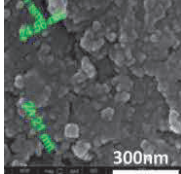
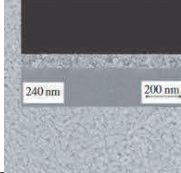
Chapter 2 and **3** have delved into the fabrication of TiO₂-based photocatalysts with the addition of either CuO or Ag by the one-step PECVD-PVD method. As the Ag-loaded TiO₂ materials have already been clearly established in our laboratory we try to investigate the Ag-loaded material with the main ZnO photocatalyst. Such that of TiO₂-based materials, alternative material such as ZnO has also given opportunities in AOPs. ZnO (band gap energy = 3.37 eV) is characterized by its affordability, environmental friendliness, and robust physical and chemical stability [5,87,88]. Moreover, it boasts a high surface area and excellent photosensitivity [39]. However, the rapid recombination of excited electrons–holes attributed to its wide band gap energy considerably limits the efficient utilization of ZnO [39].

As explored in **Chapter 1** the fabrication in the gas-phase method can also be done by using SP method which also gives its own distinct morphology. This method offers a single-step fabrication process, leading to improved dispersion of the resulting nanomaterial, thus enhancing its activity [54]. **Table 7** shows several examples of fabricated materials by SP and their applications. This method is a versatile process in the fabrication of nanomaterials either in the form of powder or film. The SP method involves the generation of droplets by a nebulizer, subsequent solvent evaporation, precursor chemical reaction, and densification of the formed particles [89,90]. This study investigates the fabrication of Ag-loaded ZnO nanoparticles by the one-step SP method and its photocatalytic activity.

Parameters such as the precursor concentration, type of gas, and furnace temperature are known to affect the characteristics of the produced materials. In this chapter the ratio of O₂:N₂ carrier gas used will be investigated. Different carrier gases yield diverse

nanocomposite structures and properties. Studies on materials like ZnO/Mn reveal that carrier gas types impact magnetic properties, especially at lower temperatures [91]. Similarly, as reported variations in carrier gases influence the crystallinity and film quality of α -Ga₂O₃ [92]. These differences can arise from the reaction conditions created by the carrier gases; for example, air and oxygen create oxidizing atmospheres, while gases like Ar or N₂ provide inert conditions, leading to varied nanoparticle characteristics [90].

Table 7. Previous studies on nanomaterials fabrication via spray pyrolysis

Materials	Precursor	Parameter	Morphology	Application	Ref.
ZnO/Ag powder	Zinc Nitrate Hexahydrate Silver nitrate	Furnace T=700–900 °C		Photocatalyst	[54]
TiO ₂ /Ag powder	Titanium(IV) isopropoxide Silver acetate	Furnace T=800–1000 °C		Photocatalyst	[37]
ZnO/Al film	Zinc acetate dihydrate Aluminium chloride	Substrate T=400 °C		Gas sensor	[93]
TiO ₂ film	Titanium (IV) isopropoxide	Substrate T=250–450 °C		Photocatalyst	[94]

In this chapter, ZnO and ZnO-Ag particles were fabricated via a one-step gas-phase SP method by varying the O₂:N₂ carrier gas ratios (1:0, 1:2, 1:1, 2:1, and 0:1). The photocatalytic activity was assessed for actual textile dye wastewaters.

4.2. Materials and experimental setup

Nanoparticles were fabricated using a one-step SP method as illustrated in **Figure 42**. Zinc acetate dehydrate crystals ($\text{Zn}(\text{CH}_3\text{COO})_2 \cdot 2\text{H}_2\text{O}$, 99.5%, E. Merck) served as the precursor for distilled water as the solvent. The solution with a final concentration of 0.1 M was ultrasonicated for 30 min to ensure uniform dissolution of zinc acetate. Subsequently, the aqueous solution was supplied to the nebulizer using a peristaltic pump (Omron, NE-U17) continuously. The precursor underwent aerosolization, and the resulting droplets were carried to the tubular furnace by gas at 2 L/min. Various $\text{O}_2:\text{N}_2$ ratios (1:0, 1:2, 1:1, 2:1, and 0:1) were employed. The tubular furnace was maintained at a temperature of 400 °C, to ensure evaporation of the solvent and decomposition of the precursor. The produced nanoparticle powder was collected in the electrostatic precipitator at an applied voltage of 40 kV and a temperature of 120 °C to prevent condensation. ZnO-Ag nanocomposites were fabricated by adding silver nitrate (AgNO_3 , 99.5%, E. Merck) at concentrations of 1, 5, and 10 wt. % to the zinc acetate solution.

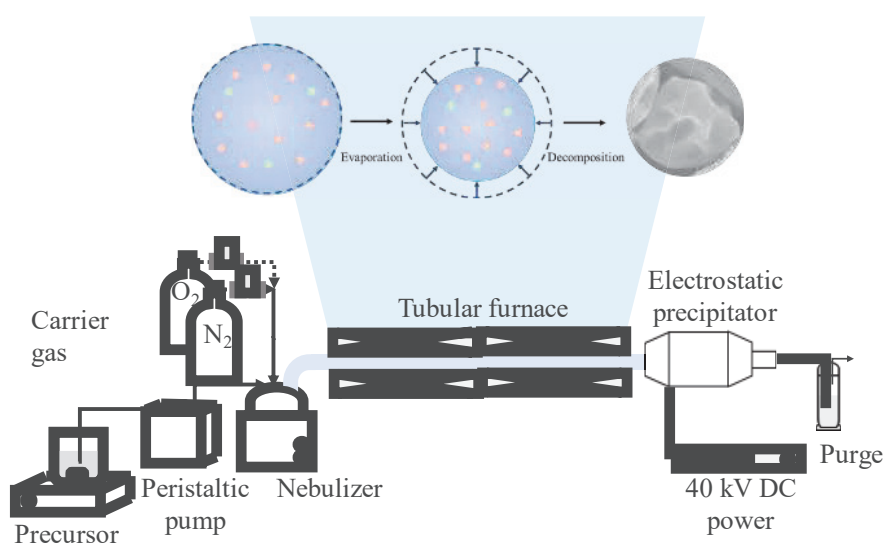


Figure 42. Schematic of SP experimental setup.

4.3. Powder characterization

The nanoparticle morphology was observed using SEM (FlexSEM1000, Hitachi High Technologies), and further observation of the morphology and elemental analysis was conducted by TEM-EDS (JEM-2010, JEOL). The crystallinity and phase composition of the nanoparticles were determined by XRD (Philip XPERT MPD, Philips) operated at 40 kV and 30 mA. The XRD patterns were obtained within a 2θ range of $20\text{--}80^\circ$. Furthermore, the surface area of the nanoparticles was determined by a nitrogen gas adsorption device (Quantachrome Instruments).

4.4. Evaluation of photocatalytic activity

The photocatalytic activity of the nanoparticles was evaluated for the degradation of organic dye pollutants. In this study, textile wastewater obtained from UD, ATBM Jufri Hartono, Gresik, East Java, was used. Initially, the wastewater was diluted tenfold using distilled water. Subsequently, 30 mL of the diluted pollutant solution was mixed with 10 mg nanoparticle powder inside a glass beaker and stirred continuously during the photocatalytic test. To establish adsorption-desorption equilibrium between the photocatalyst and pollutants, the sample was kept in a dark chamber for 30 min. The photocatalytic test lasted for 90 min, with absorbance measurements taken at 30 min intervals. After each measurement, the sample was centrifuged at 5000 rpm to separate the powder catalyst from the liquid pollutant. The absorbance of the resulting supernatant was then measured using the UV-Vis spectrophotometer. The concentration of the dye was determined based on the measured absorbance intensity where they are proportional. The reaction rate constant was calculated from the slope of the equation $\ln(C_t/C_0) = kt$, where k , t , C_t , and C_0 represent the reaction rate constant, reaction time,

final concentration, and initial concentration, respectively.

4.5. Results and discussions

Figure 43 illustrates the morphology of ZnO and ZnO-Ag nanoparticles fabricated via SP method. Crumpled-shaped secondary submicron particles are observed, with no significant morphological change at different Ag contents and carrier gas ratios.

The size of the secondary submicron particles was measured, where comparison based on the carrier gas ratio and Ag content can be found in **Figure 44**. The increase in Ag content does not affect the size distribution; however, the diameters of the secondary particles slightly increase with the increase in the N₂ carrier gas ratio. The formation of these nanoparticles occurred during the evaporation of the solvent droplets in the aerosolized precursor followed by compression and decomposition of the precursor in the tubular furnace [55].

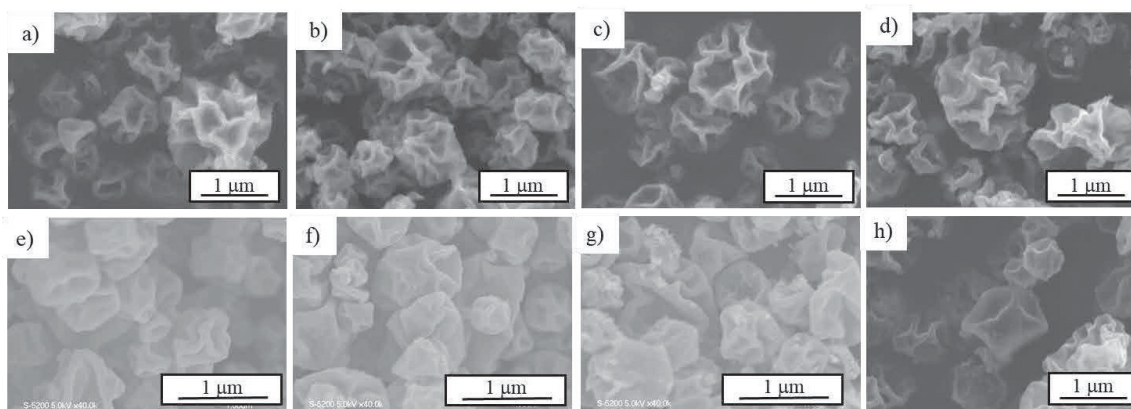


Figure 43. SEM images of a) ZnO and ZnO-Ag with Ag concentrations of b) 1 wt. %, c) 5 wt. %, and d) 10 wt. % fabricated at an O₂:N₂ ratio of 0:1. ZnO-Ag with Ag content of 10 wt. % fabricated at an O₂:N₂ ratio of e) 1:2, f) 1:1, g) 2:1, h) 1:0.

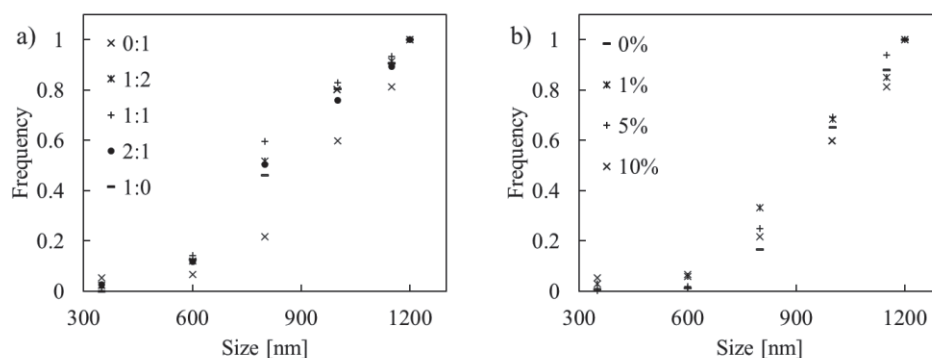


Figure 44. Cumulative size distribution ZnO and ZnO-Ag nanoparticles based on a) carrier gas ratios and b) Ag contents.

These morphological results align well with previous studies [54,95], indicating that the formation of the nanoparticles and the obtained morphology are influenced by parameters such as the evaporation rate of the solvent and concentration of the precursor. Such as the illustration in **Figure 42**, in the evaporation process the confinement force, which compresses the droplets within the pathway inside the furnace can affect the morphology and size of the nanoparticles. The confinement force is proportional to the evaporation rate. A furnace temperature of 400 °C is sufficiently high to cause a significant water solvent evaporation rate to form the crumpled-shaped spherical structure.

The TEM images **Figure 45** revealed crumpled-shaped spheres consist of smaller primary nanoparticles. The corresponding EDS indicates the presence of Zn, O, and Ag. In pristine ZnO, peaks such as Zn L α , Zn K α , Zn K β , and O K α confirm the presence of ZnO. The Ag L α peak confirms the presence of Ag nanoparticles. It's worth noting that peaks such as Cu K α and Cu K β correspond to the TEM grid used, no impurities are observed in the samples.

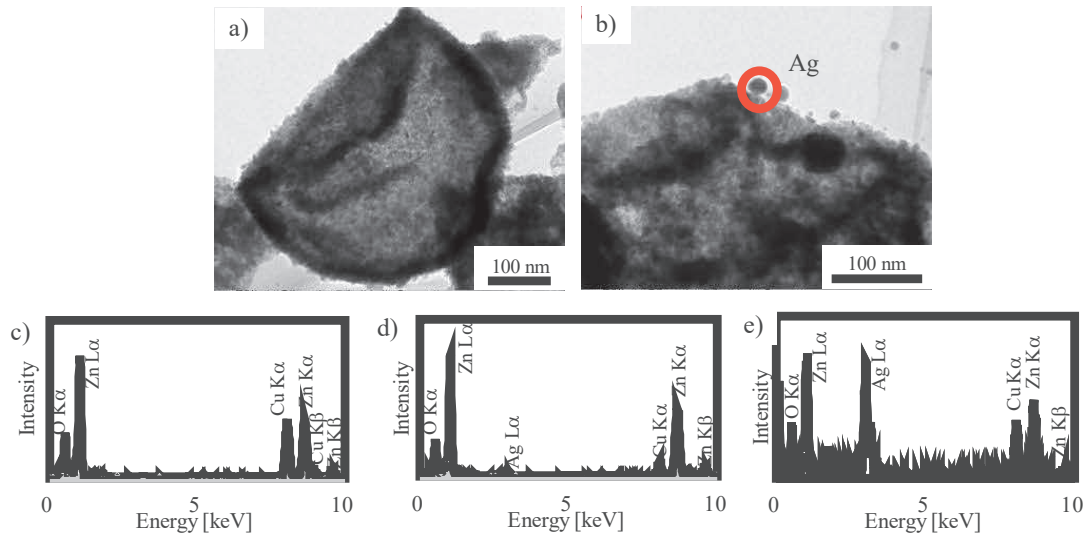


Figure 45. TEM images of a) ZnO and b) ZnO-Ag nanoparticles with 10 wt. % Ag content. Corresponding EDS spectra of c) ZnO and d) ZnO-Ag nanoparticles (bulk) and e) highlighted in red circle.

Hexagonal ZnO was identified by the XRD peaks (**Figure 46**) at $2\theta = 31.5^\circ, 33.9^\circ, 35.8^\circ,$ and 56.5° , corresponding to the (100), (002), (101), and (110) crystal planes, respectively [96]. High N_2 ratios result in the observation of Zn peaks (**Figure 46a**). The use of zinc acetate dihydrate as the precursor leads to Zn formation at 400°C . ZnO can form at sufficient amount of O_2 [97]. The reaction that occurs in the decomposition of zinc acetate dihydrate follows eq. 13–15.



The Ag peak is only observed at high Ag contents, regardless of O_2 or N_2 -rich ratios, with the FCC peak of Ag observed at $2\theta = 37.82^\circ$ for the (111) crystal plane. These XRD peaks confirm the successful formation of crystallized ZnO and Ag nanoparticles from the decomposition of zinc acetate dihydrate and silver nitrate by SP under both N_2 -

and O₂-rich conditions.

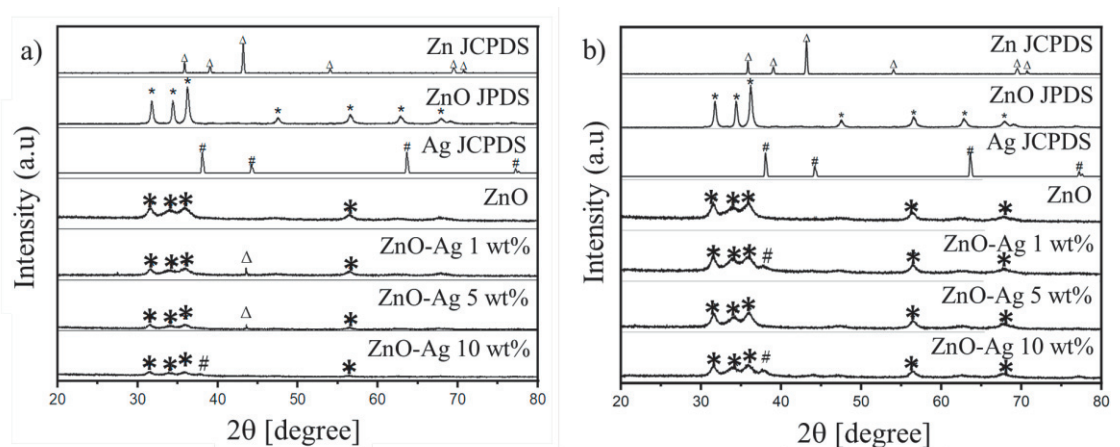


Figure 46. Crystalline phase of ZnO and ZnO-Ag fabricated at a carrier gas (O₂:N₂) ratio of a) 0:1 and b) 1:0.

The surface area of the nanoparticles was determined using a nitrogen adsorption BET method. Typically, a tightly packed nanoparticle structure results in a higher surface area and better contact between active sites and pollutants, optimizing organic compound degradation. However, except for samples with 5 wt. % Ag content, the surface area decreases with increasing O₂ ratio (**Figure 47**). The highest surface area was observed at 10 wt. % Ag content using pure N₂ as the carrier gas. Interestingly, despite the increase in secondary nanoparticle size, the surface area did not decrease as expected. This difference may be attributed to the unique crumpled-shaped of the nanoparticles developed in this study. Furthermore, because of 5-point BET measurement used there are some limitations with these results. However, it can still represent the surface area of the samples.

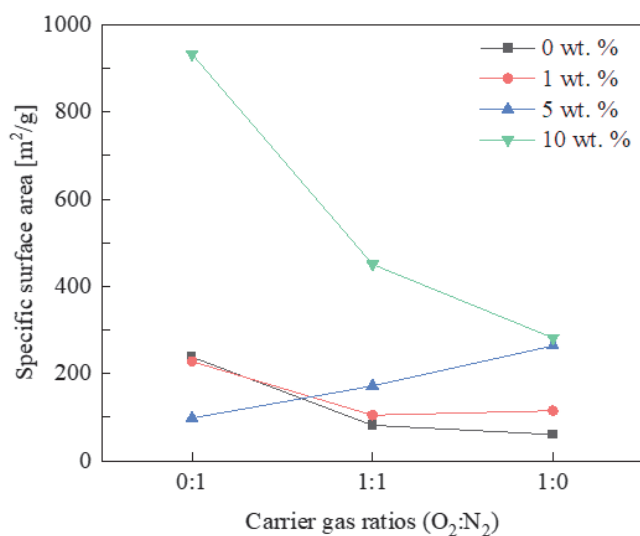


Figure 47. The comparison of surface areas at various Ag contents and carrier gas ratios for the fabricated ZnO and ZnO-Ag nanoparticles.

The photocatalytic activity of ZnO and ZnO-Ag nanoparticles was investigated for the degradation of textile wastewater under UV light irradiation. **Figure 48** shows the impact of Ag content and carrier gas ratios on the degradation reaction rate constant. At different Ag contents (0–10 wt. %) and carrier gas ratios, similar trends in rate constants were observed, with N₂-rich carrier gas demonstrating the highest photocatalytic activity in all samples. As discussed previously, the choice of carrier gas can influence various characteristics of the nanoparticles produced. An increase in the nitrogen ratio resulted in higher nanoparticle surface area, which can enhance photocatalytic activity. Additionally, Zn metal was detected in nanoparticles produced in higher N₂ ratios. The presence of Zn improved separation of electrons–holes [98,99]. When exposed to light, electrons generated in ZnO migrate to zinc, leaving holes in the VB, which react with water or hydroxyl ions to form •OH. Electrons on the surface of Zn further react with dissolved oxygen, yielding superoxide radicals.

At 10 wt. % Ag content, the influence of carrier gases on photocatalytic activity was more pronounced compared to lower Ag contents. However, the exact reason for this phenomenon remains unclear. Both Ag content and carrier gas type significantly impact the photocatalytic activity of the developed nanoparticles.

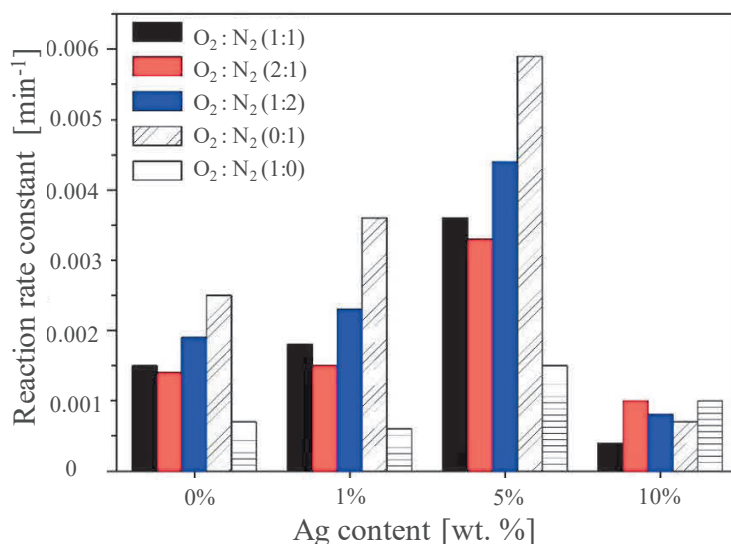


Figure 48. Reaction rate constant of ZnO and ZnO-Ag at different Ag contents and carrier gas ratios

The absorbance spectra of the fabricated samples with different carrier gases ratios and Ag contents were measured such seen in **Figure 49**. Absorbance measurements provided insights for response to shorter wavelengths of light, indicating better performance under UV light irradiation. Additionally, the presence of Ag metal nanoparticles was confirmed from the absorbance spectra, with peaks observed at wavelengths of 350–400 nm, attributed to the LSPR of Ag metal nanoparticles.

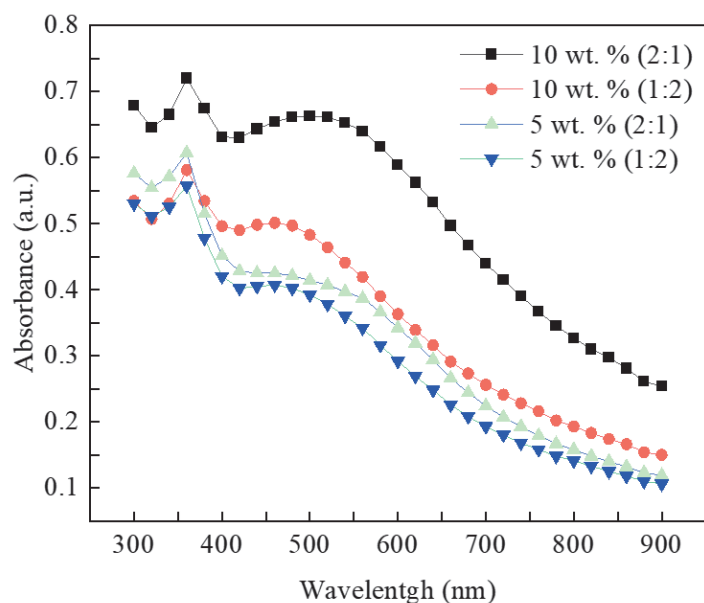


Figure 49. Absorbance spectra of ZnO-Ag nanoparticles with different Ag content and O₂:N₂ carrier gas ratios.

Despite achieving a higher surface area and the higher light absorption at a 10 wt. % Ag content, the optimal photocatalytic activity is observed at a 5 wt. % Ag content. This difference may be attributed to the excessive amount of Ag at 10 wt. %, which serves as charge recombination centers. The negatively charged Ag facilitates the capturing of holes, leading to reduced electron–hole separation and consequently decreasing the degradation of organic compounds [54,100]. Moreover, the increase in foreign material can reduce the photocatalytic activity under UV light irradiation due to the shielding effect on the active sites of the photocatalyst [101]. Several parameters, including surface area [5], crystallinity [102], and crystallite size [96], as well as the concentration of Ag [5], collectively influence the photocatalytic degradation process.

4.6. Conclusions

Crumpled-shaped ZnO and ZnO-Ag submicron secondary particles were produced by a one-step gas-phase SP method. The submicron particles consist of smaller primary spherical nanoparticles. These nanoparticles were fabricated at varying Ag concentrations and O₂:N₂ carrier gas ratios. The existence of Ag can be observed at higher content (> 5 wt. %). The change of Ag content showed no effects towards the crumpled-shaped morphology and size. The carrier gas ratio gave minimal impact on the morphology and primary size of the nanoparticles; however, it did affect the surface area and secondary nanoparticles size. In addition, with N₂-rich carrier gas ratio, Zn was formed, confirmed from the XRD patterns. The nanoparticles demonstrated promising performance, with optimal activity observed for ZnO-Ag with 5 wt. % Ag content, fabricated under N₂-rich conditions.

Blank page

Chapter 5

Summary

5.1. Conclusions

The fabrication of semiconductor-based materials can be achieved in several methods. The gas-phase method is advantageous, owing to its simple steps in the fabrication process, which can fabricate nanomaterials in a one-step manner. Furthermore, it allows for precise control over the characteristics of the produced nanomaterials (size, crystallinity, purity, and uniformity) while minimizing environmental impact. Therefore, it is suitable for large-scale production. The gas-phase method includes the PECVD, PVD, and spray pyrolysis methods.

In this dissertation photocatalyst of TiO₂ nanoparticulate thin film with loaded materials such as CuO and Ag were successfully fabricated by means of a one-step PECVD and evaporation-condensation PVD. Furthermore, in extending the one-step gas-phase method and semiconductor-based materials, ZnO and Ag-loaded ZnO nanoparticles were fabricated by means of SP method.

TiO₂ and TiO₂-CuO nanoparticulate thin films were successfully fabricated through a one-step PECVD-PVD method. The annealing temperature changed the size and crystalline phase of TiO₂ nanoparticles, with CuO loading enhancing the photocatalytic activity, particularly in rutile TiO₂. Additionally, investigations into the photocatalytic activity of anatase- TiO₂ with the change of pH and addition of H₂O₂ revealed the highest photocatalytic activity was achieved at pH 13 for anatase- TiO₂-CuO/H₂O₂.

Similarly, TiO₂ and TiO₂-Ag nanoparticulate thin films, produced via the one-step PECVD-PVD method, demonstrated increased light absorption with Ag addition,

extending their application potential into visible light. Photocatalytic testing confirmed enhanced degradation rates, especially with 0.24 wt. % Ag content. Further investigation for the annealing parameter revealed that higher heating rates led to higher crystallinity. Additionally, the surface area and total pore volume increased with the heating rate. Photocatalytic activity test for MB degradation under UV light revealed enhancement with increasing heating rate.

Furthermore, crumpled-shaped ZnO and ZnO-Ag particles fabricated via SP method exhibited promising results in the degradation textile wastewater, with optimal activity observed in Ag-loaded ZnO nanoparticles containing 5 wt. % Ag, fabricated under N₂-rich conditions.

These findings highlight the versatility of the gas-phase method and effectiveness in tailoring nanoparticle properties for photocatalysis.

5.2. Suggestions for future studies

The current investigation centered on the one-step gas-phase fabrication of semiconductor-based nanomaterials comprising of the PECVD, PVD, and SP method. Semiconductor-based loaded with either semiconductor or metal nanomaterials have been successfully fabricated, with materials of TiO₂-CuO, TiO₂-Ag and ZnO-Ag. These materials are used for photocatalytic degradation of organic liquid pollutants. However, there are opportunities to further optimize the experimental parameters and expand the range of applications.

1. The concentration could be adjusted by modifying PVD system parameters, such as the carrier gas flow rate or heating temperature. Additionally, alternative setups, such as using quenching gas instead of the cooling water system, could be explored

for rapid cooling.

2. Additional research in photocatalytic applications could focus on a comprehensive assessment of the active species involved and the reaction pathways. Furthermore, monitoring in the overall change of the degraded organic pollutant throughout photocatalysis could provide valuable insights.
3. The one-step gas-phase method involving PECVD, PVD, and SP systems can be utilized to explore the fabrication of other materials, which can further broaden their application scope.
4. Owing to the characteristics of the fabricated materials, such as the morphology, light absorption capabilities, and high surface area. Furthermore, the known potential of TiO₂ and ZnO, gas sensing applications could be an intriguing subject for future studies.

Blank page

References

1. Ong, C.B.; Ng, L.Y.; Mohammad, A.W. *Renew. Sustain. Energy Rev.* **2018**, *81*, 536–551.
2. Paździor, K.; Bilińska, L.; Ledakowicz, S. *Chem. Eng. J.* **2019**, *376*, 120597.
3. Herrmann, J.-M. *ASME Int. Mech. Eng. Congr. Expo. Proc.* **1999**, *53*, 115–129.
4. Chen, D.; Cheng, Y.; Zhou, N.; Chen, P.; Wang, Y.; Li, K.; Huo, S.; Cheng, P.; Peng, P.; Zhang, R.; Wang, L.; et al. *J. Clean. Prod.* **2020**, *268*, 121725.
5. Saravanan, R.; Karthikeyan, N.; Gupta, V.K.; Thirumal, E.; Thangadurai, P.; Narayanan, V.; Stephen, A. *Mater. Sci. Eng. C* **2013**, *33*, 2235–2244.
6. Zhao, W.; Feng, L.; Yang, R.; Zheng, J.; Li, X. *Appl. Catal. B Environ.* **2011**, *103*, 181–189.
7. Zhang, X.; Wang, Y.; Hou, F.; Li, H.; Yang, Y.; Zhang, X.; Yang, Y.; Wang, Y. *Appl. Surf. Sci.* **2017**, *391*, 476–483.
8. Abdullah, F.H.; Bakar, N.H.H.A.; Bakar, M.A. *J. Hazard. Mater.* **2022**, *424*, 127416.
9. Ahmad, R.; Ahmad, Z.; Khan, A.U.; Mastoi, N.R.; Aslam, M.; Kim, J. *J. Environ. Chem. Eng.* **2016**, *4*, 4143–4164.
10. Demirci, S.; Dikici, T.; Yurddaskal, M.; Gultekin, S.; Toparli, M.; Celik, E. *Appl. Surf. Sci.* **2016**, *390*, 591–601.
11. Kubo, M.; Mantani, Y.; Shimada, M. *J. Chem. Eng. JAPAN* **2015**, *48*, 292–299.
12. Zhang, J.; Zhou, P.; Liu, J.; Yu, J. *Phys. Chem. Chem. Phys.* **2014**, *16*, 20382–20386.
13. Humayun, M.; Raziq, F.; Khan, A.; Luo, W. *Green Chem. Lett. Rev.* **2018**, *11*, 86–102.
14. Etacheri, V.; Di Valentin, C.; Schneider, J.; Bahnemann, D.; Pillai, S.C. *J. Photochem. Photobiol. C Photochem. Rev.* **2015**, *25*, 1–29.
15. Pathak, T.K.; Kroon, R.E.; Swart, H.C. *Vacuum* **2018**, *157*, 508–513.
16. Gogoi, D.; Namdeo, A.; Golder, A.K.; Peela, N.R. *Int. J. Hydrogen Energy* **2020**, *45*, 2729–2744.
17. Tang, C.; Chen, C.; Zhang, H.; Zhang, J.; Li, Z. *Phys. B Condens. Matter* **2020**, *583*, 412029.
18. Erdogan, N.; Bouziani, A.; Park, J.; Micusik, M.; Kim, S.Y.; Majkova, E.; Omastova, M.; Ozturk, A. *J. Photochem. Photobiol. A Chem.* **2019**, *377*, 92–100.
19. Hardiansyah, A.; Budiman, W.J.; Yudasari, N.; Isnaeni; Kida, T.; Wibowo, A. *ACS Omega* **2021**, *6*, 32166–32177.
20. Wu, C.Y.; Lee, Y.L.; Lo, Y.S.; Lin, C.J.; Wu, C.H. *Appl. Surf. Sci.* **2013**, *280*, 737–744.
21. Mardikar, S.P.; Kulkarni, S.; Adhyapak, P. V. *J. Environ. Chem. Eng.* **2020**, *8*, 102788.
22. Qi, K.; Cheng, B.; Yu, J.; Ho, W. *Chinese J. Catal.* **2017**, *38*, 1936–1955.
23. Udayabhanu; Lakshmana Reddy, N.; Shankar, M. V.; Sharma, S.C.; Nagaraju, G. *Int. J.*

- Hydrogen Energy* **2020**, *45*, 7813–7828.
24. Kumar, S.G.; Rao, K.S.R.K. *Appl. Surf. Sci.* **2017**, *391*, 124–148.
 25. Nakate, U.T.; Patil, P.; Na, S.I.; Yu, Y.T.; Suh, E. kyung; Hahn, Y.B. *Colloids Surfaces A Physicochem. Eng. Asp.* **2021**, *612*, 125962.
 26. Scuderi, V.; Amiard, G.; Sanz, R.; Boninelli, S.; Impellizzeri, G.; Privitera, V. *Appl. Surf. Sci.* **2017**, *416*, 885–890.
 27. Sathishkumar, P.; Sweena, R.; Wu, J.J.; Anandan, S. *Chem. Eng. J.* **2011**, *171*, 136–140.
 28. Tekin, D.; Kiziltas, H.; Urgan, H. *J. Mol. Liq.* **2020**, *306*, 112905.
 29. Alqahtani, A.; Alraddadi, S.; Alshomrany, A.S.; Qasem, A. *Opt. Mater. (Amst)*. **2024**, *149*, 115002.
 30. Ansari, F.; Sheibani, S.; Caudillo-Flores, U.; Fernández-García, M. *J. Sol-Gel Sci. Technol.* **2020**, *96*, 464–479.
 31. Hu, Q.; Huang, J.; Li, G.; Jiang, Y.; Lan, H.; Guo, W.; Cao, Y. *Appl. Surf. Sci.* **2016**, *382*, 170–177.
 32. Li, B.; Hao, Y.; Zhang, B.; Shao, X.; Hu, L. *Appl. Catal. A Gen.* **2017**, *531*, 1–12.
 33. Honda, M.; Ochiai, T.; Listiani, P.; Yamaguchi, Y.; Ichikawa, Y. *Materials (Basel)*. **2023**, *16*, 639.
 34. Date, M.K.; Yang, L.; Yang, T.; Wang, K.; Su, T. *Nanoscale Res. Lett.* **2020**, *15*, 45.
 35. Kubiak, A.; Bielan, Z.; Kubacka, M.; Gabała, E.; Zgoła-Grześkowiak, A.; Janczarek, M.; Zalas, M.; Zielińska-Jurek, A.; Siwińska-Ciesielczyk, K.; Jesionowski, T. *Appl. Surf. Sci.* **2020**, *520*, 146344.
 36. Kirk, C.H.; Wang, P.; Chong, C.Y.D.; Zhao, Q.; Sun, J.; Wang, J. *J. Mater. Sci. Technol.* **2024**, *183*, 152–164.
 37. Haugen, A.B.; Kumakiri, I.; Simon, C.; Einarsrud, M.A. *J. Eur. Ceram. Soc.* **2011**, *31*, 291–298.
 38. Dong, H.; Zeng, G.; Tang, L.; Fan, C.; Zhang, C.; He, X.; He, Y. *Water Res.* **2015**, *79*, 128–146.
 39. Pragati Fageria; Subhashis Gangopadhyay; Surojit Pande *RSC Adv.* **2014**, *4*, 24962–24972.
 40. Ran, H.; Fan, J.; Zhang, X.; Mao, J.; Shao, G. *Appl. Surf. Sci.* **2018**, *430*, 415–423.
 41. Rinaudo, M.G.; Beltrán, A.M.; Fernández, M.A.; Cadús, L.E.; Morales, M.R. *Mater. Today Chem.* **2020**, *17*.
 42. Abbad, S.; Guergouri, K.; Gazaout, S.; Djebabra, S.; Zertal, A.; Barille, R.; Zaabat, M. *J. Environ. Chem. Eng.* **2020**, *8*.
 43. Zhang, Y.; Wang, T.; Zhou, M.; Wang, Y.; Zhang, Z. *Ceram. Int.* **2017**, *43*, 3118–3126.
 44. Camenzind, A.; Caseri, W.R.; Pratsinis, S.E. *Nano Today* **2010**, *5*, 48–65.

45. Gass, S.; Cohen, J.M.; Pyrgiotakis, G.; Sotiriou, G.A.; Pratsinis, S.E.; Demokritou, P. *ACS Sustain. Chem. Eng.* **2013**, *1*, 843–857.
46. Kruis, F.E.; Fissan, H.; Peled, A. *J. Aerosol Sci.* **1998**, *29*, 511–535.
47. Teleki, A.; Heine, M.C.; Krumeich, F.; Akhtar, M.K.; Pratsinis, S.E. *Langmuir* **2008**, *24*, 12553–12558.
48. Feng, J.; Chen, D.; Pikhitsa, P. V.; Jung, Y. ho; Yang, J.; Choi, M. *Matter* **2020**, *3*, 1646–1663.
49. Kusdianto, K.; Jiang, D.; Kubo, M.; Shimada, M. *Ceram. Int.* **2017**, *43*, 5351–5355.
50. Nguyen, H.T.; Byeon, J.H.; Phung, C.D.; Pham, L.M.; Ku, S.K.; Yong, C.S.; Kim, J.O. *ACS Appl. Mater. Interfaces* **2019**, *11*, 24959–24970.
51. Sriram, S.R.; Parne, S.R.; Pothukanuri, N.; Edla, D.R. *J. Anal. Appl. Pyrolysis* **2022**, *164*, 105527.
52. Jamkhande, P.G.; Ghule, N.W.; Bamer, A.H.; Kalaskar, M.G. *J. Drug Deliv. Sci. Technol.* **2019**, *53*, 101174.
53. Kim, R.; Jang, J.S.; Kim, D.H.; Kang, J.Y.; Cho, H.J.; Jeong, Y.J.; Kim, I.D. *Adv. Funct. Mater.* **2019**, *29*, 1–10.
54. Dermenci, K.B.; Genc, B.; Ebin, B.; Olmez-Hanci, T.; Gürmen, S. *J. Alloys Compd.* **2014**, *586*, 267–273.
55. Rahemi Ardekani, S.; Sabour Rouhaghdam, A.; Nazari, M. *Chem. Phys. Lett.* **2018**, *705*, 19–22.
56. Zhou, M.; Roualdès, S.; Zhao, J.; Autès, V.; Ayrat, A. *Thin Solid Films* **2015**, *589*, 770–777.
57. Jung, J.H.; Cheol Oh, H.; Soo Noh, H.; Ji, J.H.; Soo Kim, S. *J. Aerosol Sci.* **2006**, *37*, 1662–1670.
58. Graniel, O.; Weber, M.; Balme, S.; Miele, P.; Bechelany, M. Atomic Layer Deposition for Biosensing Applications. *Biosens. Bioelectron.* 2018, *122*, 147–159.
59. Kubo, M.; Ishihara, Y.; Mantani, Y.; Shimada, M. *Chem. Eng. J.* **2013**, *232*, 221–227.
60. Jiang, D.; Kusdianto, K.; Kubo, M.; Shimada, M. *Mater. Res. Express* **2020**, *7*, 116406.
61. Pedanekar, R.S.; Shaikh, S.K.; Rajpure, K.Y. *Curr. Appl. Phys.* **2020**, *20*, 931–952.
62. Kusdianto, K.; Jiang, D.; Kubo, M.; Shimada, M. *Mater. Res. Bull.* **2018**, *97*, 497–505.
63. Gunnewiek, R.F.K.; Kiminami, R.H.G.A. *Ceram. Int.* **2014**, *40*, 10667–10675.
64. Galizia, P.; Maizza, G.; Galassi, C. *Process. Appl. Ceram.* **2016**, *10*, 235–241.
65. Sierra-Uribe, H.; Córdoba-Tuta, E.M.; Acevedo-Peña, P. *J. Electrochem. Soc.* **2017**, *164*, H279.
66. Singh, J.; Juneja, S.; Soni, R.K.; Bhattacharya, J. *J. Colloid Interface Sci.* **2021**, *590*, 60–71.

67. Sathiyar, K.; Bar-Ziv, R.; Mendelson, O.; Zidki, T. *Mater. Res. Bull.* **2020**, *126*, 110842.
68. Rao, Y.F.; Chu, W. *Chem. Eng. J.* **2010**, *158*, 181–187.
69. Chen, M.; Chen, J.; Chen, C.; Zhang, C.; He, H. *Appl. Catal. B Environ.* **2022**, *300*, 120735.
70. Arshad, R.; Bokhari, T.H.; Javed, T.; Bhatti, I.A.; Rasheed, S.; Iqbal, M.; Nazir, A.; Naz, S.; Khan, M.I.; Khosa, M.K.K.; Iqbal, M. *J. Mater. Res. Technol.* **2020**, *9*, 3168–3178.
71. Fernández, J.; Kiwi, J.; Baeza, J.; Freer, J.; Lizama, C.; Mansilla, H.D. *Appl. Catal. B Environ.* **2004**, *48*, 205–211.
72. Isari, A.A.; Payan, A.; Fattahi, M.; Jorfi, S.; Kakavandi, B. *Appl. Surf. Sci.* **2018**, *462*, 549–564.
73. Wu, M.C.; Lin, T.H.; Hsu, K.H.; Hsu, J.F. *Appl. Surf. Sci.* **2019**, *484*, 326–334.
74. Kumar, M.M.; Badrinarayanan, S.; Sastry, M. *Thin Solid Films* **2000**, *358*, 122–130.
75. Talla, A.; Suliali, N.J.; Goosen, W.E.; Urgessa, Z.N.; Motloung, S. V; Botha, J.R. *Phys. B Phys. Condens. Matter* **2022**, *640*, 414026.
76. Razali, M.H.; Yusoff, M. *Mater. Lett.* **2018**, *221*, 168–171.
77. Gnanasekaran, L.; Pachaiappan, R.; Kumar, P.S.; Hoang, T.K.A.; Rajendran, S.; Durgalakshmi, D.; Soto-Moscoso, M.; Cornejo-Ponce, L.; Gracia, F. *Environ. Pollut.* **2021**, *287*, 117304.
78. Khdary, N.H.; Alkhurajji, W.S.; Sakthivel, T.S.; Khdary, D.N. *Catalysts* **2020**, *10*, 872.
79. Berdini, F.; Otaño, J.O.; Avena, M.; Brigante, M. *Results Eng.* **2022**, *16*.
80. Seery, M.K.; George, R.; Floris, P.; Pillai, S.C. *J. Photochem. Photobiol. A Chem.* **2007**, *189*, 258–263.
81. Dikici, T.; Demirci, S.; Tünçay, M.M.; Yildirim, B.K.; Kaya, N. *J. Sol-Gel Sci. Technol.* **2021**, *97*, 622–637.
82. Luo, Z.; Poyraz, A.S.; Kuo, C.H.; Miao, R.; Meng, Y.; Chen, S.Y.; Jiang, T.; Wenos, C.; Suib, S.L. *Chem. Mater.* **2015**, *27*, 6–17.
83. Fei, J.; Li, J. *Adv. Mater.* **2015**, *27*, 314–319.
84. Han, C.; Likodimos, V.; Khan, J.A.; Nadagouda, M.N.; Andersen, J.; Falaras, P.; Rosales-Lombardi, P.; Dionysiou, D.D. *Environ. Sci. Pollut. Res.* **2014**, *21*, 11781–11793.
85. Bumajdad, A.; Madkour, M. Understanding the Superior Photocatalytic Activity of Noble Metals Modified Titania under UV and Visible Light Irradiation. *Phys. Chem. Chem. Phys.* **2014**, *16*, 7146–7158.
86. Sun, Y.; Gao, Y.; Zeng, J.; Guo, J.; Wang, H. *Mater. Lett.* **2020**, *279*, 128506.
87. Akkari, M.; Aranda, P.; Belver, C.; Bedia, J.; Ben Haj Amara, A.; Ruiz-Hitzky, E. *Appl. Clay Sci.* **2018**, *156*, 104–109.

88. Kusdianto, K.; Sari, T.D.; Laksono, M.A.; Madhania, S.; Winardi, S. *IOP Conf. Ser. Mater. Sci. Eng.* **2021**, *1053*, 12023.
89. Lee, Y.; Fujimoto, T.; Yamanaka, S.; Kuga, Y. *Adv. Powder Technol.* **2021**, *32*, 1619–1626.
90. Leng, J.; Wang, Z.; Wang, J.; Wu, H.H.; Yan, G.; Li, X.; Guo, H.; Liu, Y.; Zhang, Q.; Guo, Z. *Chem. Soc. Rev.* **2019**, *48*, 3015–3072.
91. Vorovsky, V.Y.; Kovalenko, A. V.; Kushneryov, A.I.; Khmelenko, O. V. *Funct. Mater.* **2018**, *25*, 61–66.
92. Xu, Y.; Zhang, C.; Cheng, Y.; Li, Z.; Cheng, Y.; Feng, Q.; Chen, D.; Zhang, J.; Hao, Y. *Mater. 2019, Vol. 12, Page 3670* **2019**, *12*, 3670.
93. Kathwate, L.H.; Umadevi, G.; Kulal, P.M.; Nagaraju, P.; Dubal, D.P.; Nanjundan, A.K.; Mote, V.D. *Sensors Actuators, A Phys.* **2020**, *313*, 112193.
94. Dundar, I.; Krichevskaya, M.; Katerski, A.; Acik, I.O. *R. Soc. Open Sci.* **2019**, *6*.
95. El Rouby, W.M.A. *RSC Adv.* **2015**, *5*, 66767–66796.
96. El-Bindary, A.A.; El-Marsafy, S.M.; El-Maddah, A.A. *J. Mol. Struct.* **2019**, *1191*, 76–84.
97. Wang, R.-C.; Tsai, C.-C. *Appl. Phys. A* **2009**, *94*, 241–245.
98. Wang, P.; Yang, L.; Li, J.; Sadeh, B. *Catal. Letters* **2020**, *150*, 1985–1992.
99. Ma, H.; Yue, L.; Yu, C.; Dong, X.; Zhang, X.; Xue, M.; Zhang, X.; Fu, Y. *J. Mater. Chem.* **2012**, *22*, 23780–23788.
100. Georgekutty, R.; Seery, M.K.; Pillai, S.C. *J. Phys. Chem. C* **2008**, *112*, 13563–13570.
101. Liu, C.; Mao, S.; Wang, H.; Wu, Y.; Wang, F.; Xia, M.; Chen, Q. *Chem. Eng. J.* **2022**, *430*, 132806.
102. Tripathy, N.; Ahmad, R.; Kuk, H.; Lee, D.H.; Hahn, Y.B.; Khang, G. *J. Photochem. Photobiol. B Biol.* **2016**, *161*, 312–317.

Blank page

List of Publications

1. Kusdianto Kusdianto, **Meditha Hudandini**, Dianping Jiang, Masaru Kubo and Manabu Shimada “Effect of Heating Rate on the Photocatalytic Activity of Ag–TiO₂ Nanocomposites by One-Step Process via Aerosol Routes” *Catalysts* **2022**, *12*(1), 17
2. **Meditha Hudandini**, Dianping Jiang, Kusdianto Kusdianto, Masaru Kubo and Manabu Shimada “Functionalization of Nanoparticulate Thin-film Fabrication for Enhanced Properties Via a One-step Gas Phase Method” *Eurozoru Kenkyu* **2022**, *37*(3), 165-171
3. **Meditha Hudandini**, Nurdiana Ratna Puri, Sugeng Winardi, Widiyastuti Widiyastuti, Manabu Shimada and Kusdianto Kusdianto “Photocatalytic Activity of ZnO/Ag Nanoparticles Fabricated by a Spray Pyrolysis Method with Different O₂:N₂ Carrier Gas Ratios and Ag Contents” *Catalysts* **2022** *12*(11) 1374
4. Dianping Jiang, **Meditha Hudandini**, Kusdianto Kusdianto, Masaru Kubo, and Manabu Shimada “Visible-Light-Driven Photocatalytic Activity of Ag Loaded TiO₂ Nanoparticulate Thin Film Fabricated via PECVD-PVD Method” *Chem Eng J Japan* **2024** *12*(1) 17
5. **Meditha Hudandini**, Kusdianto Kusdianto, Masaru Kubo, and Manabu Shimada “Gas-phase fabrication and photocatalytic activity of TiO₂ and TiO₂–CuO nanoparticulate thin films” *Materials* **2024** *12*(1) 17

Blank page

List of Presentations

1. **Meditha Hudandini**, Dianping Jiang, Kusdianto K, Masaru Kubo, Manabu Shimada “Fabrication of TiO₂-copper oxide nanoparticulate thin films through the PECVD-PVD method” *European Aerosol Conference 2021* (Poster presentation).
2. **Meditha Hudandini**, Dianping Jiang, Kusdianto K, Masaru Kubo, Manabu Shimada “One-step fabrication of CuO-loaded TiO₂ nanoparticulate thin film for photocatalytic application under visible light irradiation” *Society of Chemical Engineering of Japan 52nd Autumn Meeting 2021* (Oral presentation).
3. **Meditha Hudandini**, Nurdiana Ratna Puri, Sugeng Winardi, Widiyastuti Widiyastuti, Manabu Shimada, Kudianto Kusdianto “Fabrication of ZnO/Ag Nanoparticles by Spray Pyrolysis Method with Different O₂:N₂ Carrier Gas Ratio and Its Photocatalytic Activity” *International Conference and Exhibition on Powder Technology 2021* (Oral presentation).
4. **Meditha Hudandini**, Dianping Jiang, Kusdianto K, Masaru Kubo, Manabu Shimada “Visible-light Photocatalytic Performance of Cu_xO Loaded Anatase- or Rutile-TiO₂ Fabricated by Gas Phase Method” *Asian Aerosol Conference 2022* (Oral presentation, 2nd place winner).
5. **Meditha Hudandini**, Dianping Jiang, Kusdianto K, Masaru Kubo, Manabu Shimada “One-step gas-phase fabrication of visible-light-activated TiO₂ nanoparticulate thin films” *International Aerosol Conference 2022* (Poster presentation, oral presentation- back up talk).
6. **Meditha Hudandini**, Kusdianto Kusdianto, Masaru Kubo, Manabu Shimada Photocatalytic Performance Evaluation of TiO₂ and TiO₂-CuO Nanoparticulate

Thin Films Prepared by a Gas Phase System” *Society of Chemical Engineering of Japan 54th Autumn Meeting 2023* (Oral presentation).